UNIVERSIDAD NACIONAL AUTÓNOMA DE MÉXICO
POSGRADO EN CIENCIAS FÍSICAS

SPATIOTEMPORAL CHARACTERIZATION OF LASER-INDUCED PLASMAS ON SOIL SAMPLES RE-EXCITED WITH HIGH-VOLTAGE DISCHARGES

TESIS
QUE PARA OPTAR POR EL GRADO DE:
MAESTRO EN CIENCIAS (FÍSICA)

PRESENTA:

ALEJANDRO RAMÍREZ BUENROSTRO

TUTOR:

DR. HUGO MARTÍN SOBRAL
INSTITUTO DE CIENCIAS APLICADAS Y TECNOLOGÍA, UNAM

MIEMBROS DEL COMITÉ TUTOR

DR. NASER QURESHI
INSTITUTO DE CIENCIAS APLICADAS Y TECNOLOGÍA

DR. ROBERTO SANGINÉS DE CASTRO
CENTRO DE NANOCIENCIAS Y NANOTECNOLOGÍA

CIUDAD DE MÉXICO, 2024

PROTESTA UNIVERSITARIA DE INTEGRIDAD Y HONESTIDAD ACADÉMICA Y PROFESIONAL
(Graduación con trabajo escrito)

De conformidad con lo dispuesto en los artículos 87, fracción V, del Estatuto General, 68, primer párrafo, del Reglamento General de Estudios Universitarios y 26, fracción I, y 35 del Reglamento General de Exámenes, me comprometo en todo tiempo a honrar a la Institución y a cumplir con los principios establecidos en el Código de Ética de la Universidad Nacional Autónoma de México, especialmente con los de integridad y honestidad académica.

De acuerdo con lo anterior, manifiesto que el trabajo escrito titulado:

Spatiotemporal Characterization of Laser-Induced Plasmas on Soil Samples Re-excited with High-Voltage Discharges

que presenté para obtener el grado de -----Maestria----- es original, de mi autoría y lo realicé con el rigor metodológico exigido por mi programa de posgrado, citando las fuentes de ideas, textos, imágenes, gráficos u otro tipo de obras empleadas para su desarrollo.

En consecuencia, acepto que la falta de cumplimiento de las disposiciones reglamentarias y normativas de la Universidad, en particular las ya referidas en el Código de Ética, llevará a la nulidad de los actos de carácter académico administrativo del proceso de graduación.

Alejandro Ramírez B.

Atentamente

Alejandro Ramírez Buenrostro
313334539

(Nombre, firma y Número de cuenta de la persona alumna)

Acknowledgements

Desde luego, cualquier agradecimiento debe comenzar por mis padres y Erasmo. No es posible poner en palabras el papel que desempeñaron en este trabajo.

A los miembros de mi comité tutor. Al Dr. Martín Sobral, por su guía en este proyecto y en estos años. Gracias a su dirección se logró ~~a tiempo~~ una tesis más. Al Dr. Naser Qureshi y al Dr. Roberto Sanginés, por sus aportes a este proyecto y sus esmeradas críticas al manuscrito.

Al jurado de este trabajo: Dr. Arturo Robledo Martínez, Dr. Víctor Ulises Lev Contreras Loera, Dr. Óscar Genaro de Lucio Morales y Dr. José Julio Emilio Herrera Velázquez. Espero que esta tesis refleje sus valiosos aportes y exhaustivo escrutinio.

Al Posgrado en Ciencias Físicas y a su equipo. En particular, a la Ing. Jazmín Acosta Reza, por su muy constante apoyo resolviendo mis dudas existenciales.

A los profesores que extendieron mi formación en el Posgrado, los Doctores: Rocío Jáuregui, François Leyvraz, Julio Herrera, Corina Solís, Grisel Méndez, Mufei Xiao, Citlali Sánchez, Jesús Garduño, Karen Volke, Alejandro Vásquez, Omar Morales y Leticia Gracia-Medrano.

Al ICAT y al Laboratorio de Espectroscopía de Plasmas. Agradezco la convivencia con mis compañeros de laboratorio: Eric, Emilio, y particularmente a Mitzi por el trabajo, guía y apoyo en el laboratorio.

Al Dr. Arturo Robledo Martínez por facilitar el equipo de alta tensión utilizado en este trabajo

A los compañeros en estos dos años: Jesús, Omar, y siempre es grato hacer una mención particular a Carlos.

Y para concluir, aunque a veces uno solo quiera barquear, la vida tiene formas curiositas de mantenerte cuerdo. Gracias, Diana.

Investigación realizada gracias al Programa UNAM-PAPIIT Espectroscopia de plasmas producidos por láser para el estudio del medio ambiente, clave IN104421 y a la beca 1179253 del Conacyt.

No man is an island, entire of itself; every man is a piece of the continent, a part of the main; if a clod be washed away by the sea, Europe is the less, as well as if a promontory were, as well as if a manor of thy friend's or of thine own were; any man's death diminishes me, because I am involved in mankind, and therefore never send to know for whom the bell tolls; it tolls for thee.

Devotions Upon Emergent Occasions,
Meditation XVII
John Donne

Abstract

Laser-induced breakdown spectroscopy (LIBS) is a spectroscopic technique that enables elemental identification of samples. Its popularity is due to its capability for in situ applications, rapid results, and usually does not need sample preparation. In this thesis, a laser-induced plasma, produced on a loam soil, at two different temperatures and re-excited with a high-voltage discharge (HV) was characterized.Two distinct experimental configurations were employed to investigate the spectral emission with spatial and temporal resolution along the vertical and horizontal directions of the plasma emission, as well as various acquisition times. Plasma density and temperature were determined using Stark line broadening and the Saha-Boltzmann method, respectively. Fast photography was implemented to study the plasma evolution. The results indicate symmetric temperature and density along the axial direction, even under the influence of a 12 kV HV discharge and varying sample temperatures (22 °C and 400 °C). With both re-excitation techniques—HV discharge and heated sample—electron density and temperature exhibited significant increments. Interestingly, both temperature and density decreased along the cathode direction when the discharge was applied, attributed to the electrical field of the electrodes polarizing the plasma. Photography results revealed that the HV discharge induced turbulence, accelerating the plasma's decay rate. In contrast, the heating system was found to extend the lifetime of the plasma. Both re-excitation techniques demonstrated a substantial increase in emission intensity, with no significant difference between them. Also, the plasma was found to be in Local Thermodynamic Equilibrium at all the experiments performed.

Resumen

La espectroscopía de rompimiento inducida por láser es una técnica espectroscópica que permite la identificación elemental. Su popularidad se debe a su capacidad de aplicación in situ, a la rapidez de sus resultados y a que no requiere preparación previa de la muestra. En esta tesis se caracterizó un plasma inducido por láser, producido sobre un suelo franco, a dos temperaturas diferentes y reexcitado con una descarga de alta tensión. Se implementaron dos configuraciones experimentales diferentes para estudiar, con resolución espacial, la emisión espectral a lo largo de las direcciones vertical y horizontal de la emisión del plasma, así como diferentes tiempos de adquisición. Tanto la densidad como la temperatura del plasma se calcularon a partir del ensanchamiento Stark y del método de Saha-Boltzmann, respectivamente. También se implementó la fotografía rápida para estudiar la evolución del plasma. Se encontró que tanto la densidad como la temperatura son simétricas a lo largo de la dirección axial, incluso cuando se aplicó una descarga de alta tensión (HV) de 12 kV y se utilizaron diferentes temperaturas de la muestra (22 y 400 °C). En ambas configuraciones, descarga HV y muestra calentada, la densidad electrónica y la temperatura aumentaron significativamente. Se observó que tanto la temperatura como la densidad electrónica disminuyen a lo largo de la dirección del cátodo cuando se aplica la descarga. Esto se debe al campo eléctrico de los electrodos que polariza el plasma, separando especies iónicas y especies neutras. Los resultados de fotografía mostraron que la descarga HV induce turbulencia en el plasma, lo que acelera su velocidad de decaimiento. También se observó que el sistema de calentamiento incrementa el tiempo de vida del plasma. Ambas técnicas de reexcitación aumentaron significativamente la intensidad de emisión. No se encontró diferencia significativa entre las emisiones de ambas técnicas. Finalmente, se encontró que el plasma se mantuvo en Equilibrio Termodinámico Local en todos los experimentos realizados.

Contents

List of figures

Introduction

Spectroscopy studies the matter-radiation interaction using absorption or emission processes. In this context, spectral emission or absorption may reveal the atomic structure of the radiated matter. This is because each element has a unique set of spectral lines. Thus, analysis of spectral lines can indicate the presence and even concentration of an element in a sample.

Besides, when a high-power laser source interacts with a sample, an ionization process can occur. In this case, the sample receives sufficient irradiance to be vaporized and ionized. This process may result in the formation of a plasma. A plasma is usually described as a ionized gas in which the charges have a collective behaviour. As a system, a plasma can be described thermodynamically by parameters such as temperature and density. Also, when the plasma radiation is observed through a spectrograph, the spectrum of this radiation is observed. In this case, the wavelengths in the spectrum reveal the atomic constituents of the plasma. Also, there are spectral characteristics such as line intensity and broadening that reflects the nature of the plasma. Then, the main objective of plasma spectroscopy is to study the relation between emission characteristics and plasma characteristics [1].

Laser-induced breakdown spectroscopy (LIBS) is an atomic emission spectroscopic technique that uses a plasma, induced on a sample by a laser, as a source of atomic emission. Assuming that the plasma emission comes from the atomic composition of the target, then LIBS can be used for the target's elemental analysis. Therefore, LIBS is a technique that allows for the elemental analysis of laser-irradiated targets.

LIBS is not the most widely used or reliable atomic emission spectroscopy technique; however, it does have several advantages. First, it has a relatively low cost of implementation. It only needs a laser, optics, a spectrograph and a detector. This sets LIBS as a fast technique, which can offer results of multi elemental analysis in a few minutes with a remarkable operational simplicity [2]. In addition, although most techniques require specific sample preparation, LIBS does not. A typical sample for a LIBS study can be in any state: solid, liquid or gaseous [2, 3]. In the case of liquid or gases, the major problem is the sample container. Then, LIBS only requires that the laser can be focused on the sample. In the case of solids, milling is often used to homogenize the sample to obtain a more uniform plasma, which results in a better representation of the entire sample [4]. For these reasons, LIBS has a wide range of applications, from medical analysis to ambient remediation. One of the most interesting applications of LIBS has been in extra-geological exploration. That is the case of both the Curiosity rover and the mission *Tianwen* which used LIBS to investigate Mars' surface [5, 6]. In the ambient sciences, there is a rising interest in the study of the anthropogenic pollution of the environment. As many of

the food production chains and the extraction of water depends on soil quality, there is crescent interest in the detection of, for example, toxic elements -mainly metals- in soils [7].

In contrast, one of the main drawbacks of LIBS is its relatively low sensitivity. The typical limits of detection for LIBS are in the low ppm regime, $\sim \mu g\, g^{-1}$, and some of the most popular spectrometry techniques, such as inductively coupled plasma (ICP), can reach $\mu g\, kg^{-1}$. Then, it is important to develop signal enhancement techniques for LIBS. And to preserve its application niche, it is important that as LIBS, these techniques are of low cost, operational simplicity and preserve the possibility of *in situ* analysis, with low to no sample preparation. In this context, the possibility of re-excite the laser-induced plasma (LIP) by means of high-voltage discharges and the signal enhancement in LIBS by heating the sample has been previously explored by our research group [8, 9]. These studies focused on improving LIBS sensitivity for the detection of pollutants in soils, then the limits of detection of LIBS were studied. It was shown that LIBS is capable of detecting various metals (e.g., Cd, Cr, Pb, Be.) in soils, with limits of detection under the guideline values of both Mexican standards for agricultural land and the values of priority contaminants of ecology concern of the department of ecology of Washington State, USA [9–11]. Also, as in Ref. [9], this thesis is also focused on plasma on soil samples. These works reported that, re-excitation of the plasma with the HV discharge or heating the sample improved these limits of detection. Furthermore, these techniques maintain the advantages of LIBS that were mentioned above. Then, they are reliable and interesting techniques to improve the main drawback of LIBS. In addition, in these studies, it was observed that both techniques increase plasma parameters (temperature and density), which, in the case of the heating, was attributed to a significantly increase in matter removed from the sample. However, it is not clear how the discharge affects the LIP, and since most typical LIBS studies focus on the elemental detection and the application to different kinds of samples, some of the physics of the plasma remains unstudied. Then, this thesis deals with the physics behind LIBS and mainly in the LIP. In specific, investigates how the plasma changes when it interacts with a high-voltage discharge. Since all LIBS studies suppose that the plasma is in local thermodynamic equilibrium, it is expected to investigate how true that is when the plasma is studied with both spatial and temporal resolution, while interacting with the HV discharge. Also, it is investigated how the discharge enhances the LIBS emission. From the spectral information, the density can be obtained by analysing the line broadening. Also, thermodynamic models can relate the atomic population levels to the plasma temperature, via the Saha equation. Then, in this thesis the plasma density is studied by means of the spectral line broadening, in specific, the Stark broadening. Also, the temperature is obtained with the Saha-Boltzmann method. On the other hand, in order to obtain a description of how the plasma changes with time, its morphological evolution is studied by means of fast photography. These studies are performed with both room-temperature and heated ($400\,^{\circ}C$) soil samples and using the experimental parameters used by Amador-Mejía et al. [9]. Therefore, this thesis also aims to clarify the physics behind the chemical results obtained in that work.

The structure of this thesis can be summarized as follows.

Chapter 1 focuses on LIBS. A brief description of atomic spectroscopy and the basic description of LIBS are provided in Sect. 1.1.1 and Sect. 1.1.2; respectively. In Sect. 1.1.3 the basic instrumentation for a LIBS analysis is provided. It is explained briefly the role of the laser, the target and the optics in the formation of the plasma. Also, how the plasma radiation is collected, processed and analyzed. Once the instrumentation is covered, Sect. 1.1.4 describes the

general procedure and the important parameters of a LIBS experiment. Sect. 1.1.5 summarises some of the most successful applications of LIBS, with a focus on soil studies. Finally, Sect. 1.2 describes the general scheme of both re-excitation techniques and summarises some of the related literature. The focus is on the few studies that used soils and the changes in temperature and electron density.

Chapter 2 is focused on the laser-induced plasma, its main properties, its emission, the methods for its characterization and in the derivation of the Saha-Boltzmann equation. Sect. 2.1 provides a general description of a plasma. Its physical description is focused on its parameters and thermodynamic characteristics. This description leads to the obtention of the Saha equation. Sect. 2.2 describes the formation of the plasma. It is provided a brief description of the ablation process, the internal processes of the plasma, and its evolution. Sect. 2.3 focuses on plasma spectroscopy. The production of the plasma radiation is described in Sect. 2.3.1. Then, in Sect. 2.3.2 it is provided how the spectrum is composed and the main broadening mechanisms, with focus on the Stark broadening. Then, the model known as local thermodynamic equilibrium is described in Sect. 2.3.5. From these models, in Sect. 2.3.4 is described how the electron density is calculated. Finally, both the derivation of the Saha-Boltzmann equation and the method to solve it to obtain the temperature are provided in Sect. 2.3.6.

Chapter 3 describes the experimental procedures in this thesis. Sect. 3.1 provides a description of the instrumentation used, along with the experimental configurations implemented. In Sect. 3.2 the methodology used to investigate the objectives of this work is described. The kind of sample used and the preparation used is specified. Also, the specific details for the implementation of both re-excitation techniques are presented. Then procedures conducted to obtain plasma radiation with spatial and temporal resolution are described. Once the spectral information is collected, it is necessary to specify which transitions are used for the calculations. This is also presented in this chapter. Finally, the specific parameters and details for the fast photography implementation are presented.

Chapter 4 presents and discusses the results obtained. Sect. 4.1 shows how the ablation was performed and the energy used to do it. In Sect. 4.2 the characterization of the HV discharge is presented. It is shown its voltage and current. Also, it is presented the energy that it deposits into the plasma. In Sect. 4.3 a general description of the obtained spectra is presented, along with an example of the signal-to-noise ratio. Sect. 4.4 presents the results obtained with fast photography. The results of the plasma density are presented in Sect. 4.5. The results for the plasma temperature are presented in Sect. 4.6. Sect. 4.7 includes a description of how the atomic species are affected by the discharge. With this, it is answered how the plasma changes internally when the discharge is applied. Finally, Sect. 4.8 provides some calculations of plasma parameters using the values obtained for density and temperature.

The last chapter corresponds to the Conclusions of this work. Then, some of the main highlights of this thesis are listed. Also, a brief plan for future work is proposed.

Chapter 1

Laser-induced breakdown spectroscopy

Laser-induced breakdown spectroscopy is a central focus of this work, as an analytical technique for atomic sample analysis. Due to its capacity to analyze solids, liquids, or gases, coupled with attributes like low cost, portability, minimal sample preparation, speed, and broad applicability, has become a popular technique in atomic spectroscopy. In this study, the central subject of investigation is the plasma. However, laser-induced breakdown spectroscopy is its origin and purpose. Therefore, before a description of the plasma, it is necessary to introduce its implementation framework.

This chapter introduces laser-induced breakdown spectroscopy, covering its general concepts and instrumentation used to analyze the plasma. It outlines the light's path, from the laser to the detector, and the resultant spectrum. The methodology is summarized and key applications are provided to highlight the investigation's importance. This chapter also addresses the critical issue in LIBS, suggesting sample heating and high-voltage discharge as improvement options. Finally, pertinent literature is reviewed to provide an overview of the previous work and expected results.

1.1 Fundamentals of laser-induced breakdown spectroscopy

Laser-induced breakdown spectroscopy (LIBS), also known as laser-induced plasma spectroscopy (LIPS), is an analytical technique that uses a high energy source to ablate a target. When the irradiance, exceeds a given threshold, it initiates the formation of a plasma. This plasma emits radiation that can be analyzed to characterize the target material. In this section, the main concepts regarding LIBS are introduced, exploring its basic instrumentation, methodology, and some applications.

1.1.1 Atomic and plasma spectroscopy

Atomic emission spectroscopy encompasses techniques designed to determine the elemental composition of samples. These techniques aim to atomize the sample because the analysis of the radiation emitted from excited atoms can reveal insights about the sample. Each element has a unique spectrum, allowing for identification based on its position in the spectrum. Furthermore, By calibrating the intensity and with some knowledge of the sample, the concentration of each element can be determined [3]. There are different methods to atomize the sample. Some of the commonly used are the inductively coupled plasma (ICP), electrode sparks, microwave-induced plasma (MIP) and direct coupled plasma (DCP) [3, 12]. Many of these methods involve the use of plasma, which can be defined as an assembly of atoms, ions, and electrons in which these species usually act collectively and maintain global charge neutrality. The utilization of emission to analyze the plasma is known as plasma spectroscopy. Plasma spectroscopy explores the relationship between spectral characteristics, such as wavelength or line broadening, and plasma formation [1, 12].

However, preparing samples for techniques like ICP can be a complex and time-consuming procedure. Moreover, most of the common techniques require large laboratories for operation, limiting their application scope. This work specifically focuses on LIBS, a technique where the plasma for sample atomization is formed directly within the sample. This intrinsic advantage makes LIBS particularly well-suited for in situ applications. Also, as it is explored in this chapter, LIBS proves to be a fast and easy-to-operate technique. In the following sections, The mechanisms for forming plasma in the sample and the instrumentation for a basic LIBS analysis are detailed.

1.1.2 LIBS

In LIBS, the plasma is formed by a focused laser. As depicted in Fig. 1.1 a focused laser can generate irradiances exceeding MW/cm^2. Upon reaching a critical energy deposition, ionization commences, giving rise to the formation of a plasma that rapidly expands. Initially, this plasma

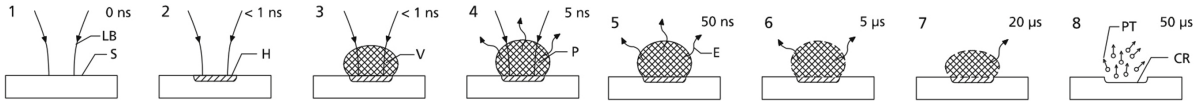

Fig. 1.1: Laser ablation and plasma generation in a sample. 1) The laser (LB) is fired at the sample (S), 2) energy is deposited (H), 3) which leads to vaporization (V) of the sample. 4) Laser-induced plasma (P) forms and expands. 5) Elemental emission. (E) 6) 7) Plasma contracts, 8) resulting in a crater (CR) and emitted particles (PT) [13].

possesses a high density and emits continuum radiation. Subsequently, the plasma undergoes decay and emits element radiation. The complete process can last for about ∼10 µs. In the case of a solid sample, this process results in the creation of a crater due to the ablated material. The emitted radiation is collected and processed to obtain the spectrum. Therefore, a LIBS spectrum can be used to know the concentrations of each element present in the sample [13].

1.1.3 LIBS Instrumentation

Two of the principal advantages of LIBS are its relatively low cost and simple instrumentation. A basic LIBS instrumentation is depicted in Fig. 1.2, which shows that a basic LIBS experiment starts with the laser pulse, focused onto the target. Once the breakdown is achieved, the radiation emitted by the plasma is collected onto a spectrograph and then registered by a detector.

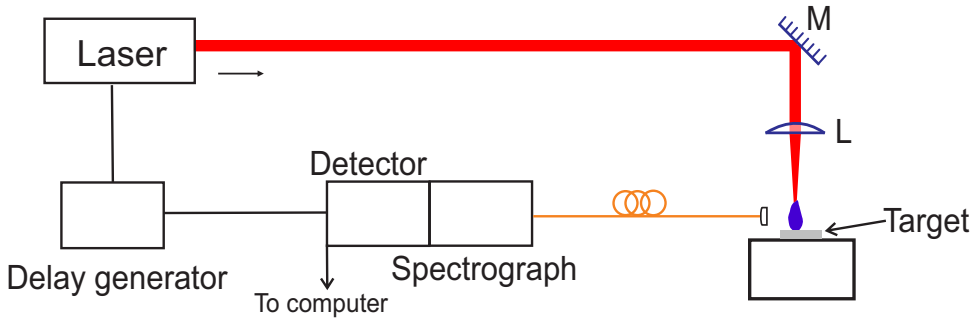

Fig. 1.2: Basic LIBS instrumentation. The laser pulse is focused onto a sample to ablate it. Radiation emitted is collected and conducted, by fibre optics, to a spectrograph with a detector coupled. The information is send to a computer for further analysis. keys: M, mirror; L, lens. Design based on [8]

Therefore, the basic instrumentation to conduct a LIBS experiment is as follows [3, 13]:

Laser: The energy source in LIBS is a laser, which irradiates the sample, inducing breakdown. Its principal parameters include energy, wavelength, irradiance, repetition rate, beam quality, divergence angle, waist, and pulse width.

Target: This refers to the sample undergoing analysis. When irradiated by the laser, a portion of its surface is ablated and atomized. Sample preparation is often minimal, and it can be in solid, liquid, or gas form.

Optics: Optics are essential for guiding the laser to the target and focusing it to achieve the energy needed for breakdown. The properties of the optics depend primarily on the laser wavelength. Additionally, an optic system or fibre optics are commonly required to collect the plasma radiation and transport it to the detector.

Wavelength selector: The collected radiation must be resolved based on its wavelength. Typically, a spectrograph is used for this purpose.

Optical detector: To register the spectrally dispersed radiation, a detector is used. Common detectors are equipped with intensifier devices.

Synchronization and visualization: Synchronization between the laser pulse and the acquisition system is crucial. Typically, a delay generator is employed for this purpose. To program the equipment and visualize the resultant spectra, a computer is required.

The basics of these instruments are addressed in the following sections. It is described their most important parameters and their relation with a basic LIBS experiment.

1.1.3.1 Laser source

LIBS experiments require high-energy laser sources, with peak power typically in the order of MW [12], to generate plasmas. For LIBS, the most widely used type of lasers is the solid-state laser of neodymium-doped yttrium aluminium garnet (Nd:YAG) medium. Next, the most important laser parameters and their influence on LIBS experiments are discussed.

Regarding the exciting radiation that affects the plasma formation process, the laser wavelength λ has a crucial role in radiation-material coupling. Collision-induced ionization becomes the dominant mechanism for ionization with long-wavelength ($\lambda > 1\,\mu m$) lasers. In contrast, multi-photon absorption becomes the primary process for the production of the initial free electrons at short wavelengths ($\lambda < 1\,\mu m$), as the pulse duration is usually shorter than the thermal coupling time [6]. In the first one, laser radiation accelerates electrons, energizing them. This process, known as inverse *Bremsstrahlung*, is followed by collision-induced ionization. The result is an exponential rise in electron density, with a breakdown threshold that may depend on the wavelength as λ^{-2} or λ^{-3}. In the other case, a single atom absorbs multiple photons simultaneously, resulting in its ionization [6].

Another important laser parameter is the pulse duration, which is defined as the full width at half maximum (FWHM) of the pulse temporal profile. Regarding the effect of different pulse duration, there are three principal types: nanosecond, picosecond and femtosecond lasers. The first type, nanosecond lasers, leads to material removal from the target surface. Evaporated matter interacts with the laser pulse, producing its heating and ionization, which leads to plasma formation. Additionally, plasma formation interacts with laser radiation, affecting how much energy the sample can receive. This effect is called plasma shielding and can be mitigated when pulses of short duration are used. For example, picosecond lasers usually deliver higher irradiances with lower radiation-matter interaction time. This type of laser pulse allows for lower energy loss as a result to thermal diffusion in the sample, which leads to a better ablation rate. Furthermore, femtosecond lasers grow electrons by multi-photon ionization, delivering a higher irradiance and ablation efficiency. The latter is a consequence of precise matter removal and less mechanical damage or melting [6].

Regarding energy, the pulse energies of LIBS range from 10 to 500 mJ, depending on the target and experimental requirements [14]. Typically, 100 mJ per pulse allows for plasma generation in most materials. As described earlier, this pulse energy is delivered over a temporal width and impacts an area of the target, with spots a few tens of µm in diameter [15]. This intensity delivered per unit time and area is known as irradiance, typically measured in W/cm^{-2}, with typical values ranging from 10^7 up to 10^{12} W/cm^{-2} [3, 13]. In this section, the irradiance, based on laser properties, will be calculated.

Operating the laser in LIBS experiments, its repetition rate should be defined. There are two principal pump sources for LIBS lasers: a flashlamp and a diode pump. For example, electro-optical Q-switched Nd:YAG lasers pumped by a flashlamp can achieve repetition rates of 10 to 100 Hz, while acousto-optical lasers can yield rates beyond 10 kHz, with smaller pulse energies and grater pulse duration. In contrast, diode-pumped lasers with electro-optic Q-switching can run up to 2 kHz [13]. The selection of a pulse rate depends on target properties (e.g. composition and size) and laser stability, for example the laser ability to maintain constant pulse energies

and temporal profiles. Also, it is important to consider how the state of the ambient gas changes between pulses. To distinguish two plasmas as different events, is necessary for the state of surrounding gas prior to the second plasma to be identical as the state of the gas prior the first one. This requires the ablated material to be removed from the interaction volume, typically by diffusion. to estimate the minimal time required to distinguish two plasmas as separate events, let's suppose a spherical expansion with diameter d. An approximation to typical velocity of the ambient gas may be the sound velocity v and then the minimal time τ between pulses to assure that the material leaves this diameter is about $\tau = d/v$. Although Some authors suggest that the shift distance should be twice the diameter, using typical plasma sizes (few mm) and about 300 m/s for sound velocity, this time is in the order of kHz, which is much larger than the typical repetition rates used in LIBS [13].

The last laser parameter described here is the beam quality and its relation with laser irradiance. The ideal laser beam, a Gaussian beam, is a solution of Maxwell's wave equations and can be produced by laser apertures. In a Gaussian beam propagating along the z-direction, the electric field has a magnitude given by

$$\|\mathbf{E}(z,r)\| = \mathrm{Re}\left\{E(z,r)\right\}\mathrm{Re}\left\{e^{i(2\pi\nu t - k_0 z)}\right\}, \tag{1.1}$$

and an amplitude $E(z,r)$ given by

$$E(z,r) = \frac{\|\mathbf{E_0}\|}{1 - i\dfrac{z\lambda}{w_0^2 n\pi}} \exp\left(-\frac{r^2/w_0^2}{1 - iz\lambda/w_0^2 n\pi}\right), \tag{1.2}$$

where $r = (x^2 + y^2)^{1/2}$ is the radial coordinate, λ the wavelength of the beam traveling in a medium with refractive index n, ν is its frequency and k_0 the wavenumber. The beam waist w_0 represents the beam radius at $z = 0$. The beam radius is defined as the radius where 85% of the whole power of the beam is contained inside an area with radius

$$w(z) = w_0\sqrt{1 + \left(\frac{z}{z_R}\right)^2}, \tag{1.3}$$

where z_R is the Rayleigh length, defined by

$$z_R = \frac{\pi n w_0^2}{\lambda}. \tag{1.4}$$

Rayleigh length defines the distance at which the beam radius increases as $w(z_R) = \sqrt{2}w_0$ and the radius of curvature of the wavefronts becomes minimal [16]. Fig. 1.3 depicts the beam parameters mentioned above. As the figure shows, for distances larger that the Rayleigh length the Gaussian beam diverges linearly. Consequently, in infinite and vacuum, the divergence angle is defined by

$$\tan\theta = \lim_{z\to\infty}\frac{\mathrm{d}w(z)}{\mathrm{d}z} = \frac{w_0}{z_R} = \frac{\lambda}{\pi w_0}. \tag{1.5}$$

Then, low divergence angles can be approximated at first order as

$$\theta \approx \frac{w_0}{z_R} = \frac{\lambda}{\pi w_0}, \tag{1.6}$$

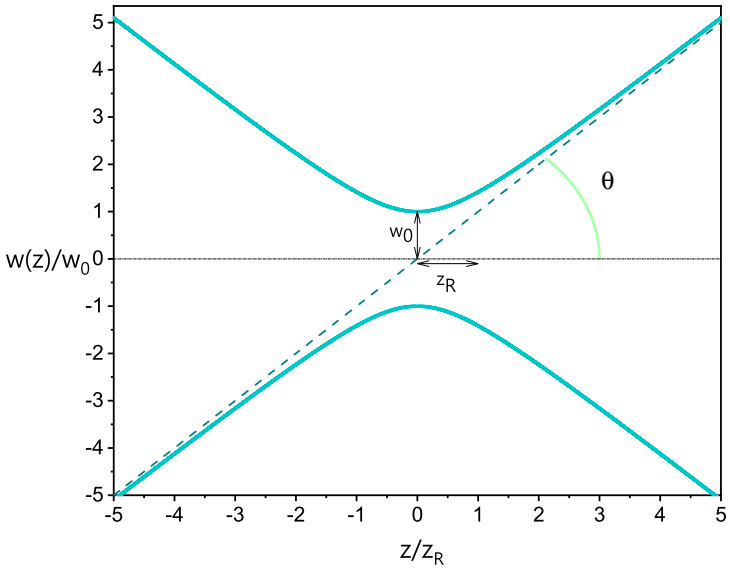

Fig. 1.3: Gaussian beam radius w(z), beam waist w_0, divergence angle θ and Rayleigh length z_R.

which also allows to approximate the beam radius, far from the Rayleigh distance, by using its linear expansion

$$w(z) \approx \frac{w_0 z}{z_R} = \frac{\lambda z}{\pi w_0}. \tag{1.7}$$

Furthermore, Eq. 1.5 relates the beam waist to its divergence. It should be noted that, as an ideal beam, *theta* is minimal for a Gaussian beam with waist w_0 [16]. This property leads to the definition of the beam parameter (BP) as

$$BP = \theta w_0, \tag{1.8}$$

which is also minimal for a Gaussian beam. This quantity describes the beam quality, hence is lower for all other beam types, compared to a Gaussian beam. Thus, the quality of a beam can be defined as

$$M^2 = \frac{BP_{beam}}{BP_{gaussian}} = \frac{\theta \pi}{\lambda} w_0. \tag{1.9}$$

Focusing a laser beam with energy per pulse E and temporal width τ, Eq. 1.9 can be utilized to estimate the average irradiance I at its focal spot [13] as

$$I = \frac{E}{\tau \pi w_0^2} = \frac{E \theta^2 \pi}{\tau \lambda^2 M^4}. \tag{1.10}$$

Laser quality, divergence angle, and waist are usually determined experimentally, and the use of focusing optics allows for achieving the desired irradiance. However, performing a LIBS experiment can require a suitable laser that meets suitable parameters, such as wavelength, energy per pulse, and temporal width. Table 1.1 provides a brief list of the most commonly used lasers in LIBS and their principal parameters. As previously said, the Nd:YAG laser is the most widely used in LIBS due to its high beam quality, efficiency, and portability. Also, its fundamental wavelength can be easily shifted from the near IR up to the near UV region [12].

Table 1.1: Characteristic properties of commonly used lasers for LIBS [6, 12, 13, 15]. Keys: SGH, second harmonic generation; THG, third harmonic generation

Laser type	Wavelength (µm)	Pulse width (ns)	Energy/pulse (mJ)
Nd:YAG	1.06; 0.53 (SHG); 035 (THG)	3-15; 4-14; 4-8	0.1-1,000; 0.05-90; 0.02-10
CO_2	10.6	200	100
Excimer	0.193-0.308	8-35	0.5-1,000
Ruby	0.694	5-30	1-50
Ti:sapphire	0.8	$2 \times 10^{-5} - 2 \times 10^{-4}$	1-5

1.1.3.2 Target

The laser target is the sample under analysis, and energy is typically focused through a lens to achieve the desired irradiance, often requiring minimal sample preparation. However, specialized containers can be utilized when the sample requires specific containment. This is particularly important when specific ambient gas or pressure conditions are necessary. For example, increasing ambient gas density has been shown to enhance material ablation at constant pressures, as the plasma is constrained by local mass, intensifying its interaction with the sample. In contrast, reducing pressure increases the ablation rate by mitigating plasma shielding and material re-condensation [13]. Nevertheless, in-situ applications may make it difficult to use target containers. LIBS is capable of analyzing diverse sample types, including particles, gases and liquids, each with different ablation requirements [14]. For example, when analyzing liquids, optics may be exposed to liquid splashing, a situation that can be mitigated by freezing the sample, which also increases the signal-to-noise ratio[1] (SNR) [17].

In addition to sample-type properties that affect the analysis, matrix effects play a key role. The matrix refers to the composition of the sample, and its effect on the atomic emission spectra is known as matrix effects [7]. These can arise from chemical compositions, where high-concentration elements (major elements) influence the emission of trace elements. Although the information about the atomic structure and bonding of the target should be lost after the plasma disintegrates the sample into its constituents, it has been observed that compounds such as $PbNO_3$ and $PbCl_2$, along with their properties like vaporization temperatures and absorption, can influence the emissions of their individual elements [3, 12]. Particle size similarly can affect sample emission because larger particles can be incompletely vaporized, leading to lower signal compared to smaller particles [12].

The plasma formation, expansion and crater formation are greatly influenced by target properties. One of the most important target parameters is the reflectivity, as it determines the coupling of laser energy with the target. Typically, materials with lower reflectivity exhibit higher absorption than those with reflective surfaces. However, it has been observed that high temperatures can lead to phase changes in materials, resulting in a great energy absorption even on reflective surfaces [7].

[1] In a spectrum, SNR is defined as the rate of the emission intensity to the background noise. It is calculated as the quotient between an emission line intensity and the standard deviation of the spectral background.

Various techniques exist to mitigate matrix effects in LIBS analysis. The use of standards is common to enhance precision by minimizing variability in laser shots [12]. Despite LIBS generally requires minimal sample preparation, specific techniques can be employed to minimize matrix effects. For example, methods such as separation, dilution, homogenization, grinding, milling, fusion, digestion and pellet formation are commonly used. Alongside reducing matrix effects on spectra, these techniques aim to enhance sensibility and reproducibility in LIBS analysis, with milling and pelletizing being among the common methods used to control particle size and achieve sample homogeneity, particularly in complex matrices such as soils [4, 13, 15].

To direct the laser radiation onto the sample and capture the resulting radiation for analysis, specific optics are essential, and these are detailed in the following section.

1.1.3.3 Optics

As previously said, laser radiation is focused onto the sample by a lens whose transmittance should coincide with the laser wavelength. According to Eq. 1.7, if at the lens the laser pulse has a diameter D, the radius at the focal spot will be

$$w_0 = \frac{2\lambda f}{\pi D}, \tag{1.11}$$

where f is the focal length of the lens.

However, focusing the lens at the sample surface might cause the breakdown to befall in the surrounding gas. To avoid this situation, sometimes the laser is focused within the sample in such a way that the irradiance outside the sample is lower than the breakdown threshold of the surrounding gas [6].

On the other hand, to recollect plasma radiation an optical system is used. The configuration needed depends on the experiment. Radiation is focused on the aperture slit of a sprectrograph. However, the most common configurations consist of optical fibers and lenses, as depicted in Fig. 1.4. As the figure shows, a portion of the light emitted can be collected by

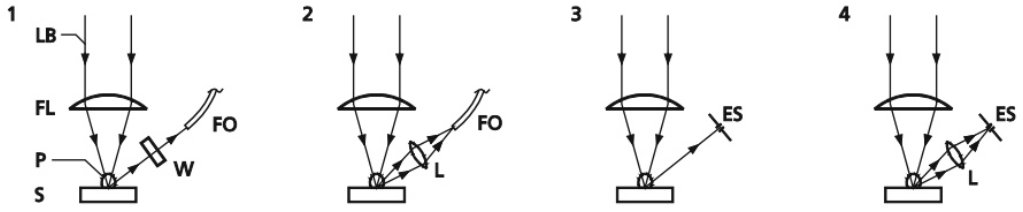

Fig. 1.4: Optical configurations used in LIBS for radiation acquisition [13]. LB = laser beam, FL = focal lens, P = plasma, W = window, FO = optical fibre, L = lens, ES = entrance slit.

an optical fibre. This configuration has advantages in field-based measurements, being capable of perform remote analysis. In this case, the amount of radiation recollected depends on the numerical aperture of the fibre [13, 15]. Additionally, as the configuration number 4 in Fig. 1.4 shows, a lens can be used to form the image of the plasma at the entrance slit. This configuration

results important in spatially resolved measurements[2]. In that case, it is advised to set the collection axis perpendicular to the propagation direction of the expanding plume [6].

As described in this section, with simple optics it is possible to conduce laser radiation and recollect plasma radiation. In the following it is described how to obtain the spectral composition from the plasma radiation.

1.1.3.4 Spectral detection

To determine the spectral composition of plasma radiation, a combination of a wavelength selector and an optical detector is employed as the spectral detection system. In LIBS, spectrographs serve as wavelength selectors, with Paschen-Runge, Czerny-Turner, and Echelle being the most common types, due to their wide resolving power [6, 12].

The Czerny-Turner design, illustrated in Fig. 1.5a), operates as follows: light first passes through the slit and is collimated by the first concave mirror. Subsequently, the radiation is directed to a plane grating, which reflects it at different angles. The dispersion is described by the equation

$$d(\sin\alpha + \sin\beta) = n\lambda, \tag{1.12}$$

where d is the grating period, α is the angle of incidence, β is the angle of diffraction, n is the diffraction order and λ the wavelength. At this point, the spectrum is formed, and a second mirror focuses it onto the focal plane. Finally, the light is recorded by the detector. Some spectrographs may include a slit to select a desired range of wavelengths to pass through to the detector. This configuration allows for high resolution, but its spectral range lies between 10 and 30 nm [12, 13]. In the Echelle type, light is first collimated by a mirror and then refracted

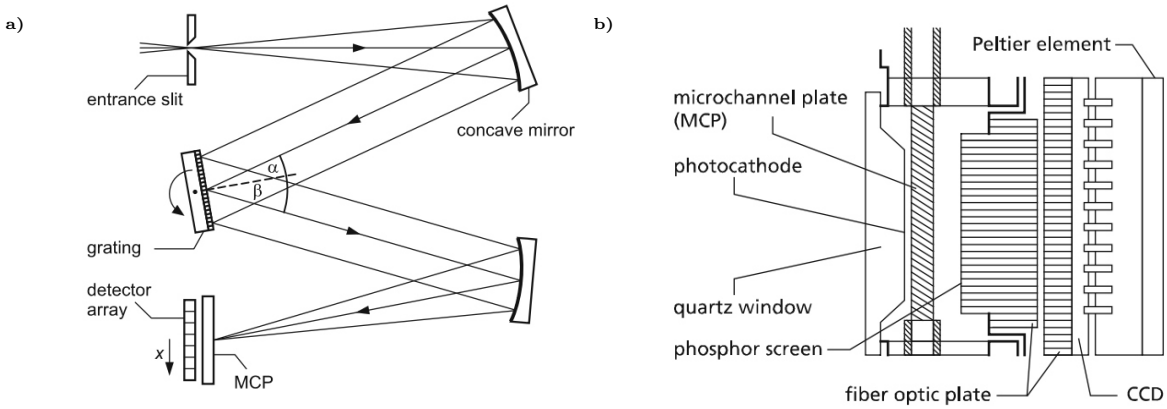

Fig. 1.5: Spectral detection system [13]. a) Spectrograph with design Czerny-Turner b) ICCD detector.

by a prism. The refracted light passes through an Echelle grating. Once diffracted, it passes through the prism again. A camera mirror images the light onto the detector plane. With this design, a spectral range from 200 up to 780 nm can be detected simultaneously. In contrast, Paschen-Runge designs allow for a wide spectral range (from 130 to 590 nm) and high resolution.

[2]This is the configuration used in this work to achieve spatial resolution.

This system consists of an entrance slit and a grating mounted along a Rowland circle, incoming light can be focused at various exit slits; depending on its wavelength [13].

To register spectrally dispersed radiation, there are several types of detectors. PMT detectors consisting of photomultiplier tubes are usually coupled to Paschen-Runge systems. In the case of Czerny-Turner and Echelle designs, the most widely used detectors are known as charged-coupled devices (CCD) [13]. A CCD is a circuit etched onto a silicon surface, consisting of arrays of photosensitive elements known as pixels. CCD detectors can be intensified by a microchannel plate (MCP). As shown in Fig. 1.5b), this results in a detector known as intensified CCD (ICCD). In this device, incoming photons in the photocathode generate free electrons. These electrons are accelerated toward the MCP due to the electric field. The MCP consists of small glass channels internally coated with electron-emitting material, serving as electron multipliers. Each accelerated electron, carrying kinetic energy, can free up to 10^3 electrons as it travels across the channel. Subsequently, the electrons are accelerated onto a phosphor screen, converting them into photons. These photons are then guided by a fiber optic to the CCD.

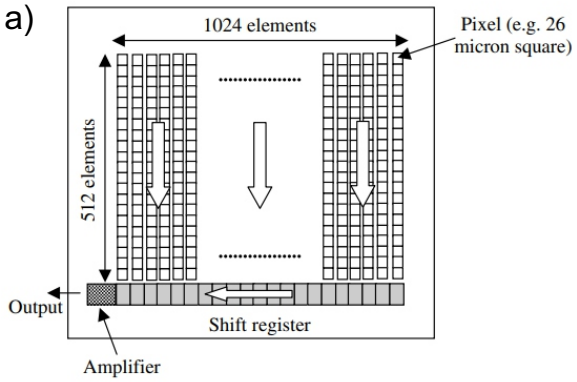

Fig. 1.6: Design of a CCD detector with 1024 × 512 pixels [12].

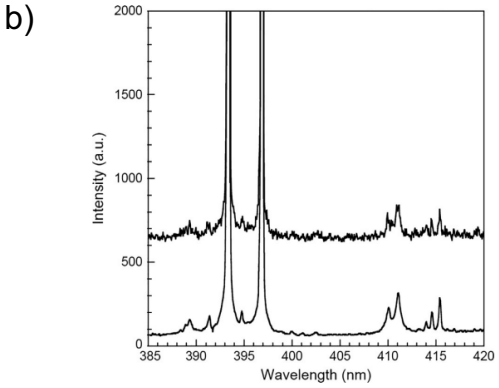

Fig. 1.7: LIBS spectra of a Ca aerosol, measured 5 μs after laser shot. Top: single-shot spectrum. Bottom: average of 200 shots [15].

In each pixel, incident photons generate free electrons, which are stored in a semiconductor region. As illustrated in Fig. 1.6, for two-dimensional arrays, these electrons undergo a vertical shift through clocked voltage until reaching the bottom row. A subsequent horizontal shift enables the final collection. This process allows the initial charge of each pixel to be recorded and sent to the computer for subsequent reconstruction and analysis [6, 12, 13]. For example, Fig. 1.7, a spatially integrated spectrum is presented. As depicted, the intensity recorded by the detector is a function of the wavelength, $I = I(\lambda)$. The principal drawback, aside from its high cost [3], of ICCD detectors is that the intensifier can introduce a significant amount of noise, which adds to the natural plasma fluctuations. As Fig. 1.7 shows, this noise can be substantially mitigated when a series of spectra is averaged [15].

With the process outlined in this section, the methodology for capturing spectral emissions from a laser-irradiated sample was explained. In addition to the basic instrumentation, the technical fundamentals of LIBS were discussed. In the following sections, the applications and the general procedure are described. It's important to note that the description of laser-induced

plasma, including its formation, evolution, properties, and its characterization have been deferred to Chapter 2 for a more in-depth description.

1.1.4 LIBS Methods

In the above section, the instrumentation commonly used in a LIBS experiment have been explained. Then, an experiment starts with sample preparation, which is minimal in LIBS. In the soil case, the typical preparation is the formation of pellets. Soil samples pass through separation, mixing, or milling processes to homogenize them, at least on a scale smaller than the LIBS spot (on the order of μm). Powders are pressed into pellets and sometimes binders should be added if the powder can't form a cohesive pellet [4, 13].

The breakdown is generated by the laser, and the radiation is collected as previously said. However, the equipment must be synchronized. This is because the plasma evolves over time and lasts for a couple of μs. Therefore, the intensity also depends on the time of observation, $I = I(\lambda, t)$. Therefore, the moment and the window of observation for the ICCD detector should be specified. Typical ICCD detectors can be programmed to initiate acquisition at a specified time after the laser shot by means of a delay generator. This time is known as gate delay, and the temporal window in which the ICCD will be acquiring and integrating the radiation is known as the gate width. Both times and its synchronization with the laser are managed by the delay generator and depend on the specific experiment [15]. Then, the spectrum recorded by a detector triggered with a delay t_d that acquires along a time width t_w is related to the intensity as

$$S(\lambda; t_d, t_w) = \int_{t_d}^{t_d+t_w} I(\lambda, t)\mathrm{d}t. \tag{1.13}$$

The number of shots also depends on the experiment. However, Figure 1.7 shown that signal quality can be improved with a series of shots. Furthermore, as the figure shows, the result will be a spectrum. In this spectrum, each atomic transition can be identified by its wavelength. In Chapter 2, the form of the spectrum in Eq. 1.13, and the information on the plasma that can be obtained from it is detailed. The next section presents the utility of the procedures described here and the general importance of LIBS.

1.1.5 Applications

With the atomic spectra, LIBS is able to provide information about the composition of substances and materials, independently of their aggregation state. With the addition of in situ measurements, the growing interest in LIBS in recent years can be seen in the vast scope of its applications. Here, some of the most recent applications of LIBS are briefly illustrated.

One of the most recent and exotic applications of LIBS is residing in space. *Tianwen-1* and Curiosity rovers have included LIBS equipment to support their investigations regarding chemical and mineral data on Mars. In contrast to previously used systems, LIBS is capable to perform analysis in far targets (up to 7 m of the instrument) and study a larger amount of samples (ChemCam studied over 400 geological targets in its first 3 months of operation).

The aim of these instruments is to investigate elemental concentrations, detection of hydrated minerals and remote rock identification [5, 6]. In Earth, LIBS has been playing a part studying the cultural heritage of humanity since the 1990s. Despite how competed this field is, LIBS stands out as a micro-destructive technique with no sampling [7]. LIBS has traced elements in pottery, being capable of distinguish the provenance of ceramics based on the chemical groups in the samples [18]. The pigment analysis has allowed LIBS to distinguish painting materials pre and post restoration in samples ranging from Ethiopian prehistoric to Byzantine paintings [7]. However, one of the most successful involvements of LIBS yields in the study of geological and metallic samples. Offering the possibility of fast and remote analysis on untreated samples, LIBS has been used in a wide range of scenarios, such as bronze and aluminium alloy analysis, analysis of iron ore, monitoring steel casting, identification of surface defects, analysis of underwater alloys, monitoring gold finesse in precious alloys and more [7, 19]. In addition to metals, LIBS was also used to analyse, identify, and classify geological samples such as vanadite, pyrite, garnet, and quartz. Also, LIBS is a popular method for geochemical fingerprint analysis and geological imaging [7].

Regarding the soil, LIBS is able to classify soild based principally due to quantification of organic and inorganic matter, ph and humidification degree. However, the principal application of LIBS with respect to soil science is in the analysis of toxic elements. LIBS has been applied, for example, in the remediation process of soils contaminated with chromium metals and in oil-spilt water. This is important because the acceleration of human development has been generating massive pollutants to the soil and atmosphere. Thus, LIBS is a growing technique in the ambient field, with a wide range of elements detectable and with great real-time and large-scale potential. This, principally due to the fact that competing techniques require additional preparation, are time consuming and impractical [6, 7, 20]. Furthermore, the anthropogenic contamination also scales to the product of the soil, the food chain. LIBS has been used to assess quality control by identifying toxic elements such as Hg, Pb, As, and Cd. In addition, elemental concentration studies have been conducted to prevent adulteration and evaluate nutritional control in aliments such as meat, flour, rice, coffee, honey, milk, maize, wine, tea, edible colourants, and salts, etc. Furthermore, LIBS has been used to study biological contaminants in food, such as *Escherichia coli, Salmonella enterica, Staphylococcus aureus,* among other dangerous bacteria and even viruses [7].

Also, as a health interest, LIBS has been applied to bioimaging, with analysis in plants, animal and human tissues. Some examples of the tissues studied are teeth, kidney, skin, brain and liver. LIBS has achieved spatial resolution down to 500 nm. Which has shown viability to the bioimaged analysis of tumours and cancerous tissues; focusing on elements such as Mg, Ca, C, K and Na. In addition, LIBS has shown the potential to characterize diseases such as hepatic fibrosis and identify a wide range of cancer tissues such as melanomas and carcinomas [7, 15, 21].

Finally, another LIBS application for safety and health lies in the nuclear field. In the nuclear-fusion industry, LIBS has been utilized for the analysis of the nuclear field in each of its stages, such as ore , fresh fuel, spent fuel, reprocessed material, and waste. The principal elements studied are U and Th, along with the principal waste elements: Ge, Sr, Mo, La, etc. In this field of application LIBS has been growing due to its remote and real-time capabilities. Furthermore, it has been demonstrated that LIBS can be used to analyze isotopes, being able to distinguish uranium (^{235}U and ^{238}U), and to determine the ratios in plutonium isotopes (^{239}Pu to ^{240}Pu) [7].

In the other hand, nuclear fusion programs such as the International Thermonuclear Experimental Reactor (ITER) require specific containers for fusion plasma. Hence, plasma-wall interactions present a major concern because of the possibility of material erosion and the deposition of impurities. LIBS can provide means of real-time monitoring of changes in the composition of plasma-facing components, mainly studying W, C, Mo, and H isotopes [7, 22].

The purpose of this section was to expose the wide application range of LIBS. As showed, LIBS in principle is capable of detecting all elements (and even its isotopes) in whichever state they are. Additionally, being a real-time, in-situ and fast technique with minimal sample preparation and minimal damage to the sample, guarantees LIBS a great niche of application and the potential to compete with traditional techniques. However, none of the detection limits (Limit of detection, LOD) for the elements were presented. Which, in fact, are also minimal. In addition to matrix effects, the main disadvantages of LIBS are its low sensibility and poor LOD, compared to traditional spectrometry techniques such as atomic absorption spectrometry (AAS), X-ray fluorescence (XRS) or inductively coupled plasma (ICP) [7]. For example, it has been reported that LIBS can detect elements in the range of µg g^{-1}, yet ICP can detect elements in the range of µg kg^{-1} [23].

Hence, it is of great importance to ensure means to improve the LOD in LIBS experiments, to overcome one of its principal limitations. In the next section, the procedures to achieve a signal enhance in LIBS are presented.

1.2 Signal-enhancing processes in LIBS

In the last section, some of the application of LIBS were exposed. These applications benefit from the atomic emission of the plasma components. However, the relatively low LOD of LIBS is a drawback for most of its applications. To improve this, there are several methods to enhance LIBS signal. The most used is the dual-pulse LIBS, in which a second pulse (which can be the same laser or a secondary one) is fired to re-excite the plasma. In this configuration, the secondary pulse interacts with the plasma plume. According to some authors, in this technique the enhancement of the signal is due to a pressure reduction induced by the second shock [6, 15]. In addition, the use of an external magnetic field has been explored to confine the plasma and enhance its emission by an increase in the radiative recombination in the plasma [24, 25]. In recent years, the possibility of improving the LIBS signal by means of nanoestructure deposition has been explored. For example, the use of metal nanoestructures can enhance the signal by more efficient ionisation and atomization, due to plasmonic coupling [7].

In this work, two enhancement techniques are of interest. Heating of the sample and the application of a high-voltage discharge to re-excite the plasma. Thus, in the following sections the characteristics and usage of these techniques will be addressed. In addition, as these techniques have been demonstrated, the most relevant literature will be reviewed. The last section provided a general overview of some applications. As said, the experimental needs and conditions, along with the spectral results and plasma properties (as is shown in this section), are heavily dependent on the target properties. Therefore, it is necessary to define a specific range of application for this study. The interest of this work is in the soil and the environment.

This choice is guided by two key factors. First, the low amount of studies regarding soils, as exposed previously. This, because metals such as aluminium are the typical LIBS targets due to their homogeneity and atomic emission range. The second reason is the importance of this application area. As mentioned before, soil pollution is a critical issue with implications not just for agriculture and the environment, but also one that has been on the rise. Therefore, this work places particular emphasis on the works carried out with contaminants in soils with the proposed techniques.

1.2.0.1 High-voltage discharge

The use of LIBS assisted by a high-voltage discharge has been shown to improve line emission. Typical experiments use one or two electrodes to re-excite the plasma, with one electrode for metal samples and two electrodes for dielectric samples. In the case of metal samples, the sample acts as the anode.

In this section some of the previous works with this technique are reviewed. The enhancing effect of a high-voltage discharge on LIBS has been studied by multiple researchers such as Bol'shakov et al. [26], Nassef et al. [27] and Hassanimatin et al. [28]. In [26] the authors used copper electrodes and currents in the mA range and voltages of a few kV, applied a few microseconds after the laser pulse. In their study, it was found a significant enhancement in SNR in the emission of LIBS assisted by a high-voltage discharge. Although it was reported that an excessive electric power may lead to excessive electrode sputtering. Reference [27] reported similar results using cylindrical W electrodes. In that work, an increase in emission intensity, volume and plasma lifetime without a significant rise in removed matter was observed. It was concluded that the increase in emission was due to an extended lifetime of the plasma and its increased volume. In the study [28], the authors explored the physical parameters that can affect the atomic emission and the mechanisms behind the enhancement of the signal. In that work, the intensification with high-voltage discharge and lower laser energies was improved. It was concluded that the parameters that lead to changes in plasma emission are its temperature and the number of emitters.

One way to characterize the discharge system is by the form of the discharge tube. For example, in the aforementioned studies the configurations are similar, with two electrodes and plasma formation between them. This setup is referred as V-shaped configuration[3] and is depicted in Fig. 1.8b). Also, alternative configurations have been studied.

Configurations as represented in Fig. 1.8a) were studied by Sobral et al. [31] and Robledo-Martinez et al. [32]; while Wang et al. [30] compared the configurations shown in Fig. 1.8b) and Fig. 1.8c). In the configuration of Fig. 1.8a), typically the target works as a cathode. In this configuration, in the reference [32] the authors investigated the impact of the delay between the laser pulse and discharge. It was observed that low discharge delays resulted in less intensification, while at higher delays, up to 20-30 µs, the intensity decays. Their study reported a difference in intensity based on each element's ionization with ionic lines in Al and Mg showing over one magnitude order higher intensification than neutral lines. Measurements of

[3]This is the configuration used in this work.

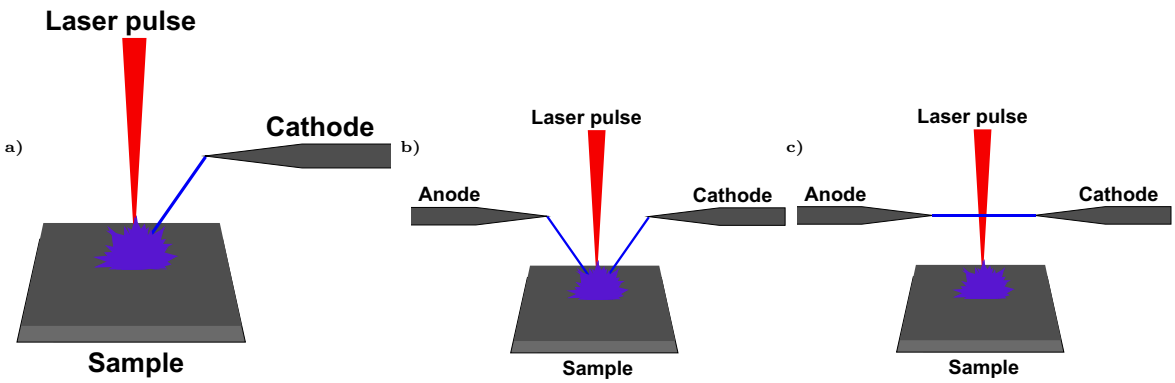

Fig. 1.8: Commonly configurations for the discharge tube. a) One electrode b) V-shape configuration c) Parallel configuration. Design based on [29, 30].

electron density and temperature showed initial increases with discharge application, followed by a decrease over time. Thus, it was concluded that the enhancement was due to a plasma reheating by the discharge, which leads to an enhance of ionization. In the reference [31] similar results, regarding the plasma parameters (temperature and electron density) are reported. Using filtered images, the authors observed a shift in both ionic and neutral species toward the sample while the discharge was applied, which was an indicative of downward plasma displacement. For the comparison in the reference [30] two W needles were used as electrodes. It was found that the V-shaped configuration resulted in higher intensification for aluminium alloys and brass. In that work, more mass removal with the V-shaped configuration than with the parallel one was reported. Also, it was observed that increasing the distance between the electrodes in the V-shape configuration leads to the parallel configuration. Also, the V-shaped configuration exhibited more mass removal than the parallel one. It was concluded that, for the specified materials, the intensification is higher with the V-shape configuration. These works may suggest that the applied discharge on LIBS does not increase the removal of matter but temporarily increases temperature and electron density. This increase in temperature apparently leads to an emission enhancement. However, with the exception of [29], these studies focused on metallic samples. Thus, the case of soils needs to be specifically addressed. This case was investigated by researchers such as Li et al. [33], Li et al. [34], Li et al. [35], Wang et al. [29], Li et al. [36] and Amador-Mejía et al [9]. In the study [33], a V-shaped electrode configuration with wolfram alloy electrodes and an 11 kV voltage was implemented. Their oscillating current led to enhanced emission for various elements, with reported enhancement factors ranging from 10 up to 223. Also, with the discharge, it was possible to measure lines that were not detected with only LIBS such as As I and Co I. Similar results were reported in the reference [35] where enhanced Pb I lines and the detection of As I, not observable with LIBS alone, were reported. Additionally, the investigation found no significant difference in removed matter between LIBS and LIBS assisted with high-voltage discharge. The reference [34] studied the enhancement of metals in soil using standard analysis powder samples. The authors demonstrated an improved LOD, specifically in magnesium lines. In the study [29], it was suggested that the discharge, applied before the laser, created a low-pressure zone. This lead to an increased sample temperature and electron density, with minimal additional matter removal at higher voltages. In the reference [36], it was investigated temperature and electron density in LIBS plasma with high-voltage discharge, using standard powder samples. While the temperature increment with the discharge was minimal, electron density showed a monotonic increase with higher applied voltage.

Recently, in [9][4] it was investigated the signal enhancement on LIBS with an applied high-voltage discharge to study contaminants in soils. Soil samples were certified loam soil reference materials. Two hemispherical capped rods with 6 mm in diameter, made of brass alloy were placed 2 mm above the target and with a gap of 5 mm between them. To re-excite the plasma, the discharge was triggered 1.5 µs after the laser. The time-damped oscillatory current reached a maximum of 190 A and 12 kV at the start. The discharge lasted for about 10 µs, delivering about 220 mJ of energy to the plasma. The LOD enhancement ranged, from 0.5 in species as Cr I to 3.1 in species such as Cd II. In the characterization of the plasma, it was demonstrated that the temperature increases lightly with the discharge. Similarly, when the discharge is triggered, the electron density increases by a factor of two. However, it decreases and reaches values similar to those of only LIBS experiments. Additionally, it was observed that the high-voltage discharge do not increases removed matter. It was concluded that the signal enhancement was a result of reheating on the plasma mainly because of the increased temperature, which provides more ions that can emit.

These works have demonstrated that it is possible to enhance the LIBS signal by an applied high-voltage discharge. However, it is not explained how the discharge interacts with the plasma and how it affects its internal composition. In this work, plasma parameters are spatially and temporally resolved to understand how the plasma changes internally when the discharge is applied. Now, a similar approach will be given to the enhance by increasing the sample temperature.

1.2.0.2 Sample heating

Sample heating as a signal-enhancing method in LIBS has demonstrated capabilities [9], although it is less studied than other techniques. Most studies focuses on metallic samples, heating them to a hundreds of degrees. In this thesis, the experiments are performed with two sample temperatures, 22 and 400 °C. Then, some of the relevant literature should be addressed.

Some of the researches conducted with sample heating were carried out by Tavassoli et al. [37], Eschlböck-Fuchs et al. [38], Sanginés et al. [39], Liaqat et al. [40], Lednev et al. [41], and Robledo-Martinez et al. [42]. In the reference [37], the authors investigated LIBS on an aluminium alloy at temperatures of 30, 100, and 150 °C. It was reported a maximum 40% increase in intensity at 150 °C, attributing this enhancement to elevated sample temperature leading to more ablated material and a higher plasma temperature. Similar findings were reported in the research [38], where higher sample temperatures resulted in a larger plasma plume and increased LIBS signal, attributed to reduced ambient density and higher ablation rates. In [39] it was correlated increased ablation rates, caused by reduced reflectivity at higher temperatures, with emission enhancement. Similarly, in the reference [40], it was reported an increase in electron density with heating, contributing to emission enhancement. In [41] the authors observed increased electron density in molten samples. Despite higher electron density and emissivity, the LOD did not change, attributed to the prevention of oxide layer formation by an Ar atmosphere. The study [42] focused on dielectric samples, specifically clay pottery ceramic discs, locally heated with a CW laser diode. It was reported increased emission intensity, SNR and plume volume

[4]This is the research, by our group, in which this work is based.

when heating the sample, with higher electron density initially and subsequent reduction as the plume expanded. There are few studies with soils at different temperatures. Umar et al. [43] studied soils contaminated with lead powder. The study revealed that both the emission intensity and the limit of detection for lead increased with higher sample temperatures. The authors attributed these findings to the enhanced ablation efficiency achieved through sample heating. In the work by our group [9][5], Amador-Mejía et al. investigated the effect of sample heating in soil samples. The samples consisted of loam soils with known elements and contaminant traces. The authors employed certified reference material as samples to maximize the relation with real soils. It was studied two sample temperatures: 22 and 400 °C. When the sample was heated, it was achieved an enhance in LOD of at least 1.3 in species such as Cd II and up to 3.4 with species like Cr II. No dependence in electron density or plasma temperature with respect to the sample temperature was found. It was reported an increase in removed matter up to 6 times with respect to the room temperature sample. Also, the plasma lifetime was observed to be longer, monitoring it up to 70 µs. The emission enhance was a result of more matter removed, because the plasma has more emitters on it. It was concluded that the reduction on air density increased the plasma volume, which in addition with the number of emitters in the plasma yielded an emission increase.

Additionally, it has been pointed that spectra acquired at high temperature may be different with respect to those acquired at room temperature, principally due to an increase in the spectral background [44]. Thus, qualitative analysis performed with LIBS may require different calibration curves or models. For example, Chang et al. [44] proposed an analysis method based on functional data analysis (FDA). It was observed to significantly decrease the error, in elemental quantification with LIBS, at different sample (high-alloy steel certified standards in that work) temperatures due to the background.

In conclusion, these previous works may suggest that heating the sample leads to an increase in the matter removed. As a result, the more emitters there are in the plasma, the more line emission is achieved. Hence, heating the sample is an effective and low-cost enhancing technique for LIBS without a significant extra sample preparation. However, the physical internal processes in the plasma are not well understood. Studies differ in whether heating the sample produces a hotter or more dense plasma than room-temperature LIBS. To understand that aspect, it is fundamental to study the internal species in the plasma. In this work, changes in the internal distribution of plasma species will be addressed. Additionally, to better understand how the plasma changes over time when the sample is heated with respect to the room-temperature case, its morphology will be investigated. Nevertheless, it should be noted that up to this section, concepts such as "plasma temperature", "plasma density", and similar terms were used freely with no further explanation. However, it is not trivial to define properties such as the temperature of collective systems such as a plasma. Thus, in the following chapter the temperature and density of the laser-induced plasma are defined. In addition, the procedures to measure them from the plasma emission are detailed.

[5]As mentioned earlier, this is the research which this work follows. Then, the same samples and parameters are used here.

Chapter 2

Laser-induced plasma

In this chapter, a general description of the plasma is presented. The chapter starts with a brief presentation of plasma physics, focusing on the main parameters that describe and define a plasma. It includes a presentation of the criteria to classify a plasma regarding its ideality and classicality state. Furthermore, a thermodynamical description is presented, which allows to introduce the statistical distributions used to describe the plasma and its parameters. Then, a brief description on the ablation process and the plasma evolution is described. Also, plasma spectroscopy is explained with the objective to obtain the relation between the state of the plasma and its emitted radiation. With this, a brief mention on the line broadening mechanisms is presented. Then, these data are used to obtain the expression for the electron density. The model known as local thermodynamic equilibrium is then presented as an alternative to the thermodynamic equilibrium. Its criteria of application are briefly explained. Finally, the derivation of the Saha-Boltzmann equation is completed and the Saha-Boltzmann method is presented as a way to compute the temperature of the plasma.

2.1 Fundamental plasma physics

The term *plasma* (Greek πλασμα for "molded" or "formed" [45, 46]) is used to denote an ionised gas. It includes free electrons, ions, neutral atoms and even molecules. Hence, a plasma is characterised by the large number of charged particles and the collective behaviour of all its components [47, 48].

2.1.1 Plasma parameters

A plasma is characterised by three parameters: particle density N, species temperature T, and magnetic field B [45]. However, in the case of an enclosed plasma, for example in a cavity with walls at constant temperature; it state is of complete thermodynamic equilibrium. Without the walls, radiation and heat conduction results in heat dissipation, which can be compensated by heating the plasma [49]. Hence, if the plasma is not enclosed, its description depends on a large array of variables.

In this section, the description of the parameters used to specify the state of a plasma are addressed. In the case of density and temperature, it should be noted that even if the species have a collective behaviour, they are not supposed to be in equilibrium. Therefore, the density and temperature of the species α will be denoted as N_α and T_α, respectively. In this work, i is used for ions and e for electrons. In addition, densities are measured in m^{-3} and temperatures in K. Unless otherwise specified, *MKS* units are used for all the rest of the constants and variables throughout this work.

However, despite plasma being a collection of positive and negative charges, it is typically electrically neutral. Actually, most plasmas are said to be quasineutral [45]. For example, suppose a plasma with a region (a sphere) far from neutrality, with all the electrons removed. Hence, let be r_m this maximum radius in which there are only ions [45]. The energy density in this sphere is

$$U = \frac{1}{2}\varepsilon_0 E^2(r), \tag{2.1}$$

where ε_0 is the permittivity of free space and $E(r)$ the electric field in the radial coordinate. In this case,

$$E(r) = \frac{Q}{4\pi\varepsilon_0 r^2}, \tag{2.2}$$

with the charge enclosed Q. Considering only n_i ions, the charge in a sphere with radius r is

$$Q = 4\pi e r^3 N_i, \tag{2.3}$$

with e the fundamental charge. Thus, the work required to assembly this sphere is

$$W = \int U r^2 \mathrm{d}r\mathrm{d}\Omega = 4\pi \int_0^{r_m} U r^2 \mathrm{d}r = \frac{2N_i^2 e^2 \pi}{45\varepsilon_0} r_m^5, \tag{2.4}$$

where $\mathrm{d}\Omega = \sin\theta \mathrm{d}\theta\mathrm{d}\varphi$ is the solid angle differential. It should be noted that this is the case with all the electrons moving radially outward. Now, in the initial case, the sphere had an average of $\frac{4}{3}\pi r_m^3 N$ particles. As and ideal gas, each particle has a mean internal energy of $\frac{3}{2}k_B T$, where k_B is Boltzmann's constant. Thus, the initial energy of the system is

$$W_0 = 2nk_B T\pi r_m^3. \tag{2.5}$$

Therefore, the relation between r_m and temperature can be obtained by equating the initial energy with the potential energy of the sphere. Supposing $N = N_i = N_e$,

$$r_m^2 = 45\frac{\varepsilon_0 k_B T_\alpha}{N_e e^2}. \tag{2.6}$$

Consequently, this is the maximum radius at which electrons could be removed spontaneously. Hence, it can be concluded that the plasma will remain quasi-neutral up to this scale length [45].

Now, it is show how the factor in the right side of Eq. 2.6 is also related to the screening of charges in a plasma. Let a test particle with charge q_0 slowly add to a spatially uniform neutral plasma, at the origin of coordinates $\boldsymbol{r} = 0$ [45]. The Poisson equation for the scalar potential is

$$\nabla^2\phi(\boldsymbol{r}) = -\frac{\rho(\boldsymbol{r})}{\varepsilon_0}, \tag{2.7}$$

where ρ denotes the charge density, which has two contributions: the charge's own density $q_0\delta(\boldsymbol{r})$ and the polarization charge density $\rho_p(\boldsymbol{r})$.

To account for the density of polarisation, each species is assumed as a fluid [45] with pressure $P_\alpha = N_\alpha k_B T_\alpha$, a mass m_α, and a mean velocity $\boldsymbol{u_\alpha}$. Therefore, the motion equation is as follows:

$$m_\alpha \frac{\mathrm{d}\boldsymbol{u}_\alpha(\boldsymbol{r})}{\mathrm{d}t} = q_\alpha \boldsymbol{E}(\boldsymbol{r}) - \frac{1}{N_\alpha}\nabla P_\alpha. \tag{2.8}$$

Invoking the slow and electrostatic approximation and supposing that the temperature is uniform, it reduces to and adiabatic response [50]

$$N_\alpha q_e \nabla\phi(\boldsymbol{r}) = -k_B T_\alpha \nabla N_\alpha(\boldsymbol{r}), \tag{2.9}$$

which gives a Boltzmann relation for the density $N_\alpha(\boldsymbol{r})$

$$N_\alpha = N_{\alpha 0}\exp\left(-\frac{q_\alpha\phi(\boldsymbol{r})}{k_B T_\alpha}\right), \tag{2.10}$$

where $N_{\alpha 0}$ is the density before the perturbation. Assuming that the potential is small compared to the thermal energy, Eq. 2.10 is expanded in its Taylor series. Up to first order, it gives

$$N_\alpha \approx N_{\alpha 0}\left(1 - \frac{q_\alpha\phi(\boldsymbol{r})}{k_B T_\alpha}\right), \tag{2.11}$$

and thus the polarization density is approximated as

$$\rho_p(\boldsymbol{r}) = \sum_\alpha q_\alpha N_{\alpha 0}\left(1 - \frac{q_\alpha\phi(\boldsymbol{r})}{k_B T_\alpha}\right). \tag{2.12}$$

In 2.12, the first term, $\rho_{p0} = \sum_\alpha q_\alpha N_{\alpha 0}$ is the condition of quasi-neutrality. Thus, $\rho_{p0} = 0$.

Therefore, Eq. 2.7 is

$$\nabla^2\phi(\boldsymbol{r}) = -\frac{1}{\varepsilon_0}\left(q_0\delta(\boldsymbol{r}) - \sum_\alpha \frac{N_{\alpha 0}q_\alpha^2}{k_B T_\alpha}\phi(\boldsymbol{r})\right), \tag{2.13}$$

which can be written as

$$\nabla^2\phi(\boldsymbol{r}) - \frac{1}{\lambda_D^2}\phi(\boldsymbol{r}) = -\frac{q_0}{\varepsilon_0}\delta(\boldsymbol{r}), \tag{2.14}$$

and solved as

$$\phi(\boldsymbol{r}) = \frac{q_0}{4\pi\varepsilon_0 r}\exp\left(\frac{-r}{\lambda_D}\right) \tag{2.15}$$

by defining the *effective Debye length* as

$$\frac{1}{\lambda_D^2} = \sum_\alpha \frac{1}{\lambda_{D\alpha}^2}, \tag{2.16}$$

and the Debye length of the species α as

Debye length

$$\lambda_{D\alpha}^2 = \frac{\varepsilon_0 k_B T_\alpha}{N_{\alpha 0} q_\alpha^2}. \tag{2.17}$$

Therefore, only for distances far greater than the effective Debye length $r << \lambda_D$ the plasma has a cloud charge that screens the test particle.

On the other hand, now it is clear that the factor on the right side of Eq. 2.6 is the Debye length for the electrons. Thus, the plasma is quasi-neutral for scale lengths greater than the electronic Debye length. From this point on, in this work, that distance is referred just as the Debye length λ_D. This, because its principal component is, usually, due to electrons. In addition, in all these calculations, it is supposed that

$$\lambda_D \ll L, \tag{2.18}$$

with L as the plasma dimension. i.e., the collective interactions are due to the bulk plasma and not to boundary effects [50]. Furthermore, the number of particles in a sphere with a radius of Debye length

$$N_D = N_e\frac{4}{3}\pi\lambda_D^3 \tag{2.19}$$

is defined as the Debye particle number or plasma parameter [47]. The reason for calling it the plasma parameter is that if

$$N_D \gg 1, \tag{2.20}$$

it follows that

$$\frac{4}{3}\pi\lambda_D\frac{\varepsilon_0 k_B T_e}{e^2} \gg 1. \tag{2.21}$$

Then

$$k_B T_e > 3\frac{e^2}{4\pi\varepsilon_0\lambda_D} > -e\phi(\lambda_D), \tag{2.22}$$

which validates the assumption of the potential energy smaller than the thermal energy, used to get 2.11. Then, both 2.18 and the condition in 2.20 are usually taken as necessary conditions for an ideal plasma. To formalise the ideality criterion in a plasma, the mean distance between particles r_s is defined by

$$\frac{4}{3}\pi N_e r_s^3 = 1. \tag{2.23}$$

i.e., the length at which a sphere of such a radius has only one electron. Then, the condition of ideality in a singly ionized plasma, is defined by the parameter of ideality Γ as

$$\Gamma = \frac{e^2}{4\pi\varepsilon_0 r_s k_B T_e} \ll 1. \tag{2.24}$$

This condition expresses the dominance of the kinetic-thermal energy over the Coulomb interaction energy. A plasma in this regime is called an ideal plasma [50, 51]. This criterion is valid only if the plasma is classical and not a quantum one. The latter is the case in which the electrons or ions are hardly at distances close to the thermal electron de Broglie wavelength [51]

$$\lambda_e = \sqrt{\frac{2\pi\hbar^2}{m_e k_B T_e}}. \tag{2.25}$$

Thus, using the radius at which the mean energy of the ion-electron interaction is $k_B T$,

$$\lambda_e \ll \frac{Ze^2}{4\pi\varepsilon_0 k_B T}, \tag{2.26}$$

becomes the condition for a classical plasma; with Z as the atomic number [51].

Therefore, a plasma that satisfies both 2.24 and 2.26 is called a classical plasma with weak interaction between ions and electrons. Furthermore, 2.24 can be extended to interaction of ions by $\Gamma_{zz} = Z^{\frac{5}{3}}\Gamma$ and the interaction of electrons and ions by $\Gamma_{Ze} = Z^{\frac{2}{3}}\Gamma$.

In all these calculations it is supposed that the plasma has two components. It can be extended to considerate, for example, the interactions with atoms in the case of the classical criterion. However, the physics remains the same. It is necessary that the plasma has a low thermal energy compared to, for example, the Rydberg energy $Ry \approx 13.6$ eV [51]. Hence, when those criteria are satisfied, it is possible to assume that the plasma is a mixture of ideal gases, and ideal gas theory can be used to determine the thermodynamic properties of the plasma [51].

2.1.2 Plasma thermodynamics

This section provides the framework for investigating how the particles in a plasma are distributed as a function of their thermodynamic properties.

Consider first a particle group in the bulk plasma. For example, of various Debye numbers. If the plasma has weak interactions, according to the previous section, it is possible to consider it as a system immersed in a reservoir. Actually, it is more appropriate to consider the plasma as the system and the external medium as the reservoir, as the effect of the plasma in the medium of, e.g., a laboratory should be negligible. Nevertheless, in Sec. 2.3.5 it is explained how a local description is more accurate for the LIBS plasma. Then, the local descriptions are used as possible.

Thus, it is possible to use the canonical ensemble to study how the energy states of the system are distributed, by supposing the bulk plasma has an energy of E_p and the total energy is E. If the system is in a state with energy E_m, $E_p = E - E_m$. Then, the total possible states

for the reservoir are $\Omega_p(E_p) = \Omega_p(E - E_m)$ and the total number of states for the total system is $\Omega(E) = \sum_m \Omega_p(E_p)$. Taking the natural logarithm of Ω_p, $\ln \Omega_p(E_p)$. As a reservoir, its energy is sufficiently greater than E_m to approximate it by E [52]. Thus, expanding with Taylor's theorem around E up to the first order,

$$\ln \Omega_p(E_p) \approx \ln \Omega_p(E) + \frac{\partial}{\partial E_p} \left[\ln \Omega_p(E_p)\right] (E_p - E) \,. \tag{2.27}$$

On the other hand, the entropy is

$$S = k_B \ln \Omega, \tag{2.28}$$

and,

$$\frac{\partial S}{\partial E} = \frac{1}{T}. \tag{2.29}$$

Hence, 2.27 yields

$$\ln \Omega(E_p) = \ln \Omega_p(E) - \frac{E_m}{k_B T}. \tag{2.30}$$

Then, the number of states for the reservoir is

$$\Omega_p(E_p)_m = \Omega_p(E) \exp\left(-E_m/k_B T\right), \tag{2.31}$$

if the system is in a state E_m.

Now, the total number of possible states (for the total system) is the sum of the possible states over each state

$$\Omega(E) = \sum_m \Omega_p(E_p)_m = \sum_m \Omega_p(E) \exp\left(-E_m/k_B T\right). \tag{2.32}$$

Thus, the probability of the state m to occur is

$$P(m) = \frac{\exp\left(-E_m/k_B T\right)}{\sum_i \exp\left(-E_i/k_B T\right)}, \tag{2.33}$$

which is the Boltzmann probability distribution.

This result can be related to the ratio of population of some state m N_m to the total population N by considering the degeneration g_m of each level [53]. i.e, for each state m it is added g_m as a statistical weight,

$$P(m) = \frac{g_m \exp\left(-E_m/k_B T\right)}{\sum_i g_i \exp\left(-E_i/k_B T\right)}, \tag{2.34}$$

which relates the population of a level m to the total population. Thus, the relative population of a quantum state m is given by the Boltzmann distribution,

Boltzmann distribution

$$\frac{N_m^z}{N^z} = \frac{g_m^z}{Z^z(T)} \exp\left(-\frac{E_m^z}{k_B T}\right), \tag{2.35}$$

where N_m, is the total density for the level m of a given energy E_m and N is the total density. Both N_m and N correspond to the same species, ions or atoms. g_m is the degeneration of level m and the partition function $Z(T)$ is defined as

$$Z(T) = \sum_i g_i e^{-E_i/k_B T}. \tag{2.36}$$

In addition, the super index z is added to indicate that the species are in the ionisation stage z. For example, $z = 0$ denotes the neutral species and $z = 1$ is the singly ionised species.

The ionisation stage is emphasised because now it is studied how different ionisation stages are related. To relate different populations, Eq. 2.35 is used. It follows that the populations of two levels m and n are related by

$$\frac{N_m^z}{N_n^z} = \frac{g_m^z}{g_n^z} \exp\left(-\frac{E_m^z - E_n^z}{k_B T}\right). \tag{2.37}$$

This equation can be thought of as the probability that a pair is in the states n and m.

These results can be extended to continuum states as they can be considered as free electrons. Taking $\mathrm{d}N_k$ as the density of free electrons in some wave number interval $k + \mathrm{d}k$, and $\mathrm{d}g_k$ the number of free electrons in that interval, Eq. 2.37 gives [53]

$$\frac{dN_k}{N_n^z} = \frac{dg_k}{g_n^z} \exp\left(-\frac{E_k - E_n^z}{k_B T}\right). \tag{2.38}$$

To calculate the free electron density, the number of modes is needed for that wave number interval. First, imposing as boundary conditions $k_i = \frac{2\pi n_i}{L}$, with L^3 the volume. Each k has $(\sum_i n_i^2)^{\frac{1}{2}}$ modes, in a sphere with $r = (\sum_i n_i^2)^{\frac{1}{2}}$ and with energy $E_k = \frac{\hbar^2 k^2}{2m_e}$. By considering the two possible values for the spin projection and g_1^{z+1} the possible degeneration for the ion ground state [54], the degeneration for the free electrons is

$$\begin{aligned} \mathrm{d}g_k &= 2g_1^{z+1} r^2 \mathrm{d}r\mathrm{d}\Omega \\ &= 2g_1^{z+1} \sum_i \left(\frac{k_i L}{2\pi}\right)^2 \mathrm{d}\left[\sum_i \left(\frac{k_i L}{2\pi}\right)^2\right]^{\frac{1}{2}} \mathrm{d}\Omega \\ &= 2g_1^{z+1} \left(\frac{L}{2\pi}\right)^3 k^2 \mathrm{d}k\mathrm{d}\Omega. \end{aligned} \tag{2.39}$$

Eq. 2.38 results,

$$\frac{dN_k}{N_n^{z-1}} = 2\left(\frac{L}{2\pi}\right)^3 \frac{g_1^z}{g_n^{z-1}} \exp\left(-\frac{E_k - E_n}{k_B T}\right) k^2 \mathrm{d}k\mathrm{d}\Omega. \tag{2.40}$$

Integrating the free electron density gives

$$\begin{aligned}\int \frac{dN_k}{N_n^z} = \frac{N_e}{N_n^z} &= \int 2\left(\frac{L}{2\pi}\right)^3 \frac{g_1^{z+1}}{g_n^z} \exp\left(-\frac{E_k - E_n^z}{k_B T}\right) k^2 \mathrm{d}k\mathrm{d}\Omega. \\ &= 2\left(\frac{L}{2\pi}\right)^3 \frac{g_1^{z+1}}{g_n^z} \exp\left(\frac{E_n^z}{k_B T}\right) 4\pi \int_0^\infty k^2 \exp\left(-\frac{\hbar^2 k^2}{2m_e k_B T}\right) \mathrm{d}k \\ &= \frac{L^3}{4} \frac{g_1^{z+1}}{g_n^z} \exp\left(\frac{E_n^z}{k_B T}\right) \left(\frac{2m_e k_B T}{\pi\hbar^2}\right)^{\frac{3}{2}} \\ &= \frac{2}{N_1^{z+1}} \frac{g_1^{z+1}}{g_n^z} \exp\left(\frac{E_n^z}{k_B T}\right) \frac{1}{\lambda_e^3},\end{aligned} \tag{2.41}$$

where the average volume per ion N_1^{z+1} was used as normalization volume.

Hence, the Saha equation is obtained as

$$\frac{N_e N_1^{z+1}}{N_n} = 2\frac{g_1^{z+1}}{g_n^z} \exp\left(\frac{E_n^z}{k_B T}\right) \frac{1}{\lambda_e^3}, \tag{2.42}$$

where the Boltzmann distribution (Eq. 2.35) can be used again to to write it with the total densities as

$$\frac{N_e N^{z+1}}{N^z} = \frac{2}{\lambda_e^3} \frac{Z^{z+1}(T)}{Z^z(T)} \exp\left(-\frac{E_\infty^z}{k_B T}\right), \tag{2.43}$$

and E_∞ is the ionisation energy for the ground state. Now, a correction for this expression must be considered.

So far, the plasma has been treated as a mixture of ideal gases. Even if this approach is reasonable, it leads to mathematical inconsistencies, reflecting its limitations. In the definition of the partition function (Eq. 2.36), while the energy shall converge, the statistical weight not. In fact, when approaching the ionisation level, the number of levels diverges [49]. Hence, since g_n depends on the principal quantum number as n^2, the partition function diverges. This arises for neglecting the Coulomb interactions. Actually, each species is subject to the field of all the other species, thus it results in a correction to the partition function. Also, the energy from the bound states between the corrected and original energies should be considered [53]. With this process, called *lowering of the ionisation energy*, the sum in the partition function becomes finite [49].

There exist different approaches to solve this problem. For example, for the Debye model of the interaction between species, in which the test particle was added to the plasma (Sec. 2.1.1). On this basis, Griem [53] obtained a first correction by considering that an atom or ion in $z-1$ needs E_∞^{z-1} for its ionisation. When this system is added to the plasma, the plasma polarisation energy should be considered for both the ion $-E_z$ and the electron $-E_1$. Thus, if they recombine, an energy E_∞^{z-1} is released. To obtain the initial state, an energy $-E^{z-1}$ is needed to remove the system from the plasma. For conservation of the total energy, the sum of these terms must be zero. Then, a correction to the ionization energy ΔE_∞^{z-1} should satisfy

$$-E_\infty^{z-1} + (-E^z - E^1) + (E_\infty^{z-1} - \Delta E_\infty^{z-1}) - (-E^{z-1}) = 0, \tag{2.44}$$

because it arises for the internal effects in the plasma.

Each energy can be calculated from the potential (Eq. 2.15) and the density (Eq. 2.12) obtained from the same model as [55]

$$\begin{aligned} E^z &= \int \rho^z(\boldsymbol{r})\phi^z(\boldsymbol{r})\mathrm{d}^3\boldsymbol{r} \\ &= -4\pi \int_0^\infty \left(\frac{ze}{4\pi\varepsilon_0 r}\right)^2 \exp\left(\frac{-2r}{\lambda_D}\right) \sum_{z,\alpha} \frac{N_\alpha^z z^2}{k_B T} r^2 \mathrm{d}r \\ &= 4\pi \left(\frac{ze}{4\pi\varepsilon_0 r}\right)^2 \frac{\lambda_D}{2} \sum_\alpha \frac{N_\alpha^z z^2}{k_B T} \\ &= \frac{z^2 e^2}{8\pi\varepsilon_0 \lambda_D}, \end{aligned} \tag{2.45}$$

where the effective Debye length was used. Using this result, the correction for the ionization energy is

$$\Delta E_\infty^{z-1} = E^{z-1} - E^z - E^1 = -\frac{z^2 e^2}{4\pi\varepsilon_0 \lambda_D}. \tag{2.46}$$

However, according to Griem [53], this expression can be simplified and replaced by a nearest neighbor algorithm, which yields

$$\Delta E_\infty^{z-1} \approx 3z \frac{e^2}{4\pi\varepsilon_0 r_s}. \tag{2.47}$$

Nevertheless, there are other approximations, some based in the deviations from ideal gas pressure and some considering ranges of density and temperature [49]. However, the variations between different models to calculate this correction are in general negligible, specifically for laboratory plasmas [49, 53]. In general, the main sources of error in this model are the deviations from thermodynamic equilibrium [53], which are studied in Sec. 2.3.5. Therefore, in this work the Saha equation is taken as

Saha equation

$$N_e \frac{N^z}{N^{z-1}} = 2\frac{Z^z(T)}{Z^{z-1}(T)} \left(\frac{m_e k_B T}{2\pi\hbar^2}\right)^{\frac{3}{2}} \exp\left(-\frac{E_\infty^{z-1} - \Delta E_\infty^{z-1}}{k_B T}\right), \tag{2.48}$$

with the correction to the ionisation energy as

$$\Delta E_\infty^{z-1} = 3z \frac{e^2}{4\pi\epsilon_0} \left(\frac{4\pi N_e}{3}\right)^{\frac{1}{3}}. \tag{2.49}$$

The Saha equation relates the density of free electrons and the densities of two different, but consecutive, ionisation stages of a single species.

In this section, a general description of the most important plasma properties was provided. Also, the main distributions, Boltzmann and Saha, were obtained. Subsequent sections deal with the specific case of a laser-induced plasma and its spectroscopic description.

2.2 Laser-induced plasma

In the last section the general plasma physics and the relevant thermodynamic equations were derived. However, the plasma and its emissions can be heavily influenced by the formation mechanism and its evolution. Thus, in this section the focus is on the formation and evolution of the plasmas that are investigated in this work: laser-induced plasmas.

2.2.1 Target ablation

The interaction between a high-power laser pulse and the target results in a temperature rise. If the laser is focused, the local irradiance produces a local heating, an evaporation of the target and plasma formation [15].

The propagation of the laser radiation onto the target is described by

$$I(z) = (1 - R)I_0 \exp(-\alpha z), \tag{2.50}$$

where $\alpha = 4\pi\,\mathbb{I}\mathrm{m}\,(n)/\lambda$ is the absorption depth of the material, n its refraction index, R its reflectivity and I_0 the laser intensity at the surface. This expression is reasonable when heat conduction is minimal compared to the depth of optical penetration [6, 13]. Then, the absorbed energy per volume in a time t is

$$-t\frac{\mathrm{d}I(z)}{\mathrm{d}z} = (1 - R)\,\alpha I_0 \exp(-\alpha z)t. \tag{2.51}$$

Taking into account the heat per unit volume $\Delta Q = \rho c \Delta T$, with ρ as the mass density and c the specific heat capacity of the material, then

$$(1 - R)\,I_0 \alpha t = \rho c \Delta T \tag{2.52}$$

is the local temperature rise in the target surface. Thus, this equation shows the relation between the target parameters and the time and energy needed to raise its temperature.

Vaporization of the target surface arises when the temperature increases substantially and reaches the critical point. Considering the solid as an ensemble of particles bounded by a potential well, the particles can escape if their kinetic energy is higher than the potential. Then, the particles escape directed normally to the target surface [6, 15].

The typical irradiances reached with a Q-switched laser, approximately $10^9\ Wcm^{-2}$, are sufficient to reach vaporization. In fact, vaporization can be reached by intensities two or three orders lower [56]. It should be pointed out that, the higher is the irradiance, more effects should be considered. One of the most important factors when vaporizing the target with a Q-switched laser is the blow-off material. As energy is carried away with the heating, the conservation of mass flow requires a proportional recession of the surface. This effect produces a recoil pressure that can raise the critical point and delay further vaporization [6, 56]. The direction of the removed matter is typically perpendicular to the surface, and is independent of the incident laser

beam angle. If the removed matter is highly heated, it can thermally radiate and this radiation can induce further vaporization at the target. In addition, re-solidified and molted material can persist on the rim of the crater and be carried away from the surface by the vapour. Furthermore, after temperature and electron density decrease, plasma colds, left matter condenses, and may crystallize [51, 56].

With nanosecond lasers, the pulse width typically exceeds the time required for thermal ablation. Further absorbing of laser radiation (with irradiances of about $10^9\ Wcm^{-2}$) by the vaporized material leads to the formation of a dense and interacting cloud of ionised gas. Thus, a plasma is formed [56, 57].

2.2.2 Plasma processes

The change from an ionized cloud to a plasma needs a critical amount of species ionized. Thus, an electronic avalanche is needed for the plasma state [7]. One of the main processes that induce the initial breakdown is multi-photon ionization. In this process, an atom absorbs (simultaneously) photons with sufficient energy to ionise it. The other process is collisional ionisation, also called cascade ionisation. Electrons energized by radiation impact neutrals, leading to their ionisation. The result is an ion and two electrons [14]. These two processes produce the seed electrons that lead to massive ionisation in the vapour cloud. In the case of dielectrics, the sudden removal of electrons from the target may cause a surface charge. The ions suffer an electrostatic repulsion that can surpass their bonding energy. This process of expulsion of ions from the target is known as a Coulomb explosion [56, 57].

As was said previously, with nanosecond lasers, each pulse lasts longer than the time needed to vaporize the target. Thus, the laser radiation interacts and energizes the cloud. This results in the free electrons absorbing photons and move higher energy states. This process is known as inverse Bremsstrahlung, and corresponds to a free-free transition and thus it produces continuum emission. In general, these three process are responsible for the medium breakdown and the plasma formation [57, 58].

There are several collisional and radiative mechanisms that sustain the plasma and are responsible for its spectral emissions. Energized free electrons can collide with ions or atoms in a level m and excite them to a higher energy level n. This process is known as collisional excitation. The inverse process can also occur. Collisions can de-excite species from upper levels to lower levels.

These two processes, along with spontaneous emission, are mainly responsible for the regulation of level populations [59]. At thermodynamic equilibrium, the level populations are described by the Saha equation. In thermodynamic equilibrium, these processes are regulated by their inverses. First, recombination arises when an electron de-ionise an ion. This process can be produced by one or two electrons. In the first case, the electron becomes bounded to the ion and radiation is released. In the other case, three-body interactions between two electrons and one ion can lead to one bounded electron and one free electron. It should be noted that both Bremsstrahlung are free-free transitions and then their radiation is also a continuum [54, 59].

All these processes, along with their respective inverse processes, can be expressed by the following relations:

- Photoionisation and radiative recombination

$$A_m^z + h\nu_{(E_{e^-} - E_m)} \rightleftarrows A^{z+1} + e^-_{(E_{e^-} + E_m - E_{ion})} \tag{2.53}$$

- Collisional ionisation and three-body recombination

$$A_m^z + e^-_{(E_{e^-})} \rightleftarrows A^{z+1} + e^-_{(E'_{e^-})} + e^-_{(E_{e^-} - E'_{e^-} - E_{ion} + E_m)} \tag{2.54}$$

- Direct and inverse Bremsstrahlung

$$A^z + e^-_{E'_{e^-}} \rightleftarrows A^z + e^-_{(E_{e^-})} + h\nu_{(E'_{e^-} - E_{e^-})} \tag{2.55}$$

- Spontaneous emission and radiative absorption

$$A_n \rightleftarrows A_m + h\nu_{mn} \tag{2.56}$$

- Collisional excitation and de-excitation

$$A_m + e^-_{(E_{e^-})} \rightleftarrows A_n + e^-_{(E_{e^-} - E_{mn})}. \tag{2.57}$$

Therefore, in general, the level populations are described by

$$\frac{\mathrm{d}N_m}{\mathrm{d}t} = -k_{ion} N_m N_e + k_{3R} N_e^2 N_A + k_{2R} N_e N_A + k_{nm} N_e N_n - k_{mn} N_e N_m - A_{mn} N_m, \tag{2.58}$$

where each k is the ratio of ionisation, three-body recombination, radiative recombination and the transitions mn; respectively. In addition, A_{mn} is the frequency of spontaneous emission. In this case, the terms corresponding to photoionisation were neglected because they are important just when the laser is radiating [59].

The processes described in this section provide information regarding plasma formation and the interactions that sustain it and its emissions. In the following section, a general description of the plasma evolution is provided.

2.2.3 Plasma evolution

Once the breakdown is achieved, the plasma evolution can be seen as its expansion against the background atmosphere, compressing it. The spatial and temporal expansion of the plasma is governed by a large group of complex phenomena. However, the expansion is typically modelled

by the Euler equations, which reflects its hydrodynamic behaviour. The experimental approach to study the expansion may involve a macroscopic observation of the expansion of the plume. In addition, it can be microscopically monitored by analyzing the number of species densities in the plasma and their ionisation stage [7, 57]. For example, plasma expansion, investigated by photographic studies, has been reported to be anisotropic. This is because, as mentioned earlier, plasma flow is typically directed from the surface with its maximum velocity perpendicular to the surface [56]. The expanding plasma and the atmosphere gas interact mainly by two processes. First, as the high-pressure plasma expands, it compresses the atmosphere, resulting in shock waves. The second are the energy transfer processes from the plasma to the atmosphere [15]. The main processes are thermal conduction, radiative transfer and the shock wave heating. The relative importance of these processes depends principally on the laser irradiance and changes along the plasma evolution. At high irradiances, shock wave transfer is the main transfer process. On the other hand, at low irradiances, the beginning of the expansion is dominated by conduction. As the plasma becomes optically thick, energy transport by radiation dominates [14].

As the plasma transport energy to its surroundings, the adjacent atmosphere is heated and its components start to absorb energy. Once a high number of its electrons are liberated, a new plasma layer is formed. The absorption layers absorb the vast majority of the laser energy in the ablation direction, shielding the bulk of the plasma from interacting with the laser radiation. This absorption and propagation process continues while the irradiance levels can support the absorption waves [14].

In the case of the shock waves, there are two directions for their propagation. First, external shock waves propagating in the background gas. Second, the scattered material forms an internal shock wave that is reflected back and forth between the front wave and the target until it decays. Then, the plasma expansion leaded by the front wave continues for a few microseconds until the gas-dynamic equilibrium with the atmosphere is reached. At this point, the pressure of the plasma is similar to that of the contact wall and the expansion is no longer produced [7, 57]. These evolutionary processes can be described in terms of the plasma parameters. In specific, with the plasma density.

Eq. 2.58 establishes three regimes for N_e [57]: $\frac{\mathrm{d}N_m}{\mathrm{d}t} > 0$, which implies ionisation dominance; $\frac{\mathrm{d}N_m}{\mathrm{d}t} = 0$ where there is equilibrium and $\frac{\mathrm{d}N_m}{\mathrm{d}t} < 0$ where recombination dominates.

The first case typically corresponds to the first stages of the plasma formation. At this point, densities $N_e > 10^{19}\, cm^{-3}$ are reached, at normal atmospheric pressures. With this high density and thus a high ionisation degree, bremsstrahlung processes dominate. Thus, the initial stages of the plasma are characterized by continuum radiation [7].

Near the equilibrium, densities are typically as $10^{16} < N_e < 10^{19}\, cm^{-3}$. In this regime, a few hundred ns after the initial breakdown, the spectra is characterized by emission transitions. The continuum and in general the contributions from radiative processes are minimal. As the deviations from equilibrium are minimal, populations are described by Boltzmann distributions. Hence, this is the regime in which LIBS analysis are performed [7].

When electron density decreases significantly, $N_e < 10^{16}\, cm^{-3}$, deviations from the equilibrium become observable. Population in low and high energy levels decouples and equilibrium can no longer be assumed[1]. At this point, emission bands from molecules can be detected [7].

Fig. 2.1 shows the emission regimes mentioned. The emission ranges are shown, along with the two man camera parameters: t_d and t_w; the time delay and the time width.

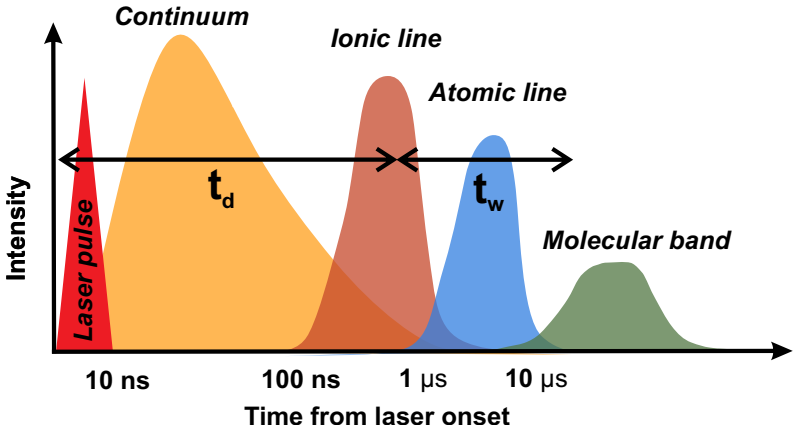

Fig. 2.1: Emission regions in the laser-induced plasma. The time scale shown is measured from the laser output. Design based on [7].

As the figure shows, in the first hundred ns from the laser output, the emission is dominated by the continuum. The line emission starts with the ionized transitions and after the first microsecond the atomic transitions dominate the emission. With the decrease in temperature and electron density, the plasma becomes partly ionised, and then may become molecular. After the first 10 microseconds after the laser output the molecular band becomes observable [51].

2.3 Plasma spectroscopy

Plasma characterisation consists of investigate the state or the parameters of a plasma. The methods used to obtain such information are known as diagnostic methods [49]. Plasma diagnostics includes several techniques for investigating plasma properties and parameters. For example, scattering of laser light across a plasma can provide information regarding the electron density and the electron velocity distribution. Another one of the most widely used diagnostic methods is the use of electrical probes [47, 60]. However, the use of probes generally comes with a disturbing effect during the measurements [49]. In this work, the diagnostic method studied is the spectral emission of plasma.

In emission spectroscopy the objective is to analyse plasma radiation, which can lead to the density, temperature, and velocity distribution of different species (electrons, ions, neutral atoms, and molecules) in plasma and its electromagnetic fields [47]. For example, wavelengths

[1] In section 2.3.5, the regime in which Boltzmann populations can be assumed is defined as Local Thermodynamic Equilibrium. The regime described here, in which deviations appear, is known as partial Local Thermodynamic Equilibrium.

and intensity in a spectral line provides information regarding the elements present and even their ionisation stage. In fact, the line intensity can even describe the plasma temperature. Furthermore, line profile may provide information regarding the kinetic temperature of emitters or the density of perturbing particles, by means of the line broadening [49]. In this section, the processes that lead from plasma emission to measurement of its physical parameters (N and T) are addressed.

2.3.1 Plasma radiation

In order to understand the plasma radiation, the processes involved should be addressed. All plasma emit and absorb electromagnetic radiation. The main sources of radiation are: bremsstrahlung, recombination radiation, and line radiation [13].

Line radiation is the main source of information about the plasma and the elements in the sample. It arises for the interaction between a particle, e.g., a charge; and a radiation field. This interaction can be described with the quantum theory of radiation fields. Following Griem [53], the Hamiltonian for a non-relativistic point electron of charge $-e$, mass m_e, and moving through a field with electromagnetic potentials $\boldsymbol{A} = \boldsymbol{A}(\boldsymbol{x}, t)$ and $\varphi = \varphi(\boldsymbol{x}, t)$ is

$$H_e = \frac{1}{2m_e}(\boldsymbol{p} + e\boldsymbol{A})^2 - e\varphi, \tag{2.59}$$

where $\boldsymbol{p}$ represent the momentum and $\boldsymbol{q}$ will be used for the coordinates components of the charge. Replacing the canonical components $\boldsymbol{p}$ with the operator $-i\hbar\nabla$ yields

$$H_e = \frac{1}{2m_e}(-i\hbar\nabla - e\boldsymbol{A})^2 + e\varphi. \tag{2.60}$$

To incorporate the quantization of the field, the Fourier expansion for the vector potential is considered as [61]

$$\boldsymbol{A}(\boldsymbol{x}, t) = \sum_{\omega}(q_\omega(t)\boldsymbol{A}_\omega(\boldsymbol{x}) + q^*_\omega(t)\boldsymbol{A}^*_\omega(\boldsymbol{x})), \tag{2.61}$$

where * denote the adjoint. Furthermore, q^* and q will act as creation and annihilation operators [54], respectively; as

$$\langle n_\omega + 1|q^*_\omega|n_\omega\rangle = \left[\frac{\hbar(n_\omega + 1)}{2\omega}\right]^{\frac{1}{2}} \exp(i\omega t), \tag{2.62}$$

and

$$\langle n_\omega|q_\omega|n_\omega + 1\rangle = \left[\frac{\hbar(n_\omega + 1)}{2\omega}\right]^{\frac{1}{2}} \exp(-i\omega t), \tag{2.63}$$

which are the only non-vanishing matrix elements.

Vector potential must satisfy the wave equation

$$\left(\frac{1}{c^2}\frac{\partial^2}{\partial t^2} - \nabla^2\right)\boldsymbol{A} = \mu_0\boldsymbol{J}, \tag{2.64}$$

and since a quantum description of radiation can be performed with only the quantization of the vector potential, the Coulomb gauge $\partial_t \varphi = 0$ is used [55]. Then, with transverse waves in vacuum and no sources, the vector potential satisfies

$$\left(\nabla_\omega^2 + \frac{\omega^2}{c^2}\right) A_\omega = 0. \tag{2.65}$$

The total Hamiltonian can be expressed as

$$\begin{aligned} H = H_e + H_f &= \frac{1}{2m_e}\left[-i\hbar\nabla + e\sum_\omega (q_\omega \boldsymbol{A}_\omega + q_\omega^* \boldsymbol{A}_\omega^*)\right]^2 - e\varphi + \sum_\omega n_\omega \hbar_\omega \\ &= -\frac{\hbar^2}{2m_e}\nabla^2 - \frac{i\hbar}{m_e}\nabla\cdot\sum_\omega (q_\omega \boldsymbol{A}_\omega + q_\omega^* \boldsymbol{A}_\omega^*) + \frac{e^2}{2m_e}\sum_\omega (q_\omega \boldsymbol{A}_\omega + q_\omega^* \boldsymbol{A}_\omega^*)\cdot\sum_{\omega'} (q_{\omega'} \boldsymbol{A}_{\omega'} + q_{\omega'}^* \boldsymbol{A}_{\omega'}^*) \\ &- e\varphi + \sum_\omega n_\omega \hbar_\omega. \end{aligned} \tag{2.66}$$

From the terms corresponding to the particle, the part that describes its interaction with the field can be identified as

$$H_i = -\frac{i\hbar}{m_e}\nabla\cdot(q_\omega \boldsymbol{A}_\omega + q_\omega^* \boldsymbol{A}_\omega^*) + \frac{e^2}{2m_e}(q_\omega q_{\omega'} \boldsymbol{A}_\omega\cdot\boldsymbol{A}_{\omega'} + q_\omega q_{\omega'}^* \boldsymbol{A}_\omega\cdot\boldsymbol{A}_{\omega'}^* + q_\omega^* q_{\omega'} \boldsymbol{A}_\omega^*\cdot\boldsymbol{A}_{\omega'} + q_\omega^* q_{\omega'}^* \boldsymbol{A}_\omega^*\cdot\boldsymbol{A}_{\omega'}^*), \tag{2.67}$$

where the summation convention was employed. Therefore, H_i has time-dependent terms. Then, it will be considered that H_i is sufficiently small to apply perturbation theory to solve the Schrödinger equation

$$i\hbar\frac{\partial}{\partial t}|\Psi(t)\rangle = H(t)|\Psi(t)\rangle, \tag{2.68}$$

where $\Psi(t)$ stands for the wave function and the Hamiltonian depends on time as $H = H_0 + H_i(t)$. Actually, for most spectroscopy applications, only the first term in Eq. 2.67 is of significant importance. The solution can be written as a combination of wavefunctions k of the unperturbed Hamiltonian

$$|\Psi(t)\rangle = \sum_k \phi_k(t)|k\rangle, \tag{2.69}$$

where the time dependence is given by

$$|\Psi(t)\rangle = \sum_k C_k(t)\exp\left(-i\frac{E_k}{\hbar}t\right)|k\rangle, \tag{2.70}$$

where E_k are the eigenvalues of H_0. Substitution in Eq. 2.68 leads to

$$i\hbar\sum_k \left[C_k(t)\left(\frac{-iE_k}{\hbar}\right) + \dot{C}_k(t)\right]\exp\left(-i\frac{E_k}{\hbar}t\right)|k\rangle = \sum_k C_k(t)\exp\left(-i\frac{E_k}{\hbar}t\right)H(t)|k\rangle. \tag{2.71}$$

Here, the product with an element of the basis, say, $\langle n|\phi_n^*$, yields in the left side of Eq. 2.71

$$\begin{aligned} i\hbar\langle n|\phi_n^*(t)\frac{\partial}{\partial t}|\Psi(t)\rangle &= i\hbar\sum_k\left[\phi_k(t)\left(\frac{-iE_k}{\hbar}\right)\phi_n^*(t)+\dot{C}_k(t)\phi_n^*(t)\exp\left(-i\frac{E_k}{\hbar}t\right)\right]\langle n\,|\,k\rangle \\ &= i\hbar\sum_k\left[\left(\frac{-iE_k}{\hbar}\right)C_k(t)\exp\left(i\omega_{nk}t\right)+\dot{C}_k(t)\exp\left(i\omega_{nk}t\right)\right]C_n^*(t)\delta_{nk} \\ &= E_n|C_n(t)|^2+i\hbar\dot{C}_n(t)C_n^*(t), \end{aligned} \tag{2.72}$$

where the frequency of transition from a state k to a state n was defined as $\omega_{nk}=(E_n-E_k)/\hbar$. The right side of Eq. 2.71 is given by

$$\begin{aligned} \langle n|\phi_n^*(t)H(t)|\Psi(t)\rangle &= \sum_k C_k(t)C_n^*(t)\exp\left(i\omega_{nk}t\right)\langle n|(H_0+H_i(t))|k\rangle \\ &= \sum_k C_k(t)C_n^*(t)\exp\left(i\omega_{nk}t\right)\left(E_k\delta_{nk}+\langle n|H_i(t)|k\rangle\right) \\ &= E_n|C_n(t)|^2+\sum_k C_k(t)C_n^*(t)\exp\left(i\omega_{nk}t\right)\langle n|H_i(t)|k\rangle. \end{aligned} \tag{2.73}$$

Therefore, the equation for the coefficients is

$$\dot{C}_{mn}(t)=-\frac{i}{\hbar}\sum_k C_{mk}(t)\exp\left(i\omega_{nk}t\right)\langle n|H_i(t)|k\rangle, \tag{2.74}$$

where the index m was added to make clear that, from Eq. 2.70, the coefficients $|C_k(t)|^2$ are proportional to the probability density at time t, $|\Psi(t)|^2$. Therefore, $|C_{mn}(t)|^2$ represents the probability of measuring a state n, at time t, with an initial state m. This interpretation will be used as an initial condition to solve Eq. 2.74.

If at $t=0$ the system is in the state m, $C_{mn}(0)=\delta_{mn}$. Using this as the zeroth-order solution, at first order the solution can be approximated as

$$C_{mn}(t)\approx\delta_{mn}-\frac{i}{\hbar}\sum_n\int_0^t\delta_{mk}\exp\left(i\omega_{nk}t'\right)\langle n|H_i(t')|k\rangle\mathrm{d}t'. \tag{2.75}$$

Now, it will be supposed that the interaction Hamiltonian varies slowly on time. This, because typically in plasma spectroscopy changes in the matrix elements of the interaction Hamiltonian are negligible over the relevant energy intervals [54]. Thus,

$$\begin{aligned} C_{mn}(t) &\approx \delta_{mn}-\frac{i}{\hbar}\int_0^t\exp\left(i\omega_{nm}t'\right)\langle n|H_i(t')|m\rangle\mathrm{d}t' \\ &\approx \delta_{mn}-\frac{i}{\hbar}\langle n|H_i|m\rangle\int_0^t\exp\left(i\omega_{nm}t'\right)\mathrm{d}t'. \end{aligned} \tag{2.76}$$

Therefore, in first order, the probability of finding the system in a state n at time t, if m was its initial state, is

$$|C_{mn}(t)|^2\approx 2\frac{|\langle n|H_i|m\rangle|^2}{(E_m-E_n)^2}\left[1-\cos\left(\omega_{mn}t\right)\right], \tag{2.77}$$

for $n \neq m$. Transition probabilities over an interval of energies will require the account of the density in the energy interval. Supposing that the total spectrum is continuous [54], then the transition probability per unit of time is

$$P_{nm} \longrightarrow \frac{1}{t}\int |C_{mn}(t)|^2 \rho_{E_n} \mathrm{d}E_n = \frac{1}{t}\int 2\frac{|\langle n|H_i|m\rangle|^2}{(E_m - E_n)^2}\left[1 - \cos\left(\omega_{mn}t\right)\right]\rho_{E_n}\mathrm{d}E_n, \tag{2.78}$$

where the integral is over all the space, and ρ_{E_n} is the density of final states per energy interval $E_n, \quad E_n + \mathrm{d}E_n$, Now, the approximation of $\langle n|H_i|m\rangle$ as a constant will be invoked again. The same can be assumed with ρ_{E_n} [53]. The resulting integral can be seen as $\int_{-\infty}^{\infty}(1-\cos(x))/x^2\mathrm{d}x$ and solved numerically, resulting in π. Hence,

$$\begin{aligned} P_{nm} &\approx \frac{2}{t}|\langle n|H_i|m\rangle|^2\rho_{E_n}\int_{-\infty}^{\infty}\frac{\left[1-\cos\left(\omega_{mn}t\right)\right]}{(E_m - E_n)^2}\mathrm{d}E_n \longrightarrow \frac{2}{\hbar}|\langle n|H_i|m\rangle|^2\rho_{E_n}\int_{-\infty}^{\infty}\frac{1-\cos x}{x^2}\mathrm{d}x \\ &= \frac{2\pi}{\hbar}|\langle n|H_i|m\rangle|^2\rho_{E_n}, \end{aligned} \tag{2.79}$$

is the probability of transition, per unit of time, from a state m to a state n. The corresponding density of final states per energy interval can be obtained analogously to Eq. 2.39. Considering only the number of modes in the solid angle element, it follows that, for a degeneracy g_n,

$$\mathrm{d}\rho_{E_n} = g_n\frac{\mathrm{d}N_k}{\mathrm{d}E_n} = g_n\left(\frac{L}{2\pi}\right)^3\frac{\omega^2}{\hbar c^3}\mathrm{d}\Omega, \tag{2.80}$$

where $\omega = ck$, for a refractive index of 1.

So far, the results obtained allow for the study of the Hamiltonian with Eq. 2.67 as a perturbation. As mentioned earlier, only the gradient term can be considered in most spectroscopy applications. Thus, one can substitute the creation term in Eq. 2.79 to obtain the probability of a photonic emission. i.e.,

$$\begin{aligned} \mathrm{d}A_{nm} &= \frac{2\pi}{\hbar}|\langle n|i\frac{\hbar e}{m_e}\nabla\cdot q_\omega^*\boldsymbol{A}_\omega^*|m\rangle|^2\mathrm{d}\rho_{E_n} \\ &= \frac{2\pi}{\hbar^2}|\langle n|i\frac{\hbar e}{m_e}\nabla\cdot q_\omega^*\boldsymbol{A}_\omega^*|m\rangle|^2 g_n\left(\frac{L}{2\pi c}\right)^3\omega^2\mathrm{d}\Omega. \end{aligned} \tag{2.81}$$

This probability per unit of time corresponds to the transition probability for spontaneous emission.

In the case of the emission to a field with empty initial modes,

$$\langle 1|q_\omega^*|0\rangle = \left(\frac{\hbar}{w}\right)^{\frac{1}{2}}\exp\left(i\omega t\right). \tag{2.82}$$

On the other hand, as A_ω must satisfy the wave equation,

$$\boldsymbol{A}_\omega = A_\omega\boldsymbol{a}_\omega\exp\left(-i\boldsymbol{k}\cdot\boldsymbol{r}\right), \tag{2.83}$$

where A_ω is the amplitude, $\boldsymbol{r}$ the coordinate vector, $\boldsymbol{k}$ and $\boldsymbol{a}$ are the propagation and polarization vectors, respectively. The amplitude of the vector potential can be obtained by equating the field energy to that of the oscillator, which gives

$$A_\omega = \left(\varepsilon_0 L^3\right)^{-\frac{1}{2}}. \tag{2.84}$$

Therefore,

$$\mathrm{d}A_{nm} = \frac{e^2\omega}{8\pi^2\varepsilon_0\hbar c^3} g_n |\langle n| i\frac{\hbar}{m_e}\nabla\cdot\boldsymbol{a}\exp\left(i\boldsymbol{k}\cdot\boldsymbol{r}\right)|m\rangle|^2 \mathrm{d}\Omega. \tag{2.85}$$

Taking the firs term in Taylor's expansion for the exponential,

$$\mathrm{d}A_{nm} = \frac{e^2\omega}{8\pi^2\varepsilon_0\hbar c^3} g_n |\langle n| i\frac{\hbar}{m_e}\nabla\cdot\boldsymbol{a}|m\rangle|^2 \mathrm{d}\Omega, \tag{2.86}$$

and replacing $i\hbar\nabla$ by $m_e\omega\boldsymbol{r}$,

$$\mathrm{d}A_{nm} = \frac{e^2\omega^3}{8\pi^2\varepsilon_0\hbar c^3} g_n |\langle n|\boldsymbol{r}\cdot\boldsymbol{a}|m\rangle|^2 \mathrm{d}\Omega. \tag{2.87}$$

Taking $\boldsymbol{a}$ and $\boldsymbol{k}$ as perpendicular, for any polarization in the plane defined by $\boldsymbol{r}$ and $\boldsymbol{k}$, $\boldsymbol{r}\cdot\boldsymbol{a} = |\boldsymbol{r}|\sin\theta$. Where θ is the angle between $\boldsymbol{k}$ and $\boldsymbol{r}$. Then, it gives for $\boldsymbol{r} = \sum_i \boldsymbol{x_i}$,

$$\mathrm{d}A_{nm} = \frac{e^2\omega^3}{8\pi^2\varepsilon_0\hbar c^3} g_n \sin^2\theta \sum_i |\langle n|x_i|m\rangle|^2 \mathrm{d}\Omega. \tag{2.88}$$

Therefore,

$$A_{nm} = \frac{e^2\omega^3}{3\pi\varepsilon_0\hbar c^3} g_n \sum_i |\langle n|x_i|m\rangle|^2 \tag{2.89}$$

is the transition probability per unit time [53].

On the other hand, spectral emission is proportional to number of emitters. And is also related to transition probability by

Emisivity

$$\epsilon^z_{mn} = A^z_{mn} N^z_m h\nu_{mn}. \tag{2.90}$$

With this expression, it is possible to understand how the plasma radiates. However, although this emission depends on a specific energy, in the next section it is shown that the spectral lines are not infinitely sharp.

2.3.2 Spectral line broadening

Previous section focused to study the radiative processes that origin spectral information of the plasma. It may seem that each transition correspond to a perfectly sharp spectral line. However, in this section it is studied how different physical process affect the width and shape of spectral lines. In this work, and as usual in the literature, the width of a spectral line corresponds to the full width at half maximum (FWHM), which is denoted as $\Delta\lambda_{1/2}$.

There are three main sources of line broadening. The first, comes from the uncertainty principles. Because energy states have finite lifetimes, thus the energy levels cannot be infinitely sharp. The second one arises from the relative movement of the emitting species with respect to the observer. Thus, the relative movement may alter the line frequency. And at last, interactions between species (mainly collisions) may reduce the lifetime of states. Then, more collisions lead to broader lines. This is the main broadening mechanism that affects LIBS plasma and, its relation to how dense the plasma is, is used to calculate its electron density [62].

2.3.2.1 Natural broadening

The first case, and the weaker one, its the natural broadening. As mentioned above, this is a result from the uncertainty principle,

$$\Delta E \Delta t \geq \frac{\hbar}{2}. \tag{2.91}$$

This is because energy levels have a finite lifetime, Δt. Thus, the energy levels of excited states are actually an energy distribution with an energy spread ΔE. Thus, although each transition has a defined energy, the line profile observed has a finite width [58, 62].

This effect corresponds to a line profile

$$\phi_L(\omega) = \frac{1}{2\pi} \frac{\gamma_{mn}}{(\omega - \omega_{mn})^2 (\gamma_{mn}/2)^2}, \tag{2.92}$$

where $1/\gamma_{mn}$ is the state lifetime. Also, it is observed that γ_{mn} corresponds to the FWHM. However, in practice this effect is negligible with respect to the other two contributions [62].

2.3.2.2 Doppler broadening

Suppose that the emitting atom has a velocity v along the line of sight. Then, from the Doppler effect there is an apparent change in line frequency as [62]

$$(\omega - \omega_{mn})/\omega_{mn} = v/c. \tag{2.93}$$

Considering also a Maxwellian distribution, the profile obtained is

$$\phi_D(\omega) = \phi_D(\omega_0) \exp\left(-\left[\frac{c(\omega-\omega_0)}{\omega_0 v_p}\right]^2\right), \tag{2.94}$$

where $v_p = \sqrt{2k_BT/m}$, with m the mass of the emitter.

Therefore, Doppler broadening gives a width

$$\Delta\lambda_D = \lambda_0 \frac{2}{c}\sqrt{\frac{2k_BT}{m}\ln 2}. \tag{2.95}$$

This effect contributes mainly in systems of low density, such as interstellar medium or high-speed rotating stars [62]. In the case of LIBS plasma, the main contribution comes from the interaction between species.

2.3.2.3 Stark broadening

The main contribution to the line broadening is the so-called pressure broadening. This effect comes from the interaction between species. Its starting point is the many body problem, in which an emitting atom is surrounded by perturbers. Thus, there is no analytical solution [62]. Pressure broadening is usually addressed by two models: impact approximation or quasi-static approximation. The latter describes fast perturbers and the former considers perturbers with negligible movement [62].

In the case of plasmas, the perturbers are usually charged particles, mainly electrons. This is known as Stark broadening. In the case of the impact approximation, the interactions with electrons are treated as collisions. These collisions may change the phase of a wave train. Then the more collisions, the shorter the lifetime becomes. This leads to a Lorentzian shape, with a total width [3, 58, 62, 63]:

$$\Delta\lambda_S = \underbrace{2w\left(\frac{N_e}{10^{16}}\right)}_{\text{Electronic interactions}} + \underbrace{3.5A\left(\frac{N_e}{10^{16}}\right)^{\frac{1}{4}}[1 - BN_D^{-\frac{1}{3}}]w\left(\frac{N_e}{10^{16}}\right)}_{\text{Ionic interactions}}, \tag{2.96}$$

where w is electron's impact parameter, which corresponds to the half of the total Stark broadening; N_e is electron density (cm^{-3}), A is the ion broadening parameter, B is a coefficient with value 1.2 or 3/4 for ions or neutrals; respectively.

If $N_D \gtrapprox 2$ and $0.05 < A\left(\frac{N_e}{10^{16}}\right)^{\frac{1}{4}} < 0.5$, Eq. 2.96 constitutes a good approximation for the line broadening [63]. Also, as said above, in typical LIBS conditions the ionic contribution could be neglected [3], and the Stark width becomes

$$\Delta\lambda_S = 2w\left(\frac{N_e}{10^{16}}\right). \tag{2.97}$$

Then, the 2w can be interpreted as the Stark width at a electron density of $10^{16}\,cm^{-3}$. With this, the electron density can be calculated, as is described in Sect. 2.3.4.

2.3.3 Line shape

In the previous sections it was shown that there exists two main line shapes, Lorentzian (neutral and Stark broadening) and Gaussian (Doppler broadening). The simultaneous Gaussian ($\phi_G(\lambda)$)and Lorentzian ($\phi_L(\lambda)$) shapes is given by the convolution

$$\int_{-\infty}^{\infty} \phi_G(\lambda' - \lambda_0)\phi_L(\lambda - \lambda')\mathrm{d}\lambda', \tag{2.98}$$

which gives a Voigt profile [58]

$$\frac{a}{\pi\Delta\lambda_G}\sqrt{\frac{4\ln 2}{\pi}}\int_{-\infty}^{\infty}\frac{\exp\left(-t^2\right)}{a^2+(x-t)^2}\mathrm{d}t, \tag{2.99}$$

where $x = \frac{\lambda-\lambda_0}{\Delta\lambda_G}2\sqrt{\ln 2}$ and $a = \frac{\Delta\lambda_S}{\Delta\lambda_G}\sqrt{\ln 2}$ specifies the relative importance of each component. Thus, in the case of LIBS spectra, usually only the Lorentzian contribution is considered.

2.3.4 Electron density

As described, one of the main plasma parameters is its electron density. This can be calculated from the line broadening, as described in Sect. 2.3.2.3. From

$$\Delta\lambda_S = 2w\left(\frac{N_e}{10^{16}}\right), \tag{2.100}$$

it follows that

$$N_e = \Delta\lambda_S\left(\frac{10^{16}}{2w}\right). \tag{2.101}$$

Then, it is possible to write the electron density as a function of the Stark width, and the electron impact parameter at a reference electron density N_r as

$$N_e = \Delta\lambda_S\left(\frac{N_r}{2w}\right). \tag{2.102}$$

Thus, to calculate the electron density it is only needed the experimental width of emission lines, which mainly corresponds to the Stark broadening.

2.3.5 Thermodynamic equilibrium

In this chapter, the plasma thermodynamics and radiation were the main subjects. In the thermodynamic analysis it was found that at thermodynamic equilibrium the plasma should, along with a Maxwellian distribution of velocities, follow Boltzmann statistics. From the derivation of Eq. 2.35, it follows that T actually corresponds to the excitation temperature T_{exc}. Also, the electrons have their own kinetic temperature T_e and the photons are described with their own temperature T_ν; say, Planck distribution. Moreover, if the discussion also involves molecules, the rotational and the vibrational temperatures should also be considered. This controversy can be solved by the assumption of thermodynamic equilibrium [64]. In this state, all these temperatures should be the same. Thus, all distributions are characterized by a single temperature, say, the electron temperature. Nevertheless, the thermodynamic equilibrium is almost impossible to reach for a laser-induced plasma. Because of spatial and temporal inhomogeneities and the lack of radiative equilibrium [64]. However, Boltzmann, Maxwell and Saha distributions can be used while the radiative emission losses are low with respect to other processes. In this context, the local thermodynamic equilibrium (LTE) is introduced as a model in which each spatial point has a local defined temperature. In this case, collisional processes dominate over radiative ones [54, 64].

Radiative equilibrium requires the plasma to be approximately a black body, but the emitted photons lead to a deviation from the Planck distribution. If the radiation losses are small in comparison to those from other processes, the Saha, Boltzmann, and Maxwell distributions are still capable of describing the system. In this case,

$$T_{exc} = T_e = T_{a,i} \neq T_\nu, \tag{2.103}$$

where $T_{a,i}$ refers to the temperature of atoms or ions. This corresponds to the regime known as LTE, in which excited states must de-excite more by collisions than by spontaneous radiation and usually requires a high electron density [65, 66].

There are several criterion to study whether the plasma is in LTE. The conditions in general depend on the characteristics of the plasma, mainly whether is stationary and homogeneous. The first case corresponds to a stationary and homogeneous plasma. Thus, without spatial gradients or time variation. In this case, LTE is reached when the rate of collision-induced transitions $m \longrightarrow n$ (X_{nm}) is higher than the radiative decay $n \longrightarrow m$ (A_{mn}) [65, 67],

$$N_m X_{nm} \gg N_n A_{mn}, \tag{2.104}$$

where N_m and N_n are the populations of their levels. Usually, it is required for the collisional rate to be at least 10 times larger than the radiative one [67]. A classical treatment of the cross sections in 2.104 results in the condition for electron density known as the McWhirter criterion [65]:

McWhirter criterion

$$N_e > 1.6 \times 10^{12} T^{\frac{1}{2}} \left(\Delta E_{mn}\right)^3, \tag{2.105}$$

where N_e (cm^{-3}) corresponds to the electron density, T (K) to the temperature and ΔE_{mn} (eV) is the energy difference between the levels n and m. However, although popular, this is only a necessary condition, that usually only says how far is the plasma from LTE [1].

If this criterion is not met, the plasma may be in a state known as partial local thermodynamic equilibrium (pLTE). In this case,there is usually a level where the rates in Eq. 2.104 are equal. As a result, the condition is met in high-energy levels, but not in low-energy levels. Therefore, upper levels can follow a Boltzmann distribution, while lower levels cannot. Thus, the excitation temperature calculated from the Boltzmann distribution may differ from the electron temperature [65].

A plasma with an electron density enough to met LTE is seldom homogeneous in space and independent of time [67]. The latter is clearly the case of LIBS plasma, in which is necessary that the changes in their parameters are small over time.

The time to compare the temporal changes in the plasma is the relaxation time τ_{rel}, defined as the time needed to establish equilibrium between ionisation and excitation. This time should be on the order of the time required to establish LTE between upper and lower states, because if the plasma transits a sequence of quasi-stationary near LTE states, most of the ionisation processes tend to occur through intermediate states. Considering the rate of excitation/de-excitation by collisions as Maxwellian,

$$X_{nm} = N_e \langle \sigma_{nm} v \rangle = 4\pi \frac{f_{nm} e^4 N_e \langle g \rangle}{\Delta E_{mn}} \left(\frac{2\pi}{3 m_e k_B T} \right)^{\frac{1}{2}} \exp\left(-\frac{\Delta E_{mn}}{k_B T} \right), \tag{2.106}$$

where

$$\sigma_{nm} = \frac{2\pi^2}{\sqrt{3}} \frac{f_{nm} \langle g \rangle e^4}{\frac{1}{2} m_e v_i^2 \Delta E_{mn}} \tag{2.107}$$

is the cross section of inelastic collisions, g is the effective gaunt factor, f_{mn} is the absorption oscillator strength of the transition, v_i the incident velocity of the electron [65].

Then, taking the rate of collisional excitation as an estimate for τ_{rel} [65],

$$\tau_{rel} \approx \frac{1}{N_e \langle \sigma_{nm} v \rangle} = \frac{6.3 \times 10^4}{N_e f_{mn} \langle g \rangle} \Delta E_{nm} \left(k_B T \right)^{\frac{1}{2}} \exp\left(\frac{\Delta E_{nm}}{k_B T} \right). \tag{2.108}$$

However, this should be taken for the excitation to the first level, because is the slowest.

Therefore, τ_{rel} can be used to study how is the temporal variation of the plasma parameters, supposing that τ_{rel} is about the time needed by the system to return to LTE after a sudden departure. Then, it is needed that this time is shorter than the time of variation of the parameters. This can be expressed, for the temperature and electron density, as [65, 67]

Temporal criteria

$$1 \gg \left| \frac{T(t+\tau_{rel}) - T(t)}{T(t)} \right| \\ 1 \gg \left| \frac{N_e(t+\tau_{rel}) - N_e(t)}{N_e(t)} \right|. \tag{2.109}$$

Hence, Eqs. 2.109 guarantees that the rates of the internal processes are higher than the variation rate of the thermodynamic parameters and thus constitute the second condition for LTE. This, in a time-dependent plasma.

When dealing with an inhomogeneous plasma, it is important to apply a similar criterion for spatial gradients. For an inhomogeneous plasma to be considered in LTE, it is necessary that the spatial gradients are small enough for an atom not to diffuse over regions of significantly different parameters within a time on the order of τ_{rel}. If this requirement is not fulfilled, the state of the atom is not related to the local values of the parameters, but to values in another region of the plasma [65, 67].

Then, defining the diffusion length as

$$\lambda_d = (D\tau_{rel})^{\frac{1}{2}}, \tag{2.110}$$

with

$$D \approx 3 \times 10^{19} \frac{k_B T}{N_e M_A}, \tag{2.111}$$

the diffusion coefficient, with M_A as the atomic mass of the species. Therefore,

$$\lambda_d \approx 1.4 \times 10^{12} \frac{(k_B T)^{\frac{3}{4}}}{N_e} \left(\frac{\Delta E_{nm}}{M_A f_{mn} \langle g \rangle} \right)^{\frac{1}{2}} \exp\left(\frac{\Delta E}{2 k_B T} \right), \tag{2.112}$$

can be taken as the diffusion length [65]. Then, in a similar spirit to the temporal criteria, the conditions for LTE at a position x can be expressed as

Spatial criteria

$$1 \gg \left| \frac{T(x) - T(x+\lambda_d)}{T(x)} \right| \\ 1 \gg \left| \frac{N_e(x) - N_e(x+\lambda_d)}{N_e(x)} \right|. \tag{2.113}$$

These criteria guarantee that the atoms or ions are described with the local values of temperature and electron density. Thus, that through the plasma, its parameters change slowly. Actually, Eq. 2.112 is an approximation to the order of magnitude and should be expected to be fulfilled within a couple of magnitude orders.

As a conclusion, in this section some conditions to consider the plasma in local thermodynamic equilibrium were presented. These criteria evaluated three important points, regarding the plasma parameters. First, the relation between the plasma parameters at a specified transition.

Second, the rate of time variation of the parameters. Finally, the magnitude of the spatial gradients in these parameters. However, it should be pointed out that these are approximations and should be asked for the plasma to satisfy them by at least a factor of 2 or 3 to account for the approximations performed, mainly for the cross sections. Nevertheless, when these criteria are met, it can be considered that the plasma may be in LTE and thus, all the distributions obtained so far can be used. In the next section, supposing LTE, the main distributions and equations are used to complete the full derivation of the Saha-Boltzmann equation, which allow for the temperature calculation.

2.3.6 Electron temperature

Once the thermodynamic distributions are derived and there is understanding on the radiative processes in the plasma, the electron temperature can be calculated. This is performed by relating the Boltzmann equation, emisivity equation and Saha equation into the Saha-Boltzmann equation.

2.3.6.1 Saha-Boltzmann method

In the context of LTE, it is possible to describe the relations between populations by the Boltzmann equation (Eq. 2.35). Substituting N_m^z from 2.35 into emissivity equation (Eq. 2.90),

$$\epsilon_{mn}^z = \frac{hc}{\lambda_{mn}} A_{mn}^z N^z \frac{g_m^z}{Q^z(T)} e^{\frac{-E_m^z}{k_B T}}, \tag{2.114}$$

and it follows that

$$\frac{\epsilon_{mn}^z \lambda_{mn}}{A_{mn}^z g_m^z} = \frac{hcN^z}{Q^z(T)} e^{\frac{-E_m^z}{k_B T}}. \tag{2.115}$$

Considering instead the line intensity and N^z from Saha equation (Eq. 2.48),

$$\begin{aligned} \frac{I_{mn}^z \lambda_{mn}}{A_{mn}^z g_m^z} &= hc \exp\left(\frac{-E_m^z}{k_B T}\right) \frac{N^{z-1}}{N_e} 2 \frac{1}{Q^{z-1}(T)} \left(\frac{m_e k_B T}{2\pi\hbar^2}\right)^{\frac{3}{2}} \exp\left(-\frac{E_\infty^{z-1} - \Delta E_\infty^{z-1}}{k_B T}\right) \\ &= \frac{hcN^{z-1}}{Q^{z-1}(T)} \left[2\left(\frac{m_e k_B}{2\pi\hbar^2}\right)^{\frac{3}{2}} \frac{T^{\frac{3}{2}}}{N_e}\right] \exp\left[-\frac{1}{k_B T}\left(E_m^z + E_\infty^{z-1} - \Delta E_\infty^{z-1}\right)\right], \end{aligned} \tag{2.116}$$

taking natural logarithm,

$$\ln \frac{I_{mn}^z \lambda_{mn}}{A_{mn}^z g_m^z} = \ln \frac{hcN^{z-1}}{Q^{z-1}(T)} + \ln\left[2\left(\frac{m_e k_B}{2\pi\hbar^2}\right)^{\frac{3}{2}} \frac{T^{\frac{3}{2}}}{N_e}\right] - \frac{1}{k_B T}(E_m^z + E_\infty^{z-1} - \Delta E_\infty^{z-1}). \tag{2.117}$$

This result allows for analyzing consecutive species $\{z-1, z\}$. To extend it to an arbitrary set of species $\{0, 1, ..., z\}$, with $z \geq 1$, it can be iterated as follows.

Substituting N^{z-1} from the Saha equation (Eq. 2.48) into 2.116. This process can be iterated up to the neutral $z = 0$. Thus,

$$\begin{aligned}\frac{I^z_{mn}\lambda_{mn}}{A^z_{mn}g^z_m} &= \frac{hcN^0}{Q^0(T)}\left[2\left(\frac{m_e k_B}{2\pi\hbar^2}\right)^{\frac{3}{2}}\frac{T^{\frac{3}{2}}}{N_e}\right]^z \exp\left(\frac{-E^z_m}{k_B T}\right)\prod_{k=0}^{z-1}\exp\left[-\frac{1}{k_B T}(E^k_\infty - \Delta E^k_\infty)\right] \\ &= \frac{hcN^0}{Q^0(T)}\left[2\left(\frac{m_e k_B}{2\pi\hbar^2}\right)^{\frac{3}{2}}\frac{T^{\frac{3}{2}}}{N_e}\right]^z \exp\left(-\frac{1}{k_B T}\left[E^z_m + \sum_{k=0}^{z-1}(E^k_\infty - \Delta E^k_\infty)\right]\right),\end{aligned} \tag{2.118}$$

taking natural logarithm,

$$\ln\frac{I^z_{mn}\lambda_{mn}}{A^z_{mn}g^z_m} = \ln\frac{hcN^0}{Q^0(T)} + \ln\left[2\left(\frac{m_e k_B}{2\pi\hbar^2}\right)^{\frac{3}{2}}\frac{T^{\frac{3}{2}}}{N_e}\right]^z - \frac{1}{k_B T}\left[E^z_m + \sum_{k=0}^{z-1}(E^k_\infty - \Delta E^k_\infty)\right]. \tag{2.119}$$

Thus, for $z \geq 1$ the Saha-Boltzmann equation is obtained as

Saha-Boltzmann equation

$$\ln\left(\frac{I^z_{mn}\lambda_{mn}}{A^z_{mn}g^z_m}\right) - z\ln\left[2\left(\frac{m_e k_B}{2\pi\hbar^2}\right)^{\frac{3}{2}}\frac{T^{\frac{3}{2}}}{N_e}\right] = -\frac{1}{k_B T}\left[E^z_m + \sum_{k=0}^{z-1}(E^k_\infty - \Delta E^k_\infty)\right] + \ln\left(\frac{hcN^0}{Q^0(T)}\right). \tag{2.120}$$

This equation can describe temperature for a level sequence. Its solution is described as follows.

Eq. 2.120 can be written in a linear form as

$$\ln\left(\frac{I^z_{mn}\lambda_{mn}}{A^z_{mn}g^z_m}\right)^* = -\frac{1}{k_B T}{E^z_m}^* + \ln\left(\frac{hcN^0}{Q^0(T)}\right), \tag{2.121}$$

where,

$$\ln\left(\frac{I^z_{mn}\lambda_{mn}}{A^z_{mn}g^z_m}\right)^* = \ln\left(\frac{I^z_{mn}\lambda_{mn}}{A^z_{mn}g^z_m}\right) - B^z(T, N_e), \tag{2.122}$$

with a correction

$$B^z(T, N_e) = z\ln\left[2\left(\frac{m_e k_B}{2\pi\hbar^2}\right)^{\frac{3}{2}}\frac{T^{\frac{3}{2}}}{N_e}\right]. \tag{2.123}$$

Also, with an energy correction as

$${E^z_m}^* = E^z_m + \sum_{k=0}^{z-1}(E^k_\infty - \Delta E^k_\infty). \tag{2.124}$$

Thus, Eq. 2.121 can be solved by considering it as a linear equation. This is, supposing that its left side is a dependent variable and E^z_m the independent one. With this procedure, the temperature can be calculated from the slope -$\frac{1}{k_B T}$. This procedure is known as the Saha-

Boltzmann plot method [68, 69]. However, the other factors depending on T leads to numerical methods as the only ways to solve it. Also, an interesting fact about this method, is that as it supposes that the plasma follows LTE, the linear regression will be representative of that. This is, the better the fit, the nearer LTE is the plasma.

In this chapter, the laser-induced plasma was studied. The most important parameters to classify a plasma were presented, along with a spectroscopical description of its radiation. Also, the ablation process and the expansion of the plasma were presented. Furthermore, a description of the LTE model was provided, with the methodologies for the computation of temperature and electron density. Stark broadening was introduced as the method for electron density determination, while the Saha-Boltzmann equation, derived in this chapter, is the source for temperature calculations. With this, the fundamental information regarding the plasma and its spectral emission is covered. The next chapter presents the experimental methodology that was used for this work.

Chapter 3

Experimental methods

The main goal of this work is to obtain a physical characterization of the LIBS plasma the LIBS plasma under the influence of two re-excitation techniques: heating the sample and the application of a high-voltage discharge to the plasma, with spatial and temporal resolution. In this chapter, the experimental procedures conducted top reach this objective are presented. First, the materials used are described. The general experimental scheme to obtain the plasma is presented. Also, the experimental design of the sample heating, and the application of the discharge are presented. Those constitute the nucleus of the experimental work. Its description include the target description, and the principal characteristics of the apparatus. Most typical spatial resolution studies focus on the description of the vertical axis of the plasma. In this work, both the vertical and horizontal axes of the plasma emission are studied. This required two specific configurations for the radiation collection and detection, one for each direction. Both experimental configurations and the reasons to implement them are explained in this chapter. In order to obtain a general picture of the plasma morphology and its temporal evolution, fast photography was implemented. It is explained the experimental scheme and the materials used for this. Finally, the specific procedures and experimental details are described. With this, it is explained the general picture of the temporally and spatially resolution. Also, it is given a brief description of the procedures to achieve the physical characterization of the plasma. The details and the results obtained are presented in the next chapter.

3.1 Materials

As exposed earlier, this work focuses in the study of LIBS plasma under two different re-excitation techniques. Thus, four LIBS configurations were studied: LIBS alone, LIBS assisted with high-voltage discharge, LIBS on a heated sample and the simultaneous use of the high-voltage discharge with the sample heated. As earlier mentioned, this work focusses on the physics behind the results reported by Amador-Mejía et al. [9]. Therefore samples, instrumentation and experimental

conditions are the same. In this section, the materials and experimental schemes used to produce the plasma in these configurations are presented. In addition, the scheme used to perform the temporal and spatial resolution spectroscopy is described. Finally, the instrumentation required to conduct the fast photography analysis is exposed.

Fig. 3.1 shows the plasma generation and re-excitation scheme used. The instrumentation employed in the different experimental setups are described in the following paragraphs. The

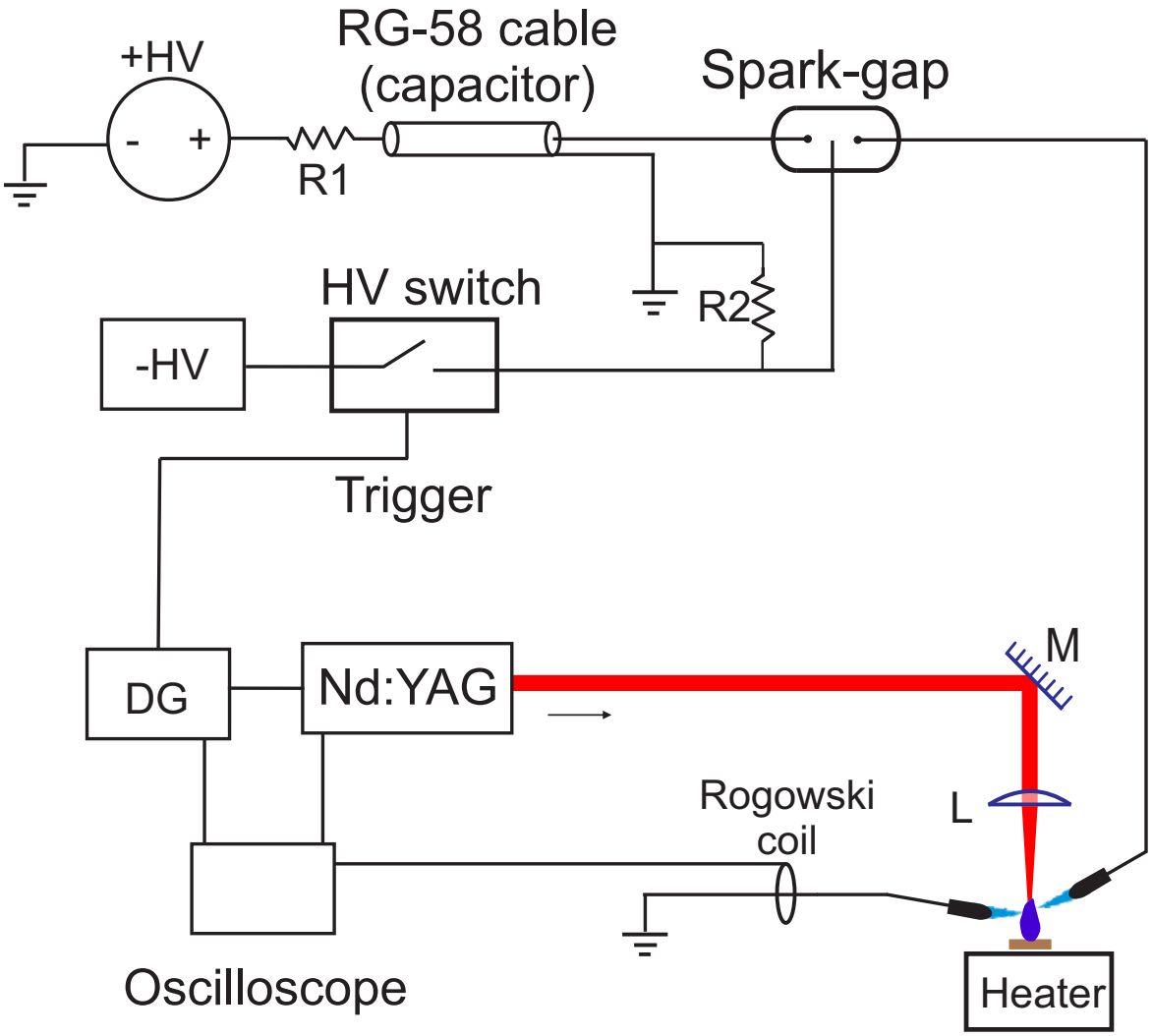

Fig. 3.1: High voltage and heating scheme. Keys: L, lens; DG, delay generator; M, Mirror; R1, 10 MΩ resistor; R2, 1 MΩ resistor.

sample was placed over the heating device, which consisted of a steel plate placed over a ceramic container. As mentioned in Sect. 1.2, the specific application of this work is soil analysis. Then, the samples used were soil pellets. Soils can be characterized by four components: organic matter, inorganic matter, liquid components and gaseous components [70]. This complex composition leads the soils to have heterogeneous surfaces which may lead to matrix effects due to these inhomgeneities. Hence, certified loam samples were used to asses changes of quantification of the four LIBS configurations used in this work.

Certified loam soils, manufactured by High-Purity Standards LLC, were used. Loam soils are made up to 50% of sand, silt and clay, this kind of soil is widely used in agricultural applications [71]. To guarantee the composition and a high level of homogeneity, the soil is collected from the field by the provider in the US. The product is then transported to a laboratory, where it undergoes a drying and mixing process. During the drying period all foreign objects were removed by hand, and sieving process was performed. After these procedures were repeated several times, the manufacturer performed homogeneity and concentration tests using inductively coupled plasma optical emission spectroscopy (ICP-OES) and inductively coupled plasma mass spectrometry (ICP-MS). With this procedure, the manufacturer can guarantee the composition[1] shown in Table 3.1. This composition is certified with a 95% confidence level.

Table 3.1: Composition of the loam soil sample used.

Element	Concentration (mg/g)
Al	57.7 ± 1.8
Ca	4.99 ± 0.13
Fe	45.0 ± 0.6
K	14.6 ± 0.3
Mg	4.44 ± 0.04
Mn	3.35 ± 0.07
Na	3.16 ± 0.10
P	1.64 ± 0.18
Ti	5.78 ± 0.28
Cr	0.269 ± 0.01
Pb	0.129 ± 0.006
V	0.127 ± 0.005

The provider distributes the soil packaged in amber glass bottles. Targets, such as the one shown in Fig. 3.2, are made from this soil after making pellets out of it. This procedure is described in Sec. 3.2.1. As the Table 3.1 shows, most of the elements in the sample have similar concentrations. As the analysis conducted is spectroscopic, it is needed to select spectral ranges based in this table to ensure a sufficient amount of information. The spectral range used is discussed in Sec. 3.2.7.

A Nd:YAG laser is focused onto the sample surface to produce the LIP. The laser used was a Surelite III, manufactured by Continuum, shown in Fig. 3.3. This laser has a pulse width ranging from 4 to 6 ns, a beam diameter of 9.5 mm and a divergence of 0.5 mrad [72]. It was operated at the fundamental wavelength, 1064 nm, with a repetition rate of 10 Hz and 50 mJ of energy per pulse.

[1]The manufacturer does not report the concentration of the major element, Si. Its concentration is estimated at around 30%.

Fig. 3.2: Loam soil pellet used as sample.

Fig. 3.3: Laser Nd:YAG @ 1064 nm, Surelite III from Continuumm [72].

The laser was focused via a 10 cm focal length plano-convex lens (L), as shown in Fig. 3.1, of 10 cm as focal length. This lens, model KPX094, is made of N-BK7 and manufactured by Newport. In addition, the laser was operated in external mode. It was synchronized with a delay generator, model 575 from Berkeley Nucleonics, shown in Fig. 3.4. This generator has eight channels and 250 ps in resolution. Also, it allows for pulse width from 10 ns up to 1,000 s [73].

Fig. 3.4: Delay generator model 575 of Berkeley Nucleonics used [73].

Fig. 3.5: Halogen lamp used to heat the sample.

As mentioned above, the sample was placed over the heater. The implemented heating system consisted of a steel plate placed over a ceramic container. Thus, the sample was placed on the plate, which was heated by a 500 W halogen lamp, shown in Fig. 3.5. The temperature of the plate was monitored by means of a thermocouple. In the experiments that required heating, the temperature was maintained at 400 $\pm$ 20 °C. The halogen lamp was powered with 4 A and 120 V, regulated by a variac.

Fig. 3.1 shows the implemented high voltage system. The sample and the laser path were placed between two brass alloy electrodes. These electrodes, shown in Fig. 3.6, are made of commercial brass alloy; mainly consisting of Cu ($\sim$ 63%), Zn ($\sim$ 33%), and Pb ($\sim$ 3.7%). To know this information is important because it was observed that when using the discharge, the electrodes erode and their elements contaminate the plasma. As the figure shows, the electrodes are hemispherical-capped rods of 6 mm in diameter. They were placed to obtain the V-shaped configuration for the discharge tube. They were placed about 5 mm apart, approximately 2

mm above the sample. However, the different conditions (e.g., the surrounding air temperature) required minor adjustments to these distances in some shots.

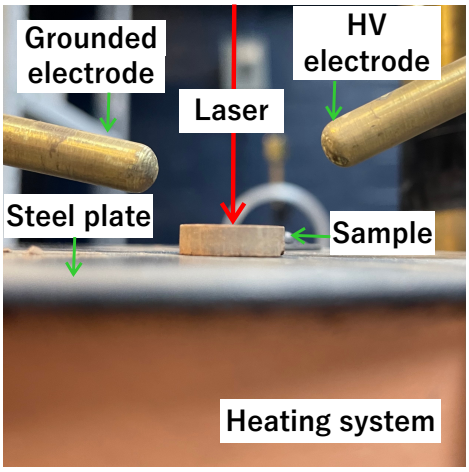

Fig. 3.6: Heating system and electrodes. The left one is grounded and the right one corresponds to the HV.

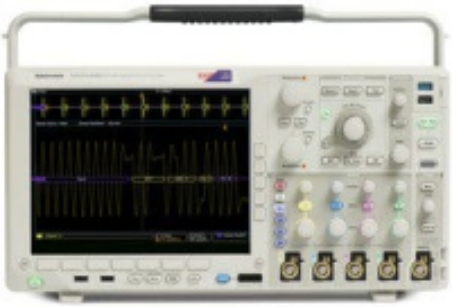

Fig. 3.7: Digital oscilloscope DPO 4104B from Tektronix [74].

A Rogowski coil was used to monitor the discharge by means of a digital oscilloscope shown in Fig. 3.7. The model employed was the DPO 4104B manufactured by Tektronix. This model has a bandwidth of 1 GHz and four channels [74]. One of the electrodes, left side in Fig. 3.6, was grounded and its connection rod passed through a Rogowski coil. From this point on, this electrode is referred as the grounded electrode and the other electrode as the charged one. As illustrated in Fig. 3.1, the delay generator also serves as a trigger for an HV switch. The specific HV switch employed was a Behlke HTS-650 model. Operating within a voltage range of 0 to ± 65 kV with DC, it boasts a maximum peak current of 30 A at DC. This device played the role of triggering a spark gap, a configuration adept at applying substantial current pulses. In fact, it has been capable of deliver pulses with a low rise time ($\sim$ 20 ns) and a low jitter (30 ns). The discharge is produced from a charged capacitor. In these experiments, a 50 m long RG-58 (RG, Radio Guide) coaxial cable with 5 nF total capacitance was used as a capacitor. Once charged, its discharge provides a bipolar pulse shape. The capacitor was charged through a 10 MΩ resistor by a high-voltage supply. It was used a Bertan 205B model manufactured by Spellman (Fig. 3.8), supply with a range of 1 to 50 kV, delivering powers from 15 to 30 W, and the polarity can be reversed [75]. The HV switch was operated by another HV supply model SLM70P600, manufactured by Spellman (Fig. 3.9). This model has positive polarity, 600 W power and can provide 70 kV, 8.56 mA [76].

Fig. 3.8: Bertan 205B HV supply used [75].

Fig. 3.9: SLM70P600 HV supply used [76].

With the implemented HV system, the discharge can be precisely triggered at a programmed time by the delay generator. This action completes the circuit, as illustrated in Fig. 3.1. To characterize the discharge, a high-voltage probe (Tektronix model P6015A) was utilized in conjunction with an oscilloscope. The probe boasts an input impedance of 100 MΩ, a bandwidth of 75 MHz, and a maximum voltage capacity of 20 kV.

With the aim of study the changes in plasma morphology, fast photography was implemented. This was used as a method to study the temporal evolution of the plasma during the LIBS experiments and to compare it to the plasma with the re-excitation techniques. Fig. 3.10 shows the experimental scheme implemented for fast photography.

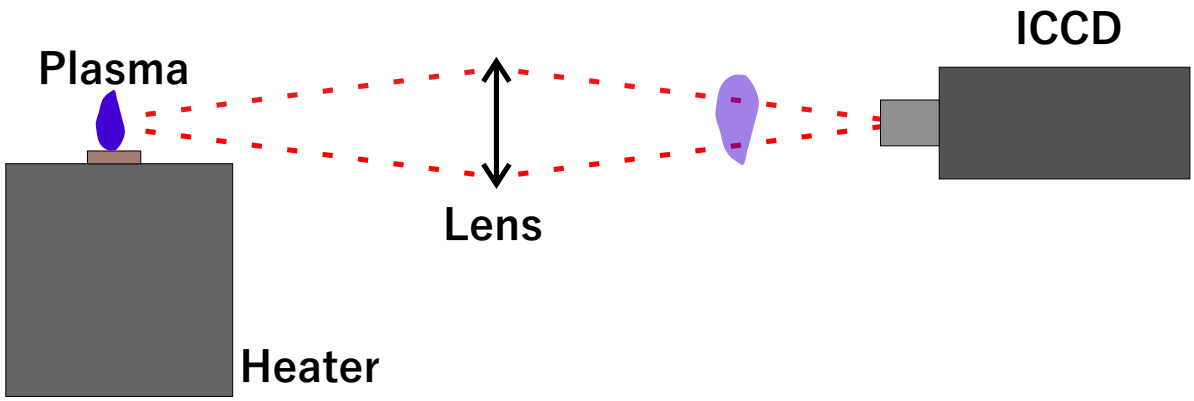

Fig. 3.10: Fast photography experimental scheme. In this case, the plasma is focused directly onto the camera and the image is formed via its lens. Electrodes have been omitted for the sake of clarity.

As shown in the figure, the camera directly captured the plasma image. A 10 cm focal length lens was employed to collect the light, utilizing the camera lens to form an image. This magnification scheme directly reproduces the plasma image on the camera. This configuration was used to obtain photographic images of the plasma at various time delays for each experiment. Further details about the ICCD camera are provided in the following paragraphs.

To investigate how the re-excitation techniques affects plasma physical parameters (temperature and electron density) with spatial and temporal resolution, two configurations were implemented: One focusing on the axial direction of the plasma and another on the radial direction. Fig. 3.11 shows the experimental scheme used to study the plasma parameters with spatial and temporal resolution.

As in Fig. 3.11a), the axial resolution was performed by means of optics, a spectrograph and a detector. The optical path consisted of a BK7 lens (KPX199) of two inches in diameter and 20 cm in focal length. As depicted in Fig. 3.11a), this lens was used in a 2f configuration to reproduce 1:1 the plasma image 40 cm away from it. At that distance, an Acton SP-2500 spectrograph was placed. This is a Czerny-Turner spectrograph manufactured by Princeton Instruments. The internal structure of this spectrograph is shown in Fig. 3.12. A diffraction grating with a electron density of 1,800 lines per millimetre was used and the entrance slit was set at an open width of 50 µm.

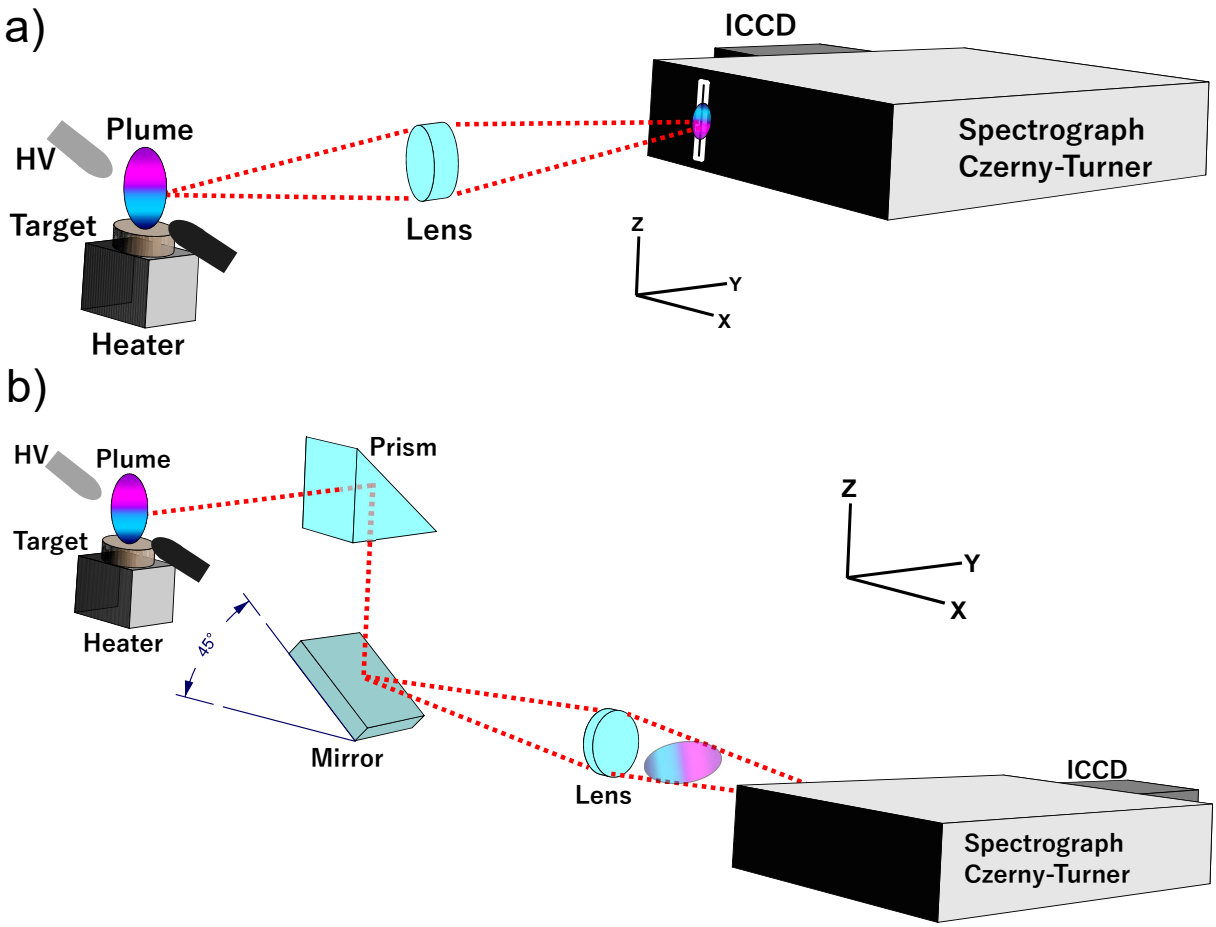

Fig. 3.11: Experimental scheme of the spatially resolved study. a) Axial configuration b) Radial configuration. In black, the grounded electrode, in gray the charged one.

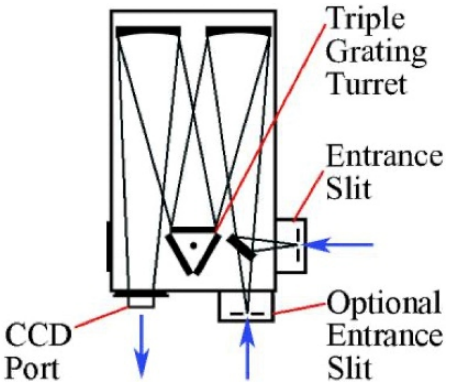

Fig. 3.12: Spectrograph Acton SP-2500 from Princeton Instruments [77].

Fig. 3.13: ICCD detector PIMAX from Princeton Instruments [78].

Therefore, the lens reproduces the image of the plasma onto the entrance slit of the spectrograph. Once the plasma image is centred, this configuration enables the collection of its radiation (and thus its spectra) along the vertical axis of the plasma, with spatial resolution. The detection system consisted of a detector coupled to the CCD port of the spectrograph. It

was used a ICCD camera as detector. The model employed was the ICCD PIMAX manufactured by Princeton Instruments, and shown in Fig. 3.13. The resolution of this model consists of a 1024 x 1024 image array.

The procedure described above allows for the recollection of radiation in the direction parallel to the aperture slit, which is vertical. In order to perform a study on the radial (i.e., horizontal) direction of the plasma, it was necessary to perform a rotation of the optical plane of emission. To do so, the configuration depicted in Fig. 3.11b) was used. The optical path consisted of a quartz prism, placed 10 cm away from the plasma. Then, a mirror reflects the image onto a quartz lens (SPX025) of two inches in diameter and 15 cm as focal length. When the image passes through the prism, its radial axis is reflected to the mirror, but the path length to the mirror changes along this radial axis. This causes the image to rotate. Therefore, the lens reproduces a rotated image of the plasma onto the aperture slit. Then, as the radial direction of the plasma is now parallel to the slit, this configuration allows for the radial collection of radiation. These two configurations were used to study the plasma spectra in both directions: radial and axial. To incorporate the temporal resolution, spectra were acquired at different time delays. As mentioned previously, in this work, the time delay (t_d) refers to the time between the laser output and the start of the ICCD acquisition. Also, the time window of acquisition is called gate width (t_w). These two parameters and thus the ICCD operation were controlled by the delay generator.

As said, synchronisation between the laser pulse, camera trigger, and discharge delay was performed by the delay generator and monitored using the oscilloscope. In the next section, the specific procedures for each experiment are described.

3.2 Methods

In this section, the experimental methodology is presented. The first aspect to be addressed is the sample preparation, from the loam soil powder to turning it into pellets, followed by details of the heating and the application of the high-voltage discharge. The main objective of this work is to investigate how plasma parameters change with spatial and temporal resolution. To achieve this, the electron density and temperature of the plasma were obtained along both the vertical and radial axis. In this section, the procedures for obtaining these measurements for the four LIBS experiments performed are be described. In addition, the application of fast photography, utilized to study plasma morphology, is also described. All these experiments were carried out with the same ambient conditions: 30 ± 5 % of humidity and 22 ± 3 °C. From now on, this temperature will be referred to as *room temperature*.

3.2.1 Sample preparation

As described in Section 3.1, the soil powder requires a pelletizing procedure. For this procedure, 1 g of the sample was placed in a cylindrical container and a pressure of 3,000 lbf/in^2 was applied for two minutes using a hydraulic press. This process produced disk-shaped pellets, as Fig. 3.2 shows, weighing approximately 1 g, with a diameter of 1.3 cm and a thickness of 4 mm.

3.2.2 Sample heating

As described earlier, a heating device was implemented to heat the samples. This device was regulated by a variac. Ten minutes, in average, was the time required to the steel plate reach the temperature specified (400 °C). The lamp was kept at the same voltage throughout all heating experiments and it was never used for more than six hours straight. As should be expected, during these experiments the air surrounding the plate was heated. Also, as the steel plate dilates, it was necessary to adjust the distance between the sample and the laser lens to maintain the same irradiance as in all the other experiments. This was performed by placing the heating device in an xyz translation stage.

3.2.3 High-voltage discharge

When employing high-voltage discharge, an additional parameter was required: the delay between the laser pulse and the discharge output. In this work, the discharge delay (τ) was set at 1.5 µs. Previous studies [9] have demonstrated that this re-excitation delay provides the energy required to enhance the sensitivity of LIBS in loam soils. The system described in the last section was designed to provide a reliable discharge delay, which was also monitored with the oscilloscope. The discharge lasts for about 8 µs. As mentioned earlier, the current was monitored using a Rogowski coil, which measures the current derivative. To characterize the current flowing through the system and, consequently, the energy given to the plasma, numerical integration was performed.

3.2.4 Fast photography

Using the experimental scheme presented in Fig. 3.10, fast photography experiments were conducted to capture the temporal evolution of the plasma. As the plasma was reproduced onto the camera lens, it was captured in a time sequence of photos.Gate delays and gate widths, programmed for the camera with the delay generator, are provided in Table 3.2. Gate delay (also called time delay) is measured from the laser onset. For each of the delays presented in Table 3.2, ten photos were acquired. In the LIBS and LIBS with sample heating experiments the entire series was recorded. However, for the HV configuration experiments the first photo was acquired at a gate delay of 1.5 µs to coincide with the discharge delay. In addition, three delays were added with respect to the temporally resolved delays: 50, 70 and 100 µs.

3.2.5 Temporally and spatially resolved measurements

As depicted in 3.11, a lens was placed at a distance of two times its focal length from the plasma, to reproduce the plasma image over the spectrograph aperture slit. This configuration enables a 1-to-1 image reproduction, ensuring the preservation of not only the plasma shape but also the precise measurements and distances within its images. Spatially resolved spectra were obtained using the following procedures.

Table 3.2: Camera parameters for investigating the temporal evolution of the plasma using fast photography.

Gate delay (µs)	Gate width (µs)
0.5	0.1
1	0.1
1.5	0.1
2	0.2
3	0.3
4	0.4
5	0.5
7	0.7
10	1
30	3
50	5
70	7
100	10

First, the axial resolution was acquired. To ensure that light recollected is from the plasma central axis, the slit aperture was positioned on the central axis of the plasma image. This configuration allowed the spectrograph to obtain spectra along the vertical axis. In the case of the radial measurements, the spectra obtained were along the horizontal direction of the plasma.

Using these configurations, the spatial resolution was achieved. For the time-resolved analysis, the time delay was modified. The gate delays used are shown in Table 3.3. These delays provide information about the plasma near the end of the continuum radiation up to the start of the molecular band emission. For each delay, three measurements were performed, with each measurement consisting of 40 averaged acquisitions. As said in previous section, high-voltage experiments were initialized at $\tau = 1.5$ µs. Additionally, to ensure comparability between measurements, each one was performed at a different spot on the sample surface. The movement of the sample between each measurement was performed with the xyz translation stage. In the case of the heating experiments, these were only performed in the axial direction of the plasma. This is due to the radial symmetry of the LIBS plasma.

Spatially resolved spectra enable measurements of the temperature and plasma electron density along both the vertical and radial axes of the plasma. Also, these delays allow for the time resolved study of each LIBS experiment.

3.2.6 Plasma characterization

To achieve the plasma physical characterization, within each delay, multiple spectra were summed along each direction to increase the signal-to-noise ratio. As mentioned previously, the detector provides an array of 1024 × 1024 pixels. Thus, each spectra consists of a 1024 × 1024 matrix. It was developed a mapping to convert between pixels to *real* distances. With this, it was determined that a width of 0.2 mm was sufficient to provide processable spectra. i.e., with low

Table 3.3: Camera parameters for investigating the plasma physical parameters with spatiotemporal resolution.

Gate delay (µs)	Gate width (µs)
0.5	0.1
1	0.1
1.5	0.1
2	0.2
3	0.3
4	0.4
5	0.5
7	0.7
10	1
30	3

noise. Then, a total length of 0.2 mm was covered in each summation, with a spacing of 0.1 mm between the summed spectra. Therefore, radiation was collected and processed in rectangles of 0.05 × 0.2 mm, defined by the aperture slit and the spatial summation. Fig. 3.14 shows these measurement points, which constitute the spatial resolution. As the figure shows, the measurement range was determined by eyesight, based on the SNR. Then, the far from the centre is, the less is the radiation intensity. Then, the radial measurements were performed at the maximum vertical intensity of the plasma: approximately 1.6 mm above the target. On the other hand, axial measurements were performed at the maximum radial intensity.

The resulting spectra were processed numerically. The electron density was obtained from the Stark broadening of the emission lines, as described in Sect. 2.3.4. The temperature was calculated by means of the Saha-Boltzmann plot method, according to Sect. 2.3.6.1. The transitions used are discussed in next section.

3.2.7 Spectral selection

In the configuration used, the spectrograph is capable of collecting a range of approximately 12 nm, then it is necessary to define an spectral range for the analysis. A proper range must have both neutral and ionic transitions of the same element, which is needed to perform a Saha-Boltzmann analysis and calculate the plasma temperature. Such a range can be obtained when the spectrograph is centred at 282 nm, which comprises all appropriate transitions for the Saha-Boltzmann analysis

Fig. 3.15. shows a spectral simulation of this range. It was made using the NIST LIBS atomic database [79], considering the concentrations of Table 3.1 and the suspected percentages of silicon (20%) and oxygen (66%). It was also made with a typical LIBS plasma temperature (1 eV) and electron density ($10^{-17}\, cm^{-3}$).

As the figure shows, in this range magnesium has four ionic transitions and one neutral transition. Actually, there are five more neutral transitions in the zone around 278 nm. However,

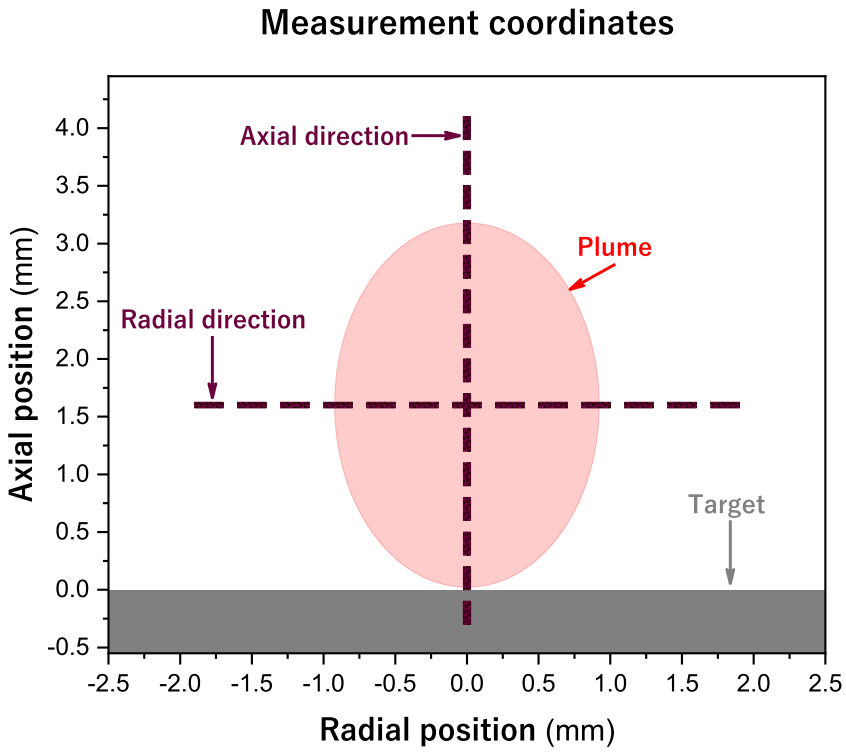

Fig. 3.14: Spatial resolution. Purple squares illustrate the spatial regions that were analyzed in both the axial and radial directions. The red ellipse is an approximation to the region where a high SNR was observed. It corresponds, approximately, to the pixels with at least 13.5% of the maximum intensity. The zero in the y-axis corresponds to the target surface. Zero in the x-axis corresponds to the maximum radial intensity of the radiation.

these transitions have a low SNR and are inconsistent over time. In addition, they are coupled with ionic iron lines, making them unreliable. Thus, only the transition 285.2127 nm of Mg I was used. This line was also used to compute the electron density.

Regarding ionic lines, the transitions 279.0776, 279.5528, 279.7998, and 280.2704 nm of Mg II were selected[2]. With these Mg transitions, the Saha-Boltzmann method was performed. Although these lines are well resolved, their intensity decreases over time, as has been discussed for ionic transitions. Also, in this range there are three Mn I transitions in the zone of 279 to 280 nm. These transitions increase their intensity over time. This makes it difficult to analyse temperature at longer delays. As shown in Fig. 3.15, two more transitions were considered. First, the 275.5736 nm transition of Fe II. Although the figure shows the presence of a Fe I transition, which in fact is in 278.81 nm, this line has a low SNR and is only visible at longer delays. However, the Fe II transition is used in Sect. 4.7 to analyze the distribution of ionic species. This is also the case for the 288.1579 nm transition of Si I. This is a transition from the major element; thus, its intensity is unreliable, due to autoabsorption. However, analogous to the Fe II transition, it was useful to study the distribution of neutral species.

[2]These are the values reported by the NIST. In the acquired spectra the exact positions usually differ, mainly due to Stark shift. Also, in this work, the measured values were used with a precision of up to the second decimal place, due to the limited resolution

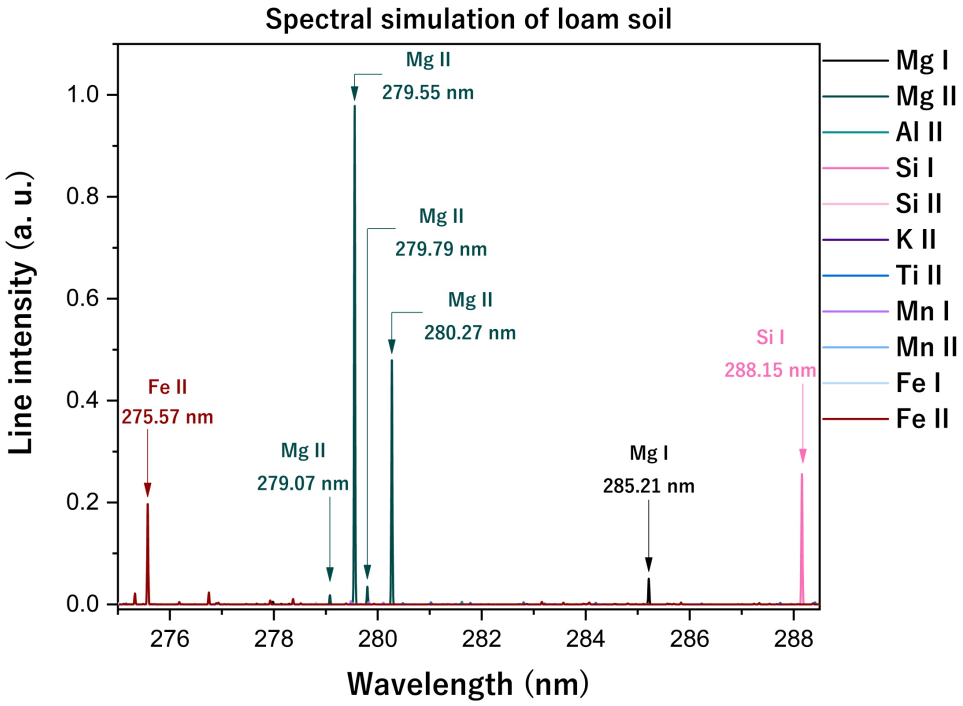

Fig. 3.15: Spectral simulation of the loam soil matrix in the range from 275 to 288.5 nm. Elemental concentration corresponds to Table 3.1, with approximately 20% of Si and 66% of O. The temperature and the density used were 1 eV (11,604.518 K) and $10^{-17}\,cm^{-3}$, respectively. Intensity is expressed in arbitrary units.

The procedures and instrumentation described in this chapter constitute the main experimental work carried out to achieve the objectives of this work. The subsequent chapter presents and discusses the obtained results.

Chapter 4

Results and discussion

This chapter presents and discusses the results obtained from the experimental methods outlined in the previous chapter. The initial sections detail the laser focusing process and characterise the discharge in terms of current and voltage. Additionally, the delivery of energy and power to the plasma over time is examined. An illustrative example of spectra is then presented to offer an intuitive understanding of the plasma emission structure. From these spectra, an example of the signal-to-noise-ratio is also provided as a general motivation for this work. These examples are followed by a detailed description of the morphological structure of the plasma, mainly via the results of fast photography. The chapter addresses electron density and temperature, presenting the results obtained from Stark broadening and the Saha-Boltzmann technique, respectively. These results are explored across the different spatial positions, times, and the four experimental conditions. This is, samples with varying temperatures and laser-induced plasma (LIP) with and without an applied high-voltage (HV) discharge.

Sect. 4.1 addresses the spectral impact of the discharge on species and their positions. Finally, all the results obtained for electron density and temperature are used to evaluate the plasma parameters detailed in Sect. 2.1.1. The assumptions made about the plasma are also examined in this analysis, investigating the existence of local thermodynamic equilibrium (LTE) conditions through the evaluation of the three criteria described in Sect. 2.3.5. Throughout all these results, insights and discussions about the findings are provided. The figures presented were elaborated via OriginLab.

4.1 Laser ablation

In this section, the laser-induced breakdown is addressed. As described in the last chapter, the laser was focused on a soil sample. Therefore, in the following paragraphs, the irradiance at target's surface is calculated.

It should be noted that breakdown can occur in the air. This happens if the irradiance in the surrounding air reaches its breakdown threshold. On the other hand, in the past chapter was described that each measurement consists of an average of shots. Then, as each shot removes matter, consecutive shots may star ionising the surrounding air. To avoid these two effects, it is

usual to focus the laser below the target surface. Fig. 4.1 shows the lens design and how the focal point is at a distance d from the target's surface.

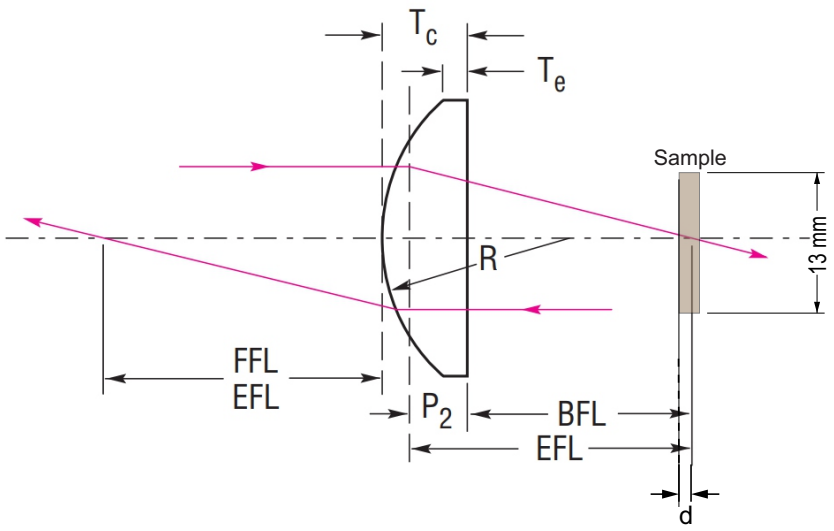

Fig. 4.1: N-BK7 lens used to focus the laser radiation onto the sample. Keys: $EFL = 100$ mm, effective focal length; $BFL = 96.97$ mm, back focal length; $R = 51.68$ mm, radius of curvature; $T_c = 4.585$ nm, centre thickness; $T_e = 3$ mm, edge thickness; $P_2 = -3.02$ mm, principal plane 2; d, distance from the lens focus to the sample surface. Design wavelength: 589 nm [80].

In this scheme, EFL corresponds to the focal length. As the figure shows, d may be on the order of the thickness of the sample. This parameter was adjusted at sight, using the plasma intensity as a control variable.

The first consideration arises from the lens material. The focal length $f = 10$ cm reported in the last chapter was obtained by the manufacturer with a design wavelength of 589 nm. At this wavelength, the N-BK7 has a refractive index $n = 1.5167$, and at the laser's wavelength, 1064 nm, $n = 1.5066$ [81]. Thus, from the lens maker's expression,

$$\frac{1}{f} = (n-1)\frac{1}{R}, \tag{4.1}$$

where $R = 51.68$ mm is the curvature radius, it follows that $f = 10.201$ cm.

Then, it is clear that BFL= 98.99 mm. On the other hand, the distance from the plane side of the lens to the surface of the sample is about 95 mm. Thus, $d \sim 3.99$ mm.

Supposing that the surface is far from Rayleigh's distance, from Eq. 1.11 and using D = 9.5 mm as the beam diameter, it results that $w_0 = 0.00727$ mm is the beam waist at the focus. Thus, from Eq. 1.7, the radius of the incidence spot is about ~ 0.1858 mm. With an average

width of 5 ns, and 50 mJ of energy, the irradiance at the spot can be estimated as

$$I = 9.22 \times 10^9 \, \frac{W}{cm^{-2}}, \tag{4.2}$$

Therefore, the irradiance at the surface is sufficient to vaporize the target and lead to the breakdown of its vapour. With this irradiance and a nanosecond laser, it should be expected that the pulse lasts longer that the vaporization time. Thus, the laser radiation should interact with the vapour cloud. Then, inverse bremsstrahlung should dominate the first stages of the plasma. After the collision-induced ionization, the electron density should rise exponentially. After the plasma starts expanding, collisional processes should dominate over radiative ones. Thus, the plasma should be in LTE.

4.2 High-voltage discharge

As one of the main objectives in this work is to study LIBS plasma re-excited by means of a high-voltage discharge, it is necessary to characterize the discharge. In particular, the main properties of the discharge are its shape, its current, and the energy that it carries. In this section, these properties are addressed.

In the previous chapter, it was discussed how the HV system works. It is powered by an HV supply and a conventional spark-gap was implemented to increase reliability. Then, the first parameter to be discussed is the trigger.

As said previously, Amador-Mejía et al. [9] demonstrated that this configuration can significantly improve the SNR with a discharge delay (τ) of 1.5 µs. At this delay, most of the ionic emissions decrease significantly. Thus, the objective of applying a discharge at this delay is to intensify the LIP emission. In the rest of this chapter, the mechanisms for doing so are investigated.

The voltage at the exit side of the capacitor was monitored by a high-voltage probe, and the current was obtained from a Rogowski coil. Actually, a Rogowski coil measures variations in the current that is passing through, i.e. its derivative. Thus, it was numerically integrated. The resultant current is shown in Fig. 4.2 along with the voltage. As the figure shows, at τ=1.5 µs, there is a potential difference that drives an alternating current. This potential difference is in the order of the HV supply. The voltage is maintained at low values after the discharge trigger, and stabilizes around zero at about 12 µs.

This bipolar current reaches a maximum of 185 A, in its first period, that lasts approximately 0.6 µs. On average, the time interval between zeros is 0.5 ± 0.11 µs, and fitting an sinusoidal wave, the period is actually about 0.57 µs. The sign of the current is determined by each local maximum or minimum in the voltage plot. Thus, the shape of the current plot is a sinusoidal damped wave, which in the interval between 1.5 and 12 µs has an exponential upper

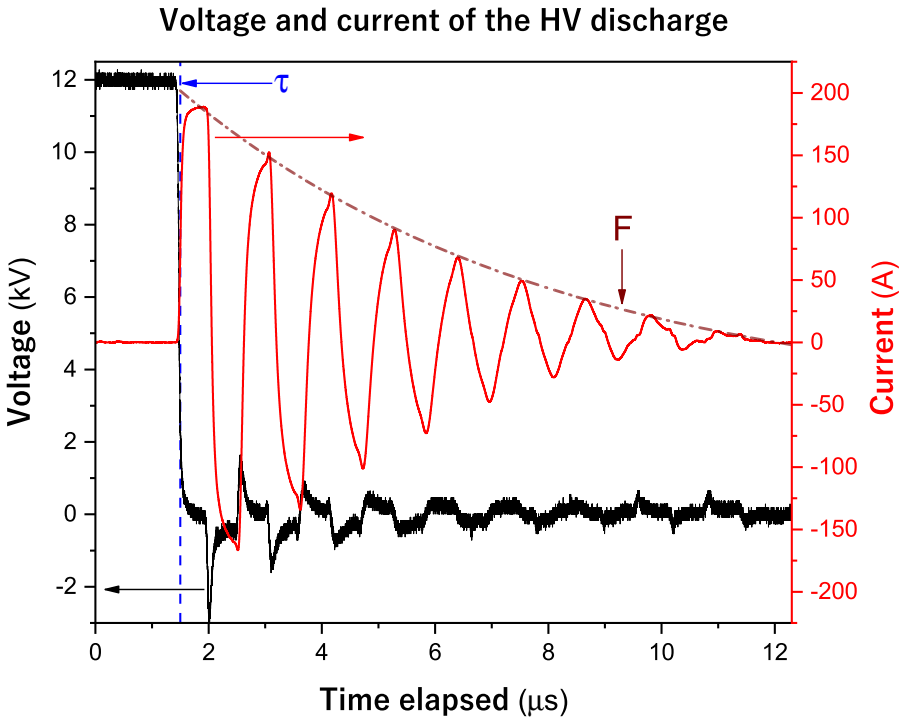

Fig. 4.2: Temporal evolution of the voltage at the exit side of the capacitor and the current at the grounded electrode. The zero in the x-axis corresponds to the laser onset. τ=1.5 µs is the discharge trigger time. F is the upper envelope of the current.

envelope that decreases with time t as

$$F(t) = -51.89 + 247.1 \exp\left(-\frac{t - 1.67}{6.64}\right). \tag{4.3}$$

The current vanishes at about t = 12 µs and reaches half of the maximum within the 5 µs after the laser pulse is triggered.

These plots provide the general information regarding the composite circuit, which should be remembered, is closed by the plasma. Thus, from these plots it is not physically clear what is the effect on the plasma, in terms of the energy delivered by the discharge. To investigate the energy and the rate at which it is delivered to the plasma, power and energy are plotted in Fig. 4.3.

Instead of the power itself, its absolute value was calculated. This, because what is of interest is the net energy that is delivered to the plasma. Although the current is bipolar, the energy delivered to re-excite the plasma should be the net flux of energy flowing through its boundaries at each time, independently of the current direction.

The power plot also resembles a damped wave. Starting from τ, where it reaches it first local maximum. In fact, the global maximum for the power comes at 2 µs, where 330 kW are delivered by the circuit. After the third local maximum (240 kW), at 2.5 µs, the power decreases significantly. Three microseconds after the laser onset, the peak power is about 100 kW. In general, the power follows a gamma distribution, centred around 2 µs and with positive skewness.

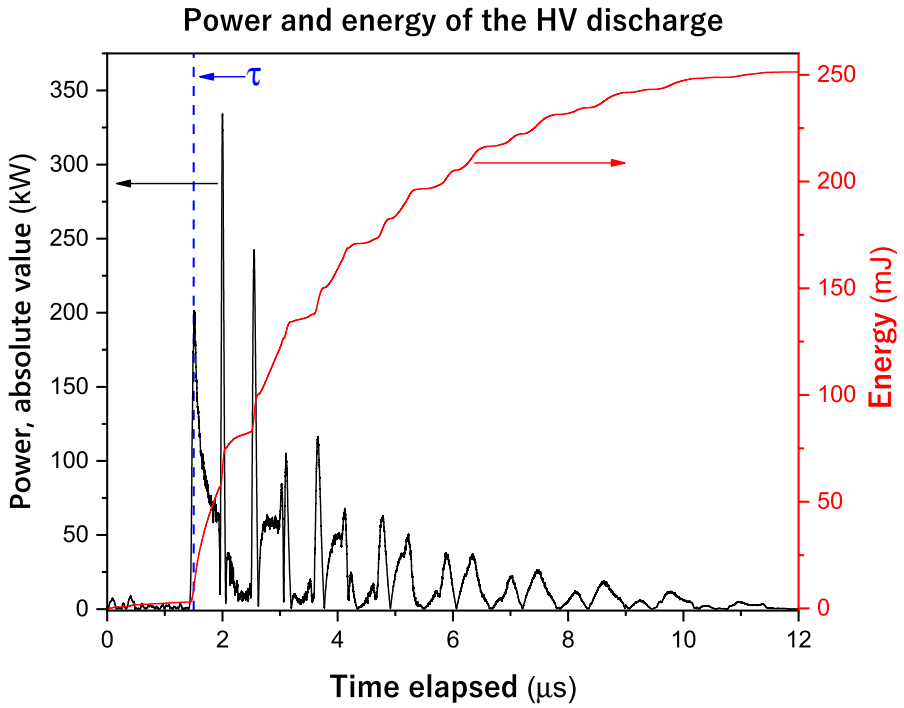

Fig. 4.3: Temporal evolution of the power and energy delivered with the HV discharge. The zero in the x-axis corresponds to the laser onset. τ=1.5 µs is the discharge trigger time.

This arises from the fact that the absolute value of the current has a decreasing exponential as an envelope. Thus, it can be suggested that even if the current lasts longer, during the first 3 µs the energy flux rate is at its maximum.

The current envelope follows a decreasing exponential, $I(t) \sim \exp(-t)$. It is clear that, with an approximately constant voltage, the net energy will increase as a negative exponential, $E(t) \sim -\exp(-t)$. This is also depicted in Fig. 4.3, where the cumulative energy delivered by the HV discharge is presented. It shows that 12 µs after the laser onset, the energy delivered through the plasma boundaries; from the HV system is 251.3 mJ. This is, of course, an estimation made with several assumptions, such as neglecting the impedance of the circuit. Then, it can be assumed that the energy delivered to the plasma is around 250 mJ. For this distribution, the first quartile comes at 2 µs. At 3 µs, half of the total energy was already delivered. The third quartile is at 5.1 µs and at 7.45 µs, ninety percent of the total energy was delivered. In fact, at 10 µs almost 99% of the total energy was already deposited.

Thus, the experimental data about the HV discharge suggests that within the initial microseconds following the discharge trigger, the majority of the discharge energy is deposited into the plasma. Therefore, if there are any discernible effects of the discharge on the plasma, they are anticipated to peak around 2 µs and progressively diminish by 7 µs after the laser onset.

4.3 Spectral analysis

In this section, the spectral data obtained is analyzed. The temporal and spatial evolution of the spectral range previously specified is discussed.

As previously said, it is well-known that the plasma has cylindrical symmetry. Then, only the axial direction is presented. Fig. 4.4 shows how the spectra changes along the axial direction. These spectra were taken at 2 µs after the laser onset. The spectral intensities are normalized, with respect to the position of the maximum, for the sake of clarity.

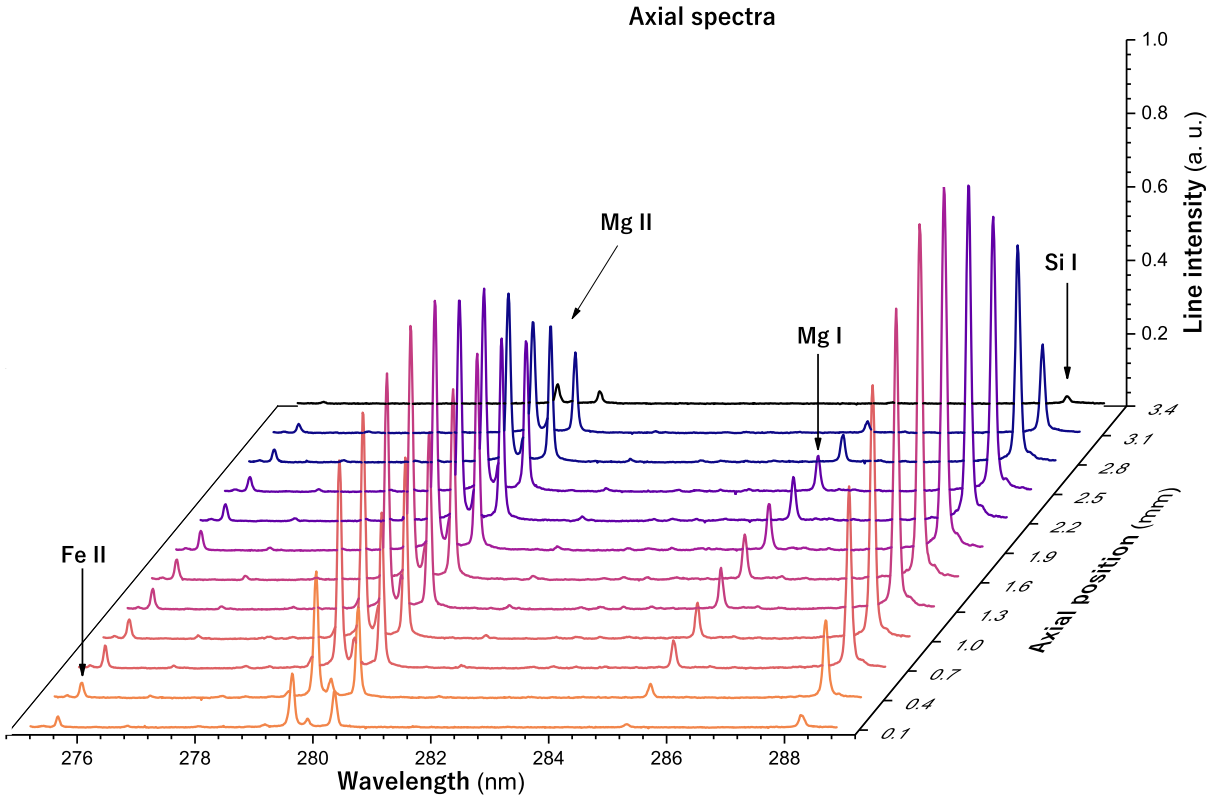

Fig. 4.4: Spatially resolved spectra on the axial direction. Time delay: 2 µs.

It can be seen that the spectral emission has symmetry in the axial dimension. As expected, the spectral intensity reaches its maximum at approximately 1.9 mm above the sample surface[1]. In this case, the Si I transition has the higher intensity at medium positions. This elevated intensity is attributed to the prominence of silicon as a major element. However, at the boundary positions, the Mg II group surpasses Si I in intensity. Then, as the proportions between ionic and neutral lines change at the boundaries, it is reasonable to anticipate variations in plasma parameters along this direction.

[1]The radial axis was centred around the estimated axial maximum, approximately 1.6 mm above the sample surface. Therefore, it can be expected that the actual maximum occurs in proximity to this position.

The temporal behaviour of the spectra can be studied similarly. Fig. 4.5 shows the temporal evolution of the height of Lorentzian fits for the Mg II (280.27 nm) and Mg I (285.21 nm) transitions, at the centre of the plasma. Data are presented for the four experimental conditions that were performed. For this analysis, the three recorded spectra were averaged and their intensity normalised to the number of accumulations in each one. The error bars were obtained from the fitting error.

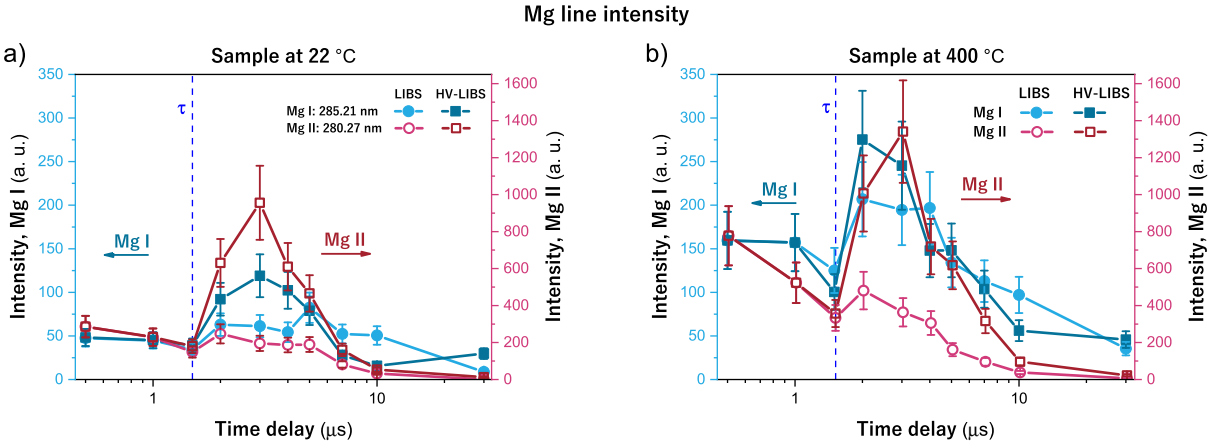

Fig. 4.5: Temporally resolved intensity (line height) of Mg transitions (Mg I: 285.21 nm, Mg II: 280.27 nm) at the plasma centre (i.e., radial position: 0 mm, axial position: 1.6 mm). The dashed line (τ=1.5 µs) corresponds to the discharge trigger. The error bars correspond to the fitting error. a) Sample at room temperature b) Sample heated to 400 °C.

Fig. 4.5a) presents the comparison of line intensity between the LIBS and HV-LIBS experiments performed at room temperature. As the figure shows, the atomic transition slightly increases its intensity around 2 µs and decreases with longer delays. On the contrary, the ionic transition decreases its intensity over time. This trend is a consequence of recombination. When the plasma cools, the ions recombines with the electrons, which leads to the observed behaviour. Thus, the temperature and electron density should follow a trend similar to that of the ionic transition. When the discharge is applied, it significantly enhances the ionic emission at 2 µs. This enhancement is maximum around 3 µs and then it decreases. The atomic transition also increases its emission, although significantly less than the ionic transition. As this behaviour agrees with the observations of the discharge energy (see Fig. 4.3), it can be suggested that this energy supply is responsible for the enhancement of the intensity and the main effect of the discharge occurs between 2 and 5 µs after the laser is fired.

Fig. 4.5b) shows the same experiments, but carried out on a heated sample. As the figure depicts, in a LIBS experiment both atomic and ionic transitions exhibit a continuous enhancement in their intensities at short delays. While at longer delays their behaviour resembles that of the room-temperature case. Then, it can be suggested that, as with discharge, heating the sample has its main effect at short delays. This may be due to the increased removal of matter. As studied by our group in [9], the ablated volume increases up to seven times when the sample is heated to 400 °C. Then, it should be expected that this increase in emitters enhances the total emission of the species. However, it is not clear why this intensity increase is predominant for shorter delays.

When the discharge is applied to the plasma induced in a heated sample, it is observed that both neutral and ionised species increase their emissions. It is clear that, as in the room-temperature case, the ionic line has the largest increase. Then, it should be expected that the combination of both re-excitation techniques lead to a further increase in electron density and temperature.

It can be inferred from Fig. 4.5 that the error bars also increase with the re-excitation techniques. In Fig. 4.5a), both intensity profiles show an increase in their associated errors when the discharge is applied, particularly in the ionic transition. Similarly, in Fig. 4.5b), heating the sample further amplifies the error bars in both transitions. This may suggest that re-excitation techniques contribute to the heightened variability in plasma spectral emission. This leads to a difficulty in measuring how optimal the enhancement in intensity is. This is because a transition can increase its emission, but if the background noise also increases or has high variability, the net enhancement may be negligible. Considering the definition of the signal-to-noise ratio (SNR), which measures the quality of the signal as [82]

$$SNR = \frac{\langle \mu \rangle}{\sqrt{\langle n_s \rangle + \langle n_d \rangle + \langle n_b \rangle}}, \tag{4.4}$$

where $\langle \mu \rangle$ is the mean signal, and $\langle n_s \rangle$, $\langle n_d \rangle$, $\langle n_b \rangle$ the mean signal noise from photons, extra detector counts and background sources, respectively. In this case, the main source of noise is assumed to arise from plasma emission. Thus, the detector and background contributions are neglected[2]. Usually, the mean noise is calculated as the expected value of the noise. However, in this case, as the only emissions should come from transitions, the expected value should be zero. Then, the standard deviation of the signal noise is used instead of its mean. Thus, the SNR is calculated as the ratio between the line intensity and the standard deviation of the signal noise near each transition.

Fig. 4.6 shows the calculated values for SNR, using the height of the transitions and the standard deviation of the noise at their background. In this case, the error bars correspond to the error-propagated quotient of the signal intensity and the standard deviation of the signal noise.

As Fig. 4.6a) shows, the atomic profile of SNR slightly increases with time, and decreases after 10 µs. Also, it is observed that the ionic transition decreases its net emission over time. These results are in agreement with the previous observations, where it was suggested that the recombination enhances the emission from neutral species and decreases ionic emission.

In contrast, the application of the HV discharge leads to different results. First, the ionic emission increases its SNR. Around 3 µs it starts to decrease, which also agrees with the previous observations. However, in the case of the atomic transition, the SNR ranges from almost no change to lesser values than only LIBS. Thus, it can be suggested that the noise increases its variance when the discharge is applied to the plasma. On the other hand, it is known [9] that the discharge increases both electron density and temperature. Thus, it should be expected that as the discharge re-excites the plasma and increases its internal energy, the amount of neutral transitions should not increase.

[2]Although these two contributions are lower than the plasma emission, a background subtraction was performed.

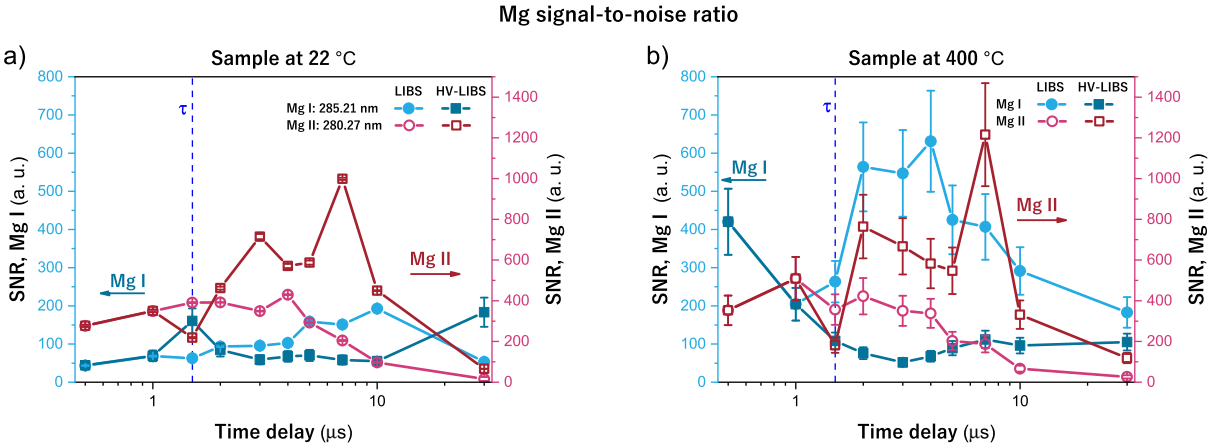

Fig. 4.6: Temporally resolved signal-to-noise ratio of Mg lines (Mg I: 285.21 nm, Mg II: 280.27 nm) at the plasma centre (i.e., radial position: 0 mm, axial position: 1.6 mm). The dashed line (τ=1.5 µs) corresponds to the discharge trigger. The error bars correspond to error-propagated quotient of the intensity and noise. a) Experiments at room temperature b) Sample heated to 400 °C.

Fig. 4.6b) shows the SNR obtained when the sample was kept at 400 °C. In the LIBS case, the atomic SNR increases significantly after 2 µs and the ionic SNR decreases with time. These trends can also be attributed to recombination. However, when the discharge is applied in this case, the SNR has values similar to those at room temperature. This can be attributed to an increase in noise variance, as a result of the noise introduced by both techniques. Also, a similar trend with the atomic transition is observed. Its SNR decreases with time when the discharge is applied, except at 7 µs where it slightly increases. At this delay, there is other interesting effect. At both sample temperatures, the SNR of the ionic transition temporarily increases when the discharge is applied. This could be due to the fact that around this delay the discharge decreases significantly. Thus, it can be suggested that the discharge flow is a strong source of noise because when it is turned off, the noise variance decreases significantly, making the SNR to increase. However, for longer times, as the plasma cools down, the emission from both transitions continue the decreasing trend.

The purpose of this section was to illustrate how is the spectral emission of the plasma and how it evolves with time. Also, to show that the re-excitation techniques increase its emission. These results correspond to the plasma centre. As the centre has the maximum emission, the general picture should be similar. However, this strongly depends on if the plasma -and its parameters- are symmetric along the spatial positions. With the aim of studying the plasma shape and structure, in the next section fast photography is used to study its morphology.

4.4 Plasma morphology

In this section, studies on plasma morphology are presented. First, it is illustrated the temporal evolution of the plasma, for the four conditions studied. Then calculations regarding the size of the plasma are presented, in order to clarify whether the techniques affect the plasma morphology.

In order to investigate how the plasma evolves with time and how changes with both re-excitation techniques, fast photography was implemented. It consisted of an array of photos, taken at the delays listed in Table 3.2. Fig. 4.7 shows some of the most representative delays studied.

As the figure shows, the photos were taken for each delay and for each experimental condition. Although spectroscopic measurements after 10 µs did not yield sufficient intensity for analysis, the camera continued to capture radiation up to 100 µs. In the case of LIBS, it is observed that the plasma shape is preserved along the first 10 µs. In this range, the plasma image has an ellipsoidal shape. In contrast, with longer delays, it can be seen that its height reduces and its width expands. This may be an indication that its internal pressure is no longer capable of balancing the pressure of the atmosphere. At this delay, its total energy should not be high enough to emit appropriately for the analysis. In addition, at 100 µs after the laser onset, the plasma decreases considerably and breaks out. The image shows that it divides into two sections, with the remnants of the laser in between. In fact, at longer delays, this structure should not be referred to as plasma. Those remnants likely correspond to air that remains heated by the laser.

When the heating system is used, the shape of the plasma is modified. It is clear that its width seems larger as the atmosphere temperature increases. As discussed previously (Sect. 2.2.3), the plasma expansion is orthogonal to the target surface. Also, it has been shown that ablation craters increase their diameter when the target is heated [9]. Thus, it is expected that the diameter of the plasma increases as well. Furthermore, at longer delays, the plasma preserves its shape when the sample is heated, unlike in the room-temperature case. Even at 100 µs the plasma slightly changes its shape. This may be due to more ablated matter, which results in more internal energy. Also, if the ambient pressure is decreased as its temperature increases, the internal and external pressure balance is maintained long after than at room temperature.

Heating the sample is known to enhance the material removal, but this effect doesn't appear directly linked to the axial expansion of the plasma. Then, although the surrounding atmosphere changes its temperature, this does not lead to a significant increase in the plasma expansion. However, with these changes in pressure and the increase in removed matter, it should be expected that the plasma increases not only in diameter, but in height. Since there's no apparent reason for the plasma to decrease in height, this phenomenon could be attributed to plate dilatation. As the plate heats, it was observed to expand. Although the plate is raised to maintain the distance between the lens and the sample, it might not be entirely sufficient. Consequently, the laser is focused deeper into the sample than in the room-temperature case.

Fig. 4.7 also shows when a HV discharge is applied to the LIBS plasma. It can be seen that the discharge channel is indeed asymmetric. The charged side interacts with the top side of the plasma, with a discharge channel at approximately 45 degrees. Yet the grounded electrode applies the discharge horizontally.

A few microseconds after the discharge is triggered, the plasma retains its shape. However, its volume increases significantly at 5 µs. In fact, even after the discharge stops around 10 µs, the volume continues to increase. This is a confirmation that the discharge effect continues after the current is gone.

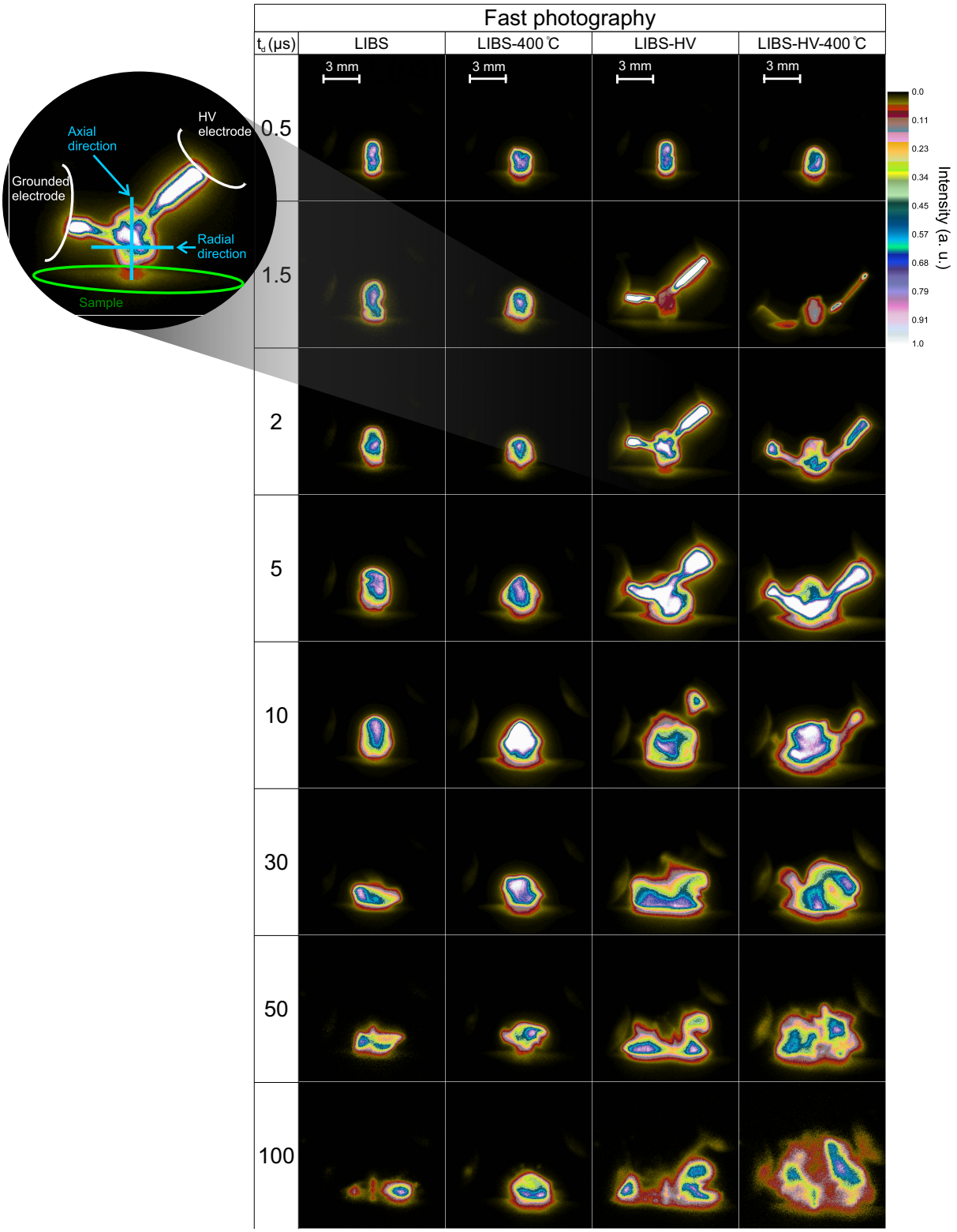

Fig. 4.7: Comparison of the plasma evolution with each experimental condition implemented. Colour is used to distinguish zones by their intensity. The intensity is normalised. Key: t_d, delay from laser onset.

This perturbative effect has further implications. From the figure, it is clear that the plasma begins to expand in its radial direction, approximately at 30 µs. This effect was previously observed in the LIBS plasma at 100 µs. In the HV case, this radial expansion, akin to a shape decomposition, is notably accelerated.

It is then suggested that HV discharge induces a perturbative effect on plasma emission. The discharge turns the plasma turbulent and affects its coupling. Also, it is suggested that the discharge effects are mainly in its radial direction.

When both re-excitation techniques are used simultaneously, their effects are slightly different. First, the discharge channel moves to the target. This change in the application zone is observed throughout all photos. Thus, the atmosphere temperature may influence how the spark breaks the air.

In addition, it has been described how heating the target maintains the pressure balance. However, with discharge, the plasma decomposes even if the atmosphere temperature was raised. It is clear that at longer delays the plasma emission seems more compact than with the discharge alone. Yet, it shows two interesting properties. First, it splits in half. Also, that its vertical expansion is increased. This may be consistent with a local decrease in atmospheric pressure as its temperature increases.

From these photographs several observations were made, mainly about how the plasma dimensions increase with each technique. In order to clarify how both axes evolve with time, Fig. 4.8 is presented. The bright zone corresponds to the plasma or the heated gas shape in Fig. 4.7. For each, the intensity and the axial and radial size were measured, measuring the size up to 13.5% ($1/e^2$) of the maximum intensity. Each value consists of the average of three measurements. The error bars correspond to their standard deviation.

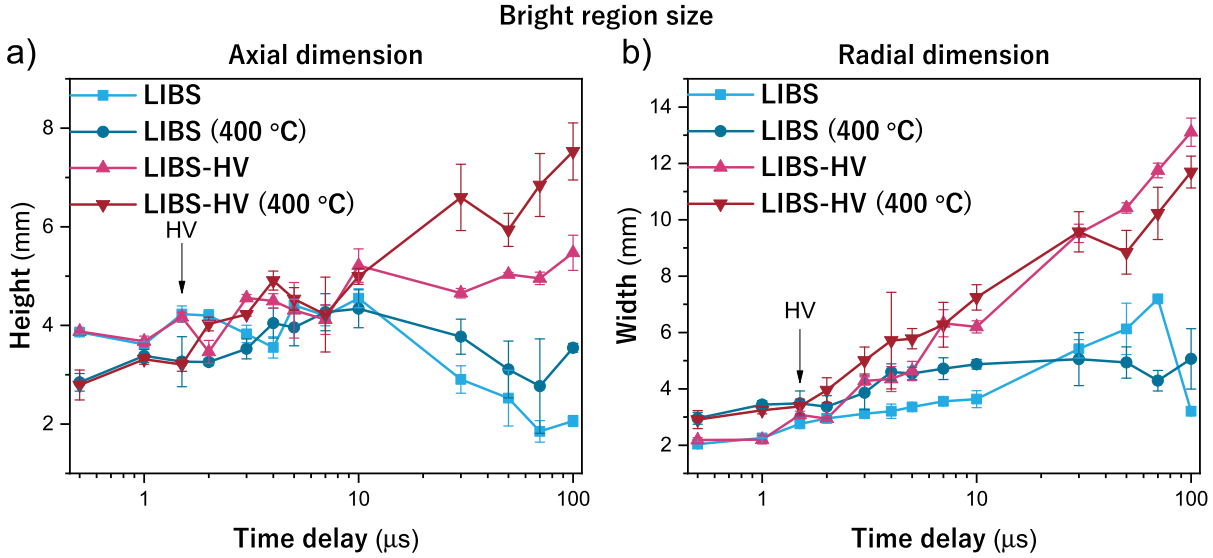

Fig. 4.8: Temporal evolution of the bright zones in fast photographs. Sizes measured at 13.5% of the maximum intensity. The error bars correspond to the standard deviation of three measurements. a) Axial direction b) Radial direction.

Fig. 4.8a) shows how the axial dimension evolves with time, for each re-excitation technique. In the LIBS case, at room temperature, it is clear that the heights of the emitted radiation do not change significantly with time, with short delays. After 10 µs it continuously decreases. In contrast, when the target is heated, this axis is shorter, and it increases slightly with time. Moreover, its rate of decrease is reduced, in contrast to that in the room temperature case. As mentioned earlier, this behaviour is attributed to the focusing of the laser.

On the contrary, it is clear that the application of the HV discharge significantly increases the size observed along the axial direction. This, at longer delays, when the current has already stopped. In short delays, the axial direction has a slightly increased height. When the target temperature is increased, the height increases continuously. This rise in height is increased after the discharge stops. Then, when the temperature is increased, the emission zone axially expands.

Fig. 4.8b) shows the temporal evolution of the radial dimension, with each re-excitation technique. In the case of LIBS emission, the width continuously increases. However, at 100 µs the emission cloud starts to decompose. This effect is lowered when the target is heated. In this case, the width is larger than at room temperature and its increasing rate is almost nullified at longer delays.

When a HV discharge is applied to the plasma, the emission volume significantly increases its width. This increase in width is almost twice the increase in height. There is not a significant difference when the target is heated.

Therefore, the main effect of the heating system is to delay plasma decomposition. Heating the target allows the plasma to maintain a pressure balance with the surrounding air. On the contrary, although the HV discharge adds energy to the plasma, it also contributes to perturb its expansion. After the current stops, the plasma starts to expand significantly in both axial and radial directions. In specific, the discharge affects mainly the radial direction. In this direction, the plasma expands and splits at longer delays. Even if the heating should sustain the plasma, when both techniques are used, the axial expansion is increased. This may be due to a lower atmospheric pressure.

To conclude, in this section the main results from the plasma structure were presented. It was shown that the plasma tends to break apart, which can be slowed down by heating the sample (and the atmosphere). However, the HV discharge induces strong turbulence that lead to an accelerated plasma decomposition. As another interesting point, as the intensity in Fig. 4.7 is normalised, it is clear that the re-excitation techniques increase the emission intensity, for example in the HV-LIBS experiment at 5 µs. It should be pointed out that these photos present the radiation that is collected by the camera, and not necessarily represents the plasma. For example, at 100 µs it is expected that most of the emission comes from molecular bands. Thus, although photos can provide information about the radiation emitted over time, there is not information provided on how the plasma and its species are affected by the discharge unless you put some interferometric filters in front of the camera.

In order to investigate how the plasma parameters change with both re-excitation techniques, the following sections present the results obtained in electron density and temperature.

4.5 Electron density

In this section, the results for the electron density analysis on the plasma are presented. In Sect. 2.3.4 it was studied the relation between line broadening and electron density. In addition, Stark broadening was considered to be the main contributor to spectral line broadening.

Therefore the electron density is related to the Stark broadening as

$$N_e = \Delta\lambda_s \left(\frac{N_r}{2w}\right), \tag{4.5}$$

where N_e is the electron density, $\Delta\lambda_s$ the Stark line broadening, and w the electron impact parameter. In fact, w corresponds to half of the FWHM at an electron density of reference N_r.

However, the analysis performed only had account for the contributions of the plasma interactions. It should be considered that the measurement process may interfere with the spectral measurements. The contribution of the instrumentation to the line broadening is known as instrumental broadening and can be also described by a Lorentz profile.

Then, the line profile that can be observed $I_0(\omega)$ is a convolution of the theoretical (Stark) profile $I(\omega)$ and the instrumental profile $I_i(\omega)$ [63],

$$I_0(\omega) = \int_{-\infty}^{\infty} I(x) I_i(\omega - x) \mathrm{d}x. \tag{4.6}$$

When both the theoretical and instrumental profiles have a Lorentz shape, the solution can be written as

$$FWHM_o = FWHM + FWHM_i, \tag{4.7}$$

with $FWHM_o$ as the observed width, $FWHM$ the theoretical width and $FWHM_i$ the instrumental width.

In order to determine the real width, it is needed to obtain the instrumental width. Most typical procedures involve the use of a halogen lamp. Studying its line broadening with the spectrograph, it is possible to estimate the instrumental width that arises from the spectrograph itself. In this work, another procedure was implemented. It was considered that along the time delays measured, the electron density should decrease exponentially with time. This, as in Eq. 2.58 is described. Of course, this refers to the theoretical electron density, which mainly corresponds to the Stark broadening. Then, the theoretical width should decrease exponentially with time. Thus, at the limit $t_d \longrightarrow \infty$, the Stark broadening must be negligible. Therefore, all of the line broadening observed at long delays should correspond to the instrumentation. The observed width of the Mg I (285.21 nm) transition was obtained for all the measured delays and all the spatial positions in both axes. This, only in the case of LIBS emission, to avoid effects from the discharge. Then an exponential regression was used on these data, and after taking the limit at $t \longrightarrow \infty$ it was estimated that the instrumental width is around 0.063 nm.

As described previously , instrumental and Stark contributions are the main cause of line broadening. In the case of Doppler broadening, it was shown that (Sect. 2.3.2.2)

$$\Delta\lambda_D = \lambda \frac{2}{c}\sqrt{\frac{2k_B T}{m}\ln 2}. \tag{4.8}$$

Considering a magnesium (m=24.3 uma) transition, it is needed a temperature over 50,000 K to obtain a line broadening of 0.01 nm. This temperature is significantly higher than typical LIBS temperatures, which can reach up to 20,000 K. Therefore, the Doppler contribution may be neglected. Then, it was supposed that the Stark broadening and the instrumental broadening were the only sources of line broadening. i.e.,

$$\Delta\lambda = \Delta\lambda_s + \Delta\lambda_i \tag{4.9}$$

is the real line width, where $\Delta\lambda_s$ is the Stark width and $\Delta\lambda_i$ is the instrumental width.

Substituting into Eq. 4.5, it follows that the electron density is given by

Electron density

$$N_e = (\Delta\lambda - \Delta\lambda_i)\left(\frac{N_r}{2w}\right), \tag{4.10}$$

where $\Delta\lambda$ is the observed line width, $\Delta\lambda_i$ the instrumental width and w the electron impact parameter at reference electron density N_r, which is related to the stark width as w=FWHM$_s$/2. In this case, FWHM$_s$ corresponds to the Stark broadening at electron density N_r.

For simplicity, only transition 285.21 nm of Mg I was considered in the electron density calculations. This transition has a reported Stark width (FWHM$_s$) of $7.1 \times 10^{-12}\, m$, and a electron density of reference N_r=$1.28 \times 10^{17}\, cm^{-3}$ [83]. Values obtained from from experimental measurements at 13,370 K.

Electron density was calculated at the spatial positions and time delays described in Sect. 3.2.6 and Sect. 3.2.5, respectively. First, the time-resolved results are presented in Fig. 4.9.

The figure shows the time evolution of the electron density for each experimental condition. In specific, these data corresponds to measurement centre. i.e., approximately 1.6 mm above the sample surface and the radial centre. The centre was selected because, according to Fig. 4.4, at this position, the spectral lines have the highest intensity. As previously described, for each delay three spectra were acquired. Thus, the results shown correspond to the average of these three measurements, and their error bars correspond to the standard deviation of these three measurements. Although the spectra was collected for all the time delays shown in Table 3.3, at 30 µs SNR was not sufficient for a proper analysis.

As expected, the electron density decreases exponentially in the first microseconds. Thus, it can be concluded that this time window corresponds to the regime in which $\frac{\mathrm{d}N_m}{\mathrm{d}t} < 0$. According to Sect. 2.2.3, in this region recombination may dominate. However, in all four cases the electron density is lower than 10^{19} and higher than $10^{16}\, cm^{-3}$. This corresponds to the near equilibrium

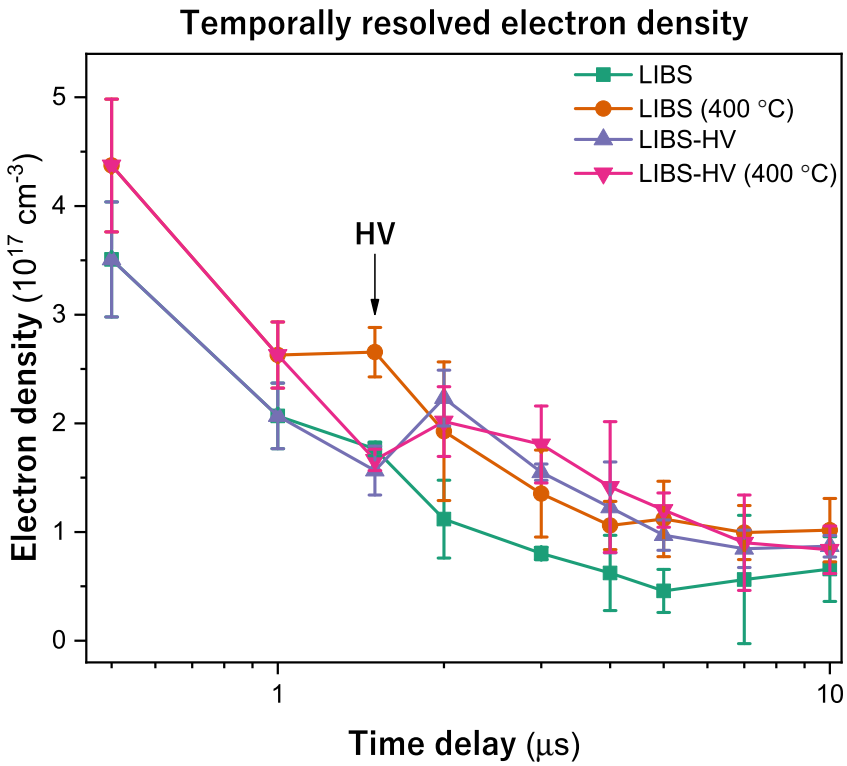

Fig. 4.9: Temporally resolved electron densities at the measurement centre for the four experimental conditions. The measurement centre is located 1.6 mm above the sample and at the radial maximum of emission. HV discharge is activated at $\tau = 1.5$ µs. Each value corresponds to the average of three measurements, and the error bars to their standard deviation.

regime. In this regime, deviations from equilibrium should be minimal and populations can be described by Boltzmann statistics.

Although this graph corresponds to only one spatial coordinate, its values should be consistent with the general picture of the plasma. Subsequently, the spatial description is discussed. In the case of LIBS, from Fig. 4.9 it is clear that it follows a decreasing exponential up to 4 µs. From this point on, the electron density stabilises around $0.5 \times 10^{17}\, cm^{-3}$. A similar evolution is observed with the heating system. In this case, the electron density is clearly higher than that at room temperature, with a tendency kept for all the observation windows.

When the discharge is triggered at room temperature no significant change in the electron density is observed. After 500 ns from the initiation of the discharge, a significant rise in electron density is observed. From this point on, the electron density decreases as usual. It was previously suggested that after 5 µs, almost 3/4 of the total energy provided by the discharge was already deposited through plasma boundaries. In fact, the difference between LIBS electron density and LIBS-HV electron density decreases around 5 µs. Approximately around the last observed time, it can be suggested that the LIBS-HV electron density is about to converge to the LIBS electron density.

A similar behaviour is observed when both re-excitation techniques are used. However, there are interesting differences. In the LIBS-HV case, it is observed that the electron density does not change at the discharge trigger time. In contrast, with the heating system, there is

observed a decrease in electron density. This can be attributed to two factors. First, the different atmospheric temperatures at which the discharge appears. The heating system may, for example, change the local humidity percent which can affect the air breaking conditions for the spark. However, it is also possible that the discharge system is not constant over time. i.e., in the room temperature case the discharge was triggered a few ns later than in the heated case. As the gate delay and gate width were constant at each time, this can cause differences in the amount of radiation recollected if the discharge triggering time deviates. However, this effect should be negligible due to the time delays used. Therefore, it should be suggested that the main factor which alters the discharge behaviour is the heated atmosphere.

After the triggering time, the electron density increases. However, this increase is only sufficient to reach the observed magnitudes for each individual re-excitation technique. Thus, it can be suggested that their effects do not add linearly. At longer delays, its electron density decreases and converges to LIBS-HV electron density.

Nevertheless, it should be remembered that these data corresponds to just one plasma spatial point and the global behaviour may be different. Thus, it is necessary to discuss the spatially resolved electron density, which is shown in Fig. 4.10 and Fig. 4.11 for the axial direction.

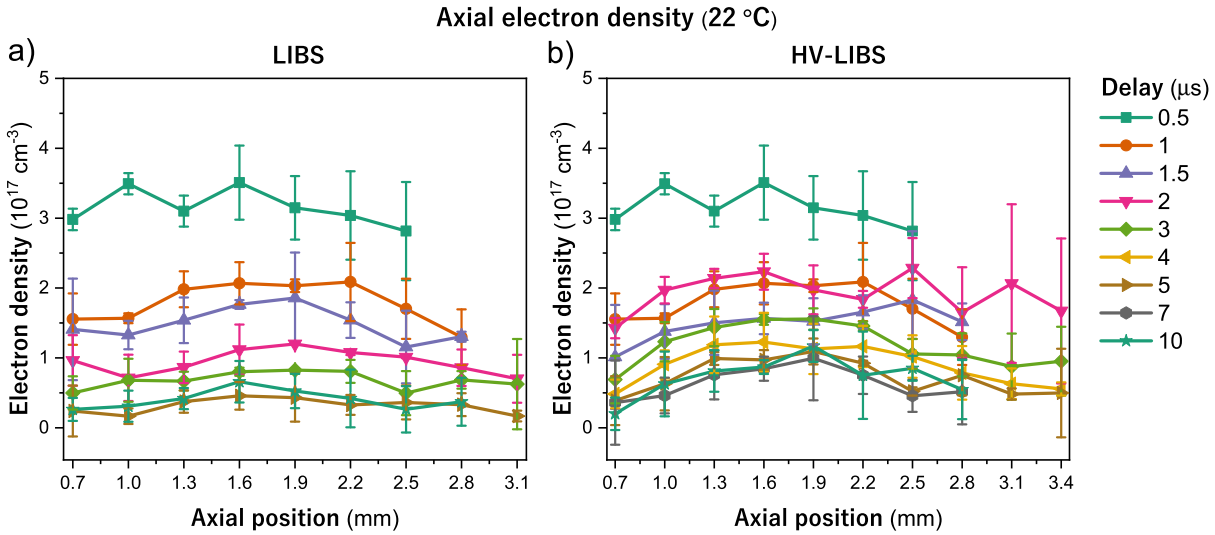

Fig. 4.10: Spatially resolved electron density in the axial direction. Delay times are measured after the laser onset. For the sake of clarity, not all the data is presented in LIBS case. Error bars correspond to the standard deviations of three measurements. The zero in the axial position corresponds to the surface of the sample. a) LIBS b) LIBS with a HV discharge triggered at 1.5 µs after the onset of the laser.

Fig. 4.10a) shows the spatially resolved LIBS electron density. It was calculated along the axial direction for all the time delays from 0.5 up to 10 µs. As the figure shows, far from the centre, the electron density decreases slightly. It results in a sort of parabolic symmetry in the range of 1 to 3 µs, as the spectral intensity in Fig. 4.4. In the rest of the delays, it is approximately constant on this axis. In addition, its temporal evolution is also uniform in the axial direction. It should be noted that even though all the measurement zones in Fig. 3.14 were collected, only positions with sufficiently high SNR spectra were analyzed. Thus, for the LIBS measurements, the spectral emission is sufficiently high, about 0.7 mm over the sample

surface. In contrast, far from the surface, the signal quality increases with time. Thus, the higher measurement position ranges between 2.5 to 3.1 mm from the surface. This may be due to the recombination process. At low delays, the plasma has a high ionization degree. As it decreases, the SNR of the neutral transition used increases. However, at 10 µs the neutral emission at the plasma boundaries has decreased significantly.

On the other hand, Fig. 4.10b) shows the case when a high voltage discharge is applied at 1.5 µs. It is clear that the discharge effect can be observed at 2 µs. At this delay, there is a general increase in electron density along all the axial direction. It can be also noted that the error bars increase significantly at higher positions above the surface. This behaviour can be due to the interaction between the discharge and the surrounding atmosphere.

At 3 µs the electron density decreases to values similar to those without discharge. This was previously observed in Fig. 4.9. However, in the LIBS case, it was not clear if the electron density has any kind of symmetry at longer delays. The LIBS-HV electron density profile may suggest that the electron density indeed has a concave profile along the axial direction. However, the lack of SNR at the boundaries causes the profiles not to be significantly different.

In addition to the zones reported in the LIBS case, it was observed an increase of SNR on the transition studied. After the HV discharge it was possible to study the plasma electron density up to 3.4 mm above the surface. However, the error bars also increase far from the surface. This may also be due to the effect of the discharge on the surrounding atmosphere. Then, a similar effect might be expected when the surrounding air is heated.

Likewise, Fig. 4.11 shows the electron density profile when the sample was heated to 400 °C. These profiles correspond to the axial direction in both cases: with and without the high voltage discharge.

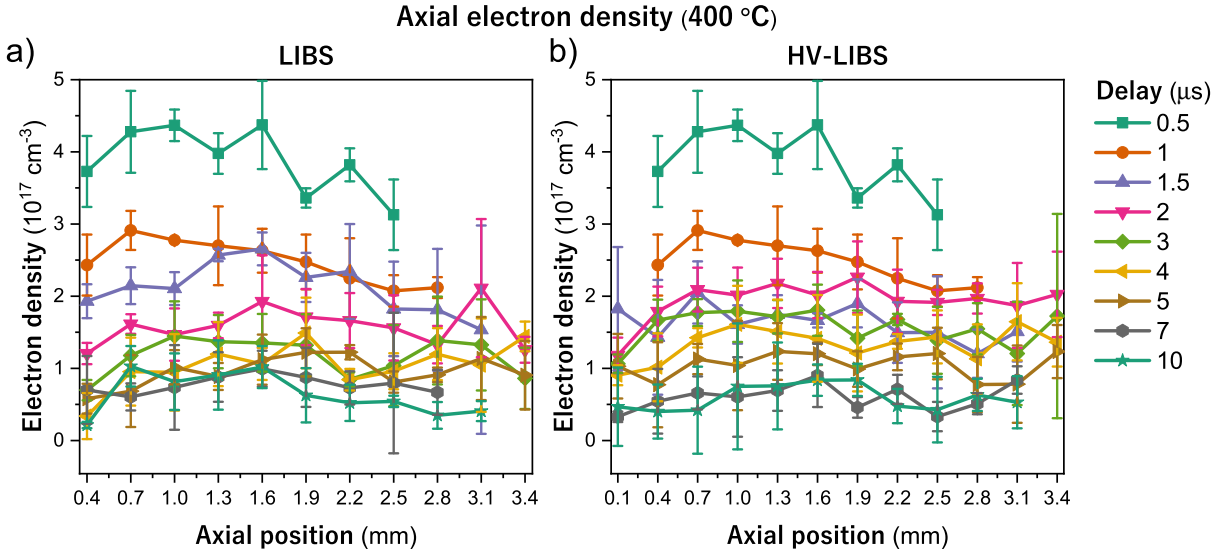

Fig. 4.11: Spatially resolved electron density in the axial direction. Error bars correspond to the standard deviation of three measurements. The zero in the axial position corresponds to the surface of the sample. a) LIBS at 400 °C b) LIBS with a HV discharge triggered at 1.5 µs; at 400 °C

Fig. 4.11a) shows the electron density profile of LIBS at 400 °C. This corresponds to the axial electron density with time delays of 0.5 to 10 µs. For each point, the average of three measurements is shown. The error bars correspond to the standard deviation of these measurements.

As expected from the temporally resolved profile (Fig. 4.9), Fig. 4.11a) shows a general increase in electron density when the sample is kept heated. Furthermore, it is observed that near the centre (1.6 mm), the electron density decreases slower, as a function of time, that at the boundaries. Although the general behaviour is similar to that of room temperature, it is clear that when the sample was heated the error bars increased significantly. This may be because the plasma electron density or the plasma expansion is dependant of the atmosphere. Therefore, the heating system might negatively affect the stability of the atmosphere.

For most delays, the electron density has a profile that resembles the LIBS profile. However, at short delays it seems that there is a preferential increasing direction. This, because electron density profiles shown a higher increase near the sample and an almost linear decreasing with distance from the sample. This happens only before 2 µs, which could be a residual effect of the initial plasma expansion, in which the first free electrons occur near the ablation spot. Another explanation may be the heating process. As there is an increase in the removed matter, it may need more time to be ionised.

The relation between target properties (R, reflectivity; α, absorption depth; ρ, mass density; c, specific heat capacity), and the temperature change (ΔT) when its surface is impacted by a laser intensity with I_0 was obtained by means of Eq. 2.52:

$$(1 - R)\, I_0 \alpha t = \rho c \Delta T. \tag{4.11}$$

Let's suppose that the target properties are approximately constant with temperature and that the sample starts its ablation when a temperature T_a is reached. It is clear that $T_a - 20$ °C $> T_a - 400$ °C. Then, it may be expected that after the sample was heated, the energy that is needed to start vaporisation is lower than that at room temperature. Also, it takes less time to be ablated.

In the time-width between ablation at room temperature and ablation at 400 °C, the laser energy continues to impact the target. This process lasts up to the plasma becomes optically thick to the laser wavelength. However, even though this time width between ablation and an optically thick plasma was the same for both target temperatures, the target at high temperature ablates easily. This leads to an increase in removed matter. A considerable increase in the removal of matter should increase the number of species in the vapour. This leads to more free electrons, which increase the ionisation via inverse Bremsstrahlung. In addition, collisional processes should increase in ratio due to a higher kinetic energy within the species. All of these processes lead to an increase in electron density and plasma emission. If the increase in electron density is faster than the plasma expansion, it may lead to a higher electron density near the target.

Although this analysis is in good agreement with what is known about this experiment, the physical properties of the sample were not studied. Furthermore, in the derivation of Eq. 2.52

it was supposed that the thermal conductivity of the sample was negligible. Then, a complete study of how the temperature of the sample affects a LIBS plasma and ablation process must include a study on the target properties and how they respond to temperature changes.

The case with both re-excitation techniques is depicted in Fig. 4.11b). As observed in the previous results, the electron density increases after the discharge is applied. In this case, it seems that the electron density is in general higher than all the previous electron density profiles studied.

However, the behaviour discussed in the last paragraphs changed significantly when the discharge was applied. The error bars increased and is not clear whether the profile is shifting apart from the surface. This change in the structure of the profile seems due to the heating. From a comparison of Fig. 4.10b) with Fig. 4.11b), it can be suggested that when the sample was heated, the spatial profiles of the electron density become more diffused. This change should be caused by the change in the surrounding atmosphere, which influences how the plasma expands.

Another interesting fact is that in both LIBS at 400 °C and LIBS-HV at 400 °C the measuring region increased. This may be due to the decrease in atmospheric density, which leads to a increase in plasma volume. Heating the sample allows for the SNR to increase considerably from 0.4 to 3.4 mm above the sample. On the other hand, when discharge is applied, the enhancement is 0.1 to 3.4 mm above the surface. It is not clear from these graphs how the emission region changes with each technique.

Of the two techniques investigated, it is clear that the heating might affect the axial direction of the plasma. However, the discharge does not have a specific direction.

To investigate how the high voltage discharge affects the plasma, its electron density in the radial direction was also studied. Fig. 4.12 shows the spatial profile of the electron density along the plasma radial axis.

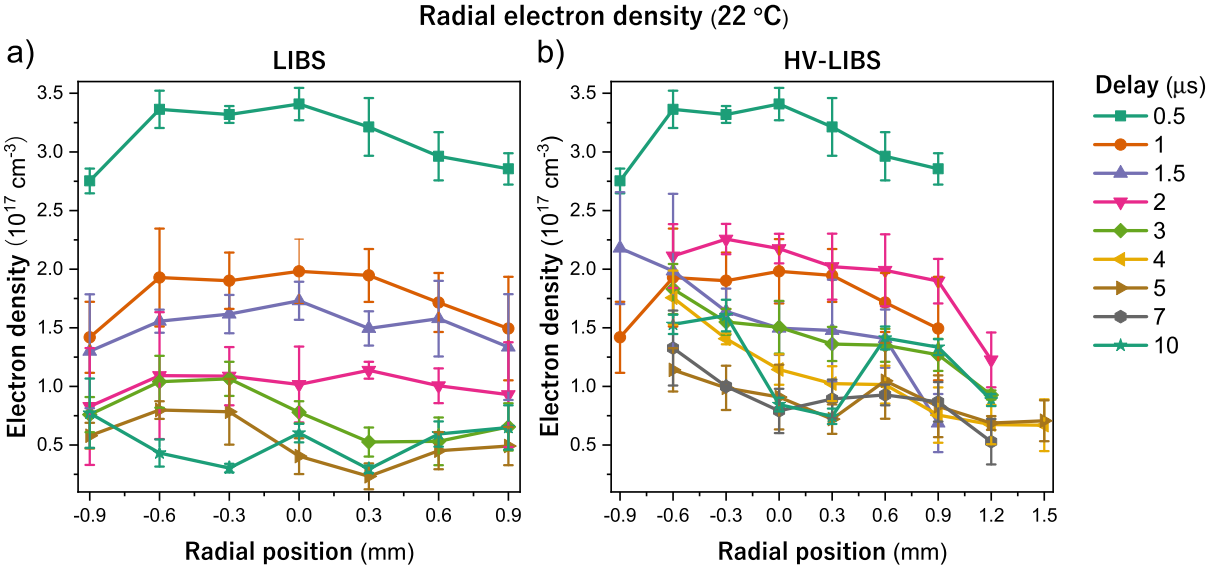

Fig. 4.12: Spatially resolved electron density in the radial direction. The zero in position corresponds approximately to the maximum of emission. For the sake of clarity, not all the data is presented in LIBS case. a) LIBS. b) LIBS with HV discharge applied at 1.5 µs.

As Fig. 4.12a) shows, the electron density profile is approximately symmetric along the radial axis, again with a concave shape. However, with delays longer than 3 microseconds, it starts to lose its shape.

In contrast, Fig. 4.12b) shows how the HV discharge affects the electron density in the radial direction. In the axial case, the main effect of the discharge was an increase in the electron density and an increase in SNR at the limits. This case shows a significantly different result. Few µs after discharge triggering, the electron density increases. However, this effect may be asymmetric. The left side, where the grounded electrode is located, may increase its electron density more than the right side. This behaviour starts to decline at 5 µs, which seems to be correlated with the main time interval of energy deposition by the HV discharge. i.e., the HV discharge increases the electron density of the plasma, but this increase is significantly higher at the side of the grounded electrode.

At 10 µs the electron density profile loses its shape. Then, this may suggests that the HV discharge perturbs the further emission of the plasma. This is because at this delay almost all the energy was already deposited.

Finally, it is observed that only on the right side of the plasma there was an increase in emission. It should be remembered that the electron density was calculated with a neutral transition. On the other hand, on the left side, the error bars increase significantly with discharge. Thus, these results may suggest that the recombination process is also affected by the discharge and has a preferential direction. In this case, it is higher on the side of the charged electrode. At first, this may be due to the electrodes polarization. However, as the discharge oscillates with time, it is not clear if there should be a preferred direction for the recombination. In the following sections, the discussion regarding this effect is continued.

In this section, the spatial and temporal profile of the electron density was studied. It was observed that the re-excitation techniques increase electron density. However, the discharge effect on the plasma decreases significantly after the first microseconds, because most of the energy is deposited at short delays. It was also found that heating the sample may affect how the plasma expands in the axial direction. To understand how the heating system affects the plasma, a heat equation was used. However, this analysis was severely limited by limited knowledge of the properties of the sample. In general, the enhancement of the SNR by heating the sample was attributed to the increase in species due to an improvement in the removal of matter. In both the axial and the radial directions, it was suggested that the plasma has a concave shape. This result agrees with previous investigations by Corsi et al. [84]. The authors studied copper transitions from a plasma formed in a copper disk and also found that the electron density profile has a concave shape. The axial shift in electron density was also obtained by De Giacomo et al. [85] in their investigation with an aluminium target. The authors mainly used transitions from aluminium and attributed the axial shift to the distribution of the species and the recombination processes in regions of high species electron density. In addition, in the radial direction was found that there is an apparent preferential direction for the electron density increase in LIBS-HV experiments, as observed in Fig. 4.13. The figure shows the same data presented previously, but rearranged to improve clarity.

From Fig. 4.13a) it is clear that the increase in electron density is approximately uniform along the axial direction. However, Fig. 4.13b) shows that the electron density on the side of

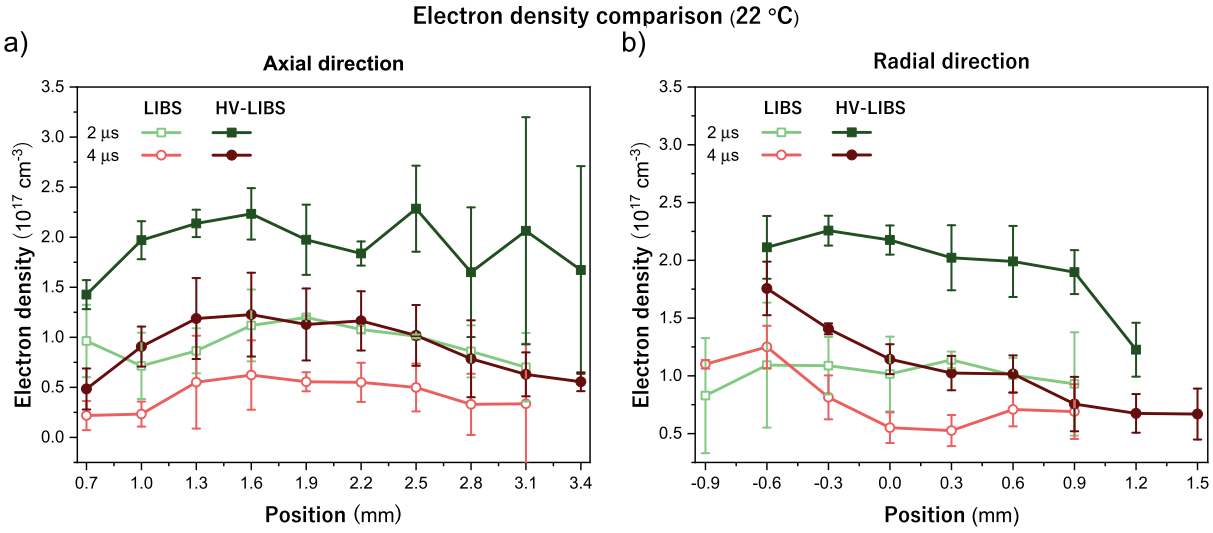

Fig. 4.13: Electron density comparison of LIBS with HV-LIBS at 2 and 4 µs. Error bars represent the standard deviation of three measurements. a) Axial direction b) Radial direction

the grounded electrode is higher than that on the right side. This discrepancy in the electron density could be attributed to varying recombination rates, which becomes a central focus in the upcoming sections. In the next section, the other fundamental plasma parameter is investigated.

4.6 Plasma temperature

In this section, the calculations used to obtain the plasma temperature are explained. The temperature is studied with temporal and spatial resolution for the re-excitation conditions described in the past chapters.

The difficulties with the definition of the plasma temperature were addressed in Chapter 2. In Sect. 2.3.6, in order to relate the populations at different levels and the plasma parameters (N_e, T), the Saha-Boltzmann equation (Eq. 2.120)

$$\underbrace{\ln\left(\frac{I^z_{nm}\lambda_{nm}}{A^z_{nm}g^z_m}\right) - z\ln\left[2\left(\frac{m_e k_B}{2\pi\hbar^2}\right)^{\frac{3}{2}}\frac{T^{\frac{3}{2}}}{N_e}\right]}_{\mathrm{y}} = \underbrace{-\frac{1}{k_B T}}_{\mathrm{m}}\underbrace{\left[E^z_m + \sum_{k=0}^{z-1}(E^k_\infty - \Delta E^k_\infty)\right]}_{x} + \underbrace{\ln\left(\frac{hcN^0}{Z^0(T)}\right)}_{b}, \tag{4.12}$$

was derived, with the correction for the ionization potential

$$\Delta E^{z-1}_\infty = 3z\frac{e^2}{4\pi\epsilon_0}\left(\frac{4\pi N_e}{3}\right)^{\frac{1}{3}}. \tag{4.13}$$

In this equation, for the transition $m \longrightarrow n$; I_{nm} is the line emission, λ_{nm} the wavelength for the transition, A_{nm} the transition probability, g_m the degeneracy, z the ionization degree, m_e the electron mass, k_B is Boltzmann's constant, $\hbar$ is the reduced Planck's constant, T the temperature, N_e the electron density, E_k the energy of level k, h is Planck's constant, c the

speed of light, e the unit charge, ε_0 is the vacuum permittivity, and N^0, Z^0 are the population and partition function for ground level, respectively. In addition, the super index z is used to indicate the degree of ionization.

From those parameters, the electron density was calculated in the last section, and the line emission is obtained from the spectral area. To solve this equation numerically, the only extra terms needed are the transition probability, upper-level degeneracy and upper-level energy. These parameters are reported in Table 4.1.

Table 4.1: Parameters used to solve the Saha-Boltzmann equation. The wavelength of each transition (λ_{nm}), the energy of upper level (E_m) and the product between transition probability and upper level degeneracy ($A_{nm}g_m$) were extracted from NIST atomic database [79].

λ_{nm} (nm)	E_m (eV)	$A_{nm}g_m$ $(10^8\,1/s)$
279.0776	8.863762	16
279.5528	4.433784	10.4
279.7998	8.863654	28.7
280.2704	4.422431	5.14
285.2127	4.3458029	14.7

The transitions used were from the neutral and ionic magnesium species and thus, $z \in \{0, 1\}$. Then, it follows that

$$\sum_{k=0}^{z-1}(E_\infty^k - \Delta E_\infty^k) = E_\infty^0 - 3\frac{e^2}{4\pi\epsilon_0}\left(\frac{4\pi N_e}{3}\right)^{\frac{1}{3}}. \tag{4.14}$$

Therefore, only the ionization energy of the neutral species, $E_\infty^0 = 7.646236\,eV$ [79], is needed.

These parameters constitute all the necessary data for solving the Saha-Boltzmann equation using the Saha-Boltzmann method. In this numerical approach, Eq. 4.12 lacks an analytical solution for temperature. The numerical solution is obtained by assuming a linear structure for the equation, represented as $y(x) = mx + b$. For this task, a computer programme in the C language was developed. The programme features an iterative algorithm with two key sections: one calculating the x-values and the other determining the corresponding y-values, as in Eq. 4.12. This was performed using the parameters measured experimentally and the tabulated values. Then, a second module performs a least squares algorithm that produces the parameters for the linear equation, as depicted in Fig. 4.14. The graph visually represents the linear relationship assumed in the Saha-Boltzmann method.

The figure shows the values plotted for HV-LIBS, obtained at 2 µs after the laser onset, and at the centre of the plasma. As depicted, each transition results in a pair (x, y) obtained through Eq. 4.12, using an initial temperature. The algorithm iteratively refines the temperature estimate using the obtained values, with each iteration employing the calculated temperature as the new initial value. The regression process obtains, from these data points, a straight line and from its slope, $m = -\dfrac{1}{k_B T}$, the temperature is calculated. Typically, the algorithm produces

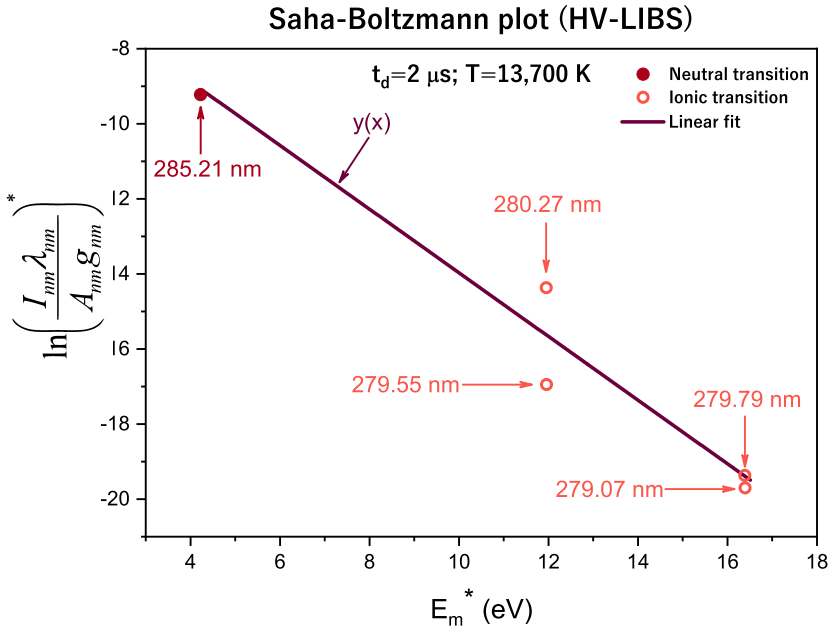

Fig. 4.14: Saha-Boltzmann plot obtained in HV-LIBS, measured in the centre at 2 µs after the laser onset. $\ln\left(\frac{I_{nm}\lambda_{nm}}{A_{nm}g_m}\right)^* = \ln\left(\frac{I_{nm}\lambda_{nm}}{A_{nm}g_m}\right) - z\ln\left[2\left(\frac{m_e k_B}{2\pi\hbar^2}\right)^{\frac{3}{2}}\frac{T^{\frac{3}{2}}}{N_e}\right]$ and $E_m^* = E_m + \sum_{k=0}^{z-1}(E_\infty^k - \Delta E_\infty^k)$; as in Eq. 4.12. y(x) is the linear fit to the data, from the slope of which a temperature of about 13,700 K is estimated.

consistent results for a wide range of initial temperatures. In this instance, an initial temperature of 10,000 K was chosen. The iteration continues until an arbitrary difference of 0.005% between successive temperature estimates is reached[3].

With this method, the plasma electron temperature was obtained. This, for all the four conditions specified, the gate delays from Table 3.3 and the spatial position zones from Fig. 3.14. In total, 471 electron density and temperature pairs were obtained. In Fig. 4.15 the temperature resolved in time is presented. As discussed previously, three measurements were made in each time delay. Then, the average of these three measurements is presented. The error bars reported correspond to the standard deviations of these measurements. As shown, the temperature was obtained in the range from 0.5 µs to 10 µs. Although the radiation from 30 µs was also collected, its low SNR made the Saha-Boltzmann equation unsolvable at that delay.

As the figure shows, the temperature magnitude ranges from 9,000 K to 15,000 K, aligning with typical temperatures reported for LIBS plasma. A first comparison between Fig. 4.9 and Fig. 4.15 reveals that the electron density exhibits an exponential decrease, particularly at shorter delays. However, this behaviour is damped at longer delays. In contrast, the electron temperature experiences an exponential decrease in the case of LIBS. Moreover, when the sample is heated, a similar trend is observed, but with a higher overall temperature than that of LIBS. This heated case also displays a more unstable progression, possibly influenced by the heating system's effect on the surrounding atmosphere.

[3]It should be pointed out that this is an arbitrary and exhaustive choice, because the the typical error in temperature calculations in LIBS can reach 10%.

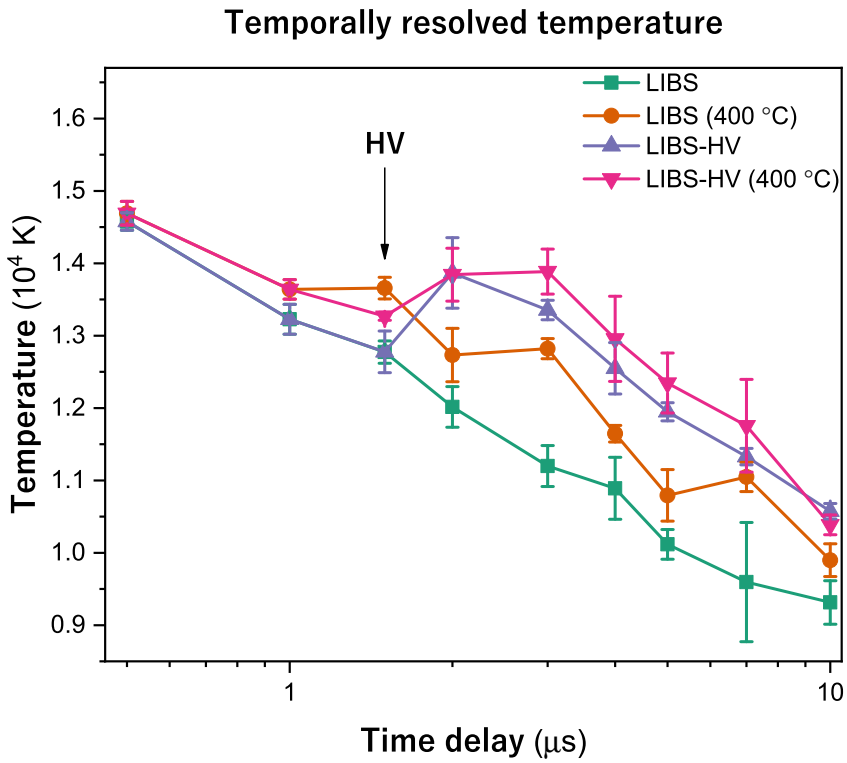

Fig. 4.15: Temporally resolved temperatures at the measurement centre for the four experimental conditions. The measurement centre is located 1.6 mm above the sample and at the radial maximum of emission. The HV discharge is activated at $\tau = 1.5$ µs. Error bars represent the standard deviation of three measurements.

Regarding the high-voltage discharge, its effect is consistent for both room temperature and heated cases. In the room temperature case, the discharge significantly increases the temperature at 2 µs, followed by an exponential decrease. This behaviour remains almost identical when the sample is heated to 400 °C. This is another indication that the effects of both techniques do not add linearly.

The spatial resolutions for the temperature are discussed in the following paragraphs. First, the axial electron temperature measured at room temperature is presented in Fig. 4.16.

Fig. 4.16a) shows the temperature along the axial direction in LIBS. The maximum height of measurement was mainly limited to the zones in which the electron density was obtained. It is clear that unlike the electron density, the temperature is approximately constant over the axial direction. Even the error bars are almost negligible at short delays. However, this changes when the delay increases. At longer delays, it seems that the temperature also exhibits a concave shape. This should be an inherited property from the electron density. These changes with time may be because after the plasma recombines, it starts deviating from equilibrium.

The fact that the temperature is approximately constant has one important implication. Although the LTE model may be described as demanding, it is actually consistent with LIBS plasmas. However, it is necessary to study the radial direction, which is expected to have the same behaviour.

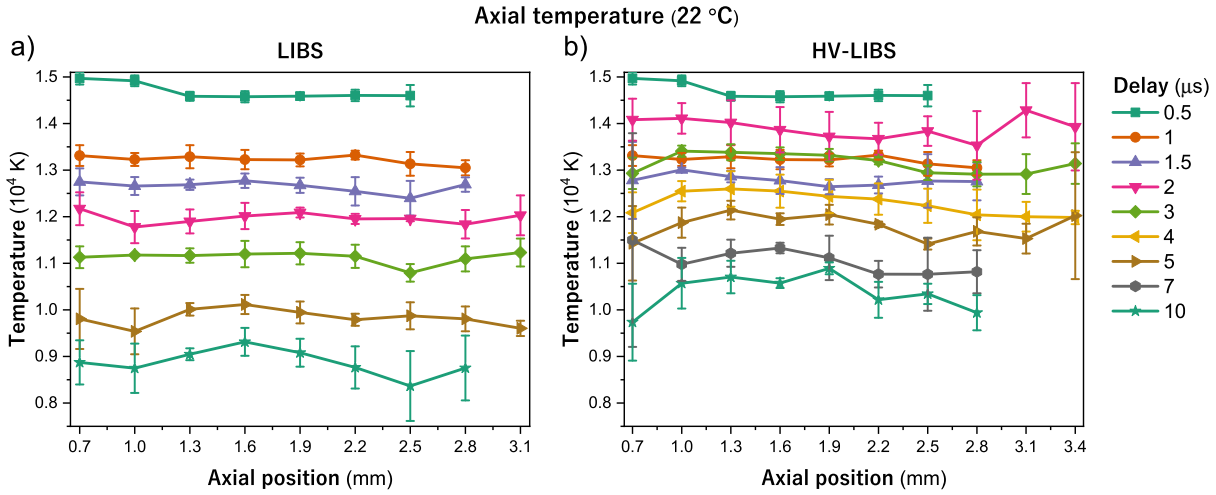

Fig. 4.16: Spatially resolved temperature in the axial direction. Delay times are measured after the laser onset. For the sake of clarity, not all the data is presented in LIBS case. Error bars correspond to the standard deviations of three measurements. The zero in the axial position corresponds to the surface of the sample. a) LIBS b) LIBS with a HV discharge triggered at 1.5 µs after the laser onset.

The case with a HV discharge applied at 1.5 µs is represented in Fig. 4.16b). The main effect of the discharge is, as previously observed, at 2 µs and 3 µs. At these delays, the temperature is higher than at 1.5 µs. This behaviour also is observed along all the measurement zones. In fact, the measurement zones are increased up to 3.4 mm above the target.

As depicted in the figure, temperatures measured in the initial microseconds of the discharge exhibit increased error bars, suggesting a deviation of the plasma from equilibrium due to the interaction with the discharge. This effect is particularly notorious at 2 µs. Subsequently, error bars decrease at longer delays, indicating a potential return of the plasma to equilibrium a few microseconds after the discharge initiation. This observation also hints at the rapid relaxation speed of the plasma. Thus, in the equilibrium state of the plasma the discharge can be considered as a short perturbation centred around 2 µs. However, it is observable that the temperature displays more irregularities compared to LIBS temperatures after the discharge is applied.

Most of the changes observed when the HV discharge was applied seem to have been inherited from the electron density. As the HV discharge constitutes an electron flux, these electron may collide with the internal species and enhance the ionization. As Fig. 4.12b) shown, the electron density may be higher at the side of the grounded electrode. Thus, it should be expected that the temperature also shows a radial asymmetry.

In Fig. 4.17 the experiments performed with the heating system are presented. Both cases are presented, with and without the HV discharge. Likewise previous cases, each measurement consist of the average of three measurements and the error bars correspond to their standard deviation. As the figure shows, heating the sample increases the SNR at the boundaries. This allows to increase the measurement range to 0.4-3.4 mm above the target for LIBS at 400 °C and 0.1-3.4 mm for LIBS-HV at 400 °C.

Fig. 4.17a) shows the axial temperature of the plasma when the sample was heated to 400 °C. Similarly to previous cases, the temperature exhibited high axial symmetry, remaining

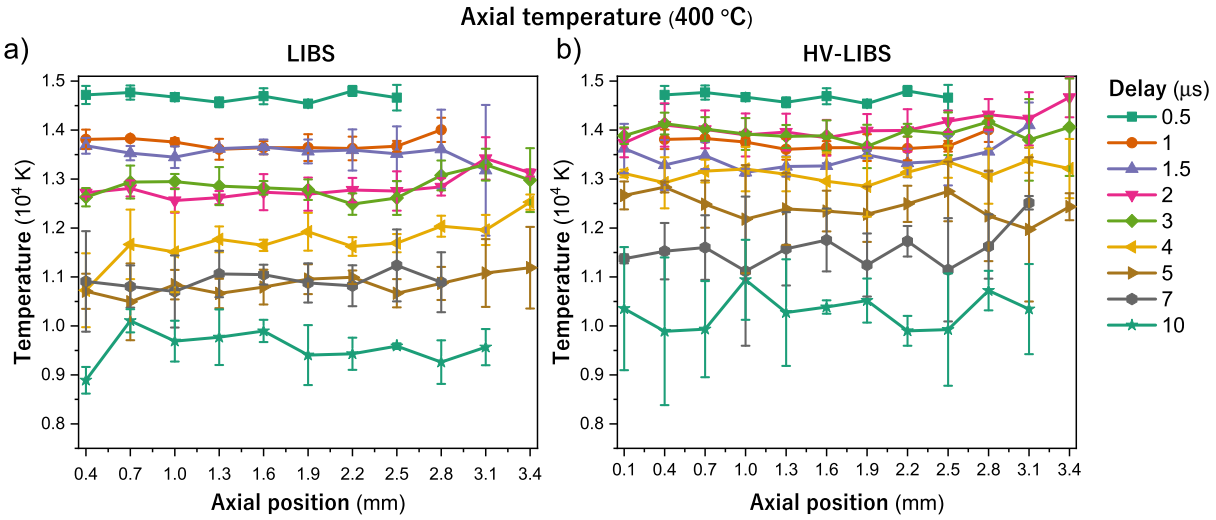

Fig. 4.17: Spatially resolved temperature in the axial direction. Error bars correspond to the standard deviation of three measurements. The zero in the axial position corresponds to the surface of the sample. a) LIBS at 400 °C b) LIBS with a HV discharge triggered at 1.5 µs; at 400 °C.

approximately constant along the vertical axis. Compared to the room-temperature case, the error bars showed a slight increase, possibly indicating that the heating system perturbed the plasma and deviated its state from equilibrium, although to a lesser extent than the HV discharge at room temperature. However, the main difference is that the discharge perturbation is centred around 2 µs, whereas heating is applied throughout the entire plasma lifetime.

The figure also shows that heating the sample influences the rate of temperature decrease over time. The temperature profiles show arbitrary pairs at certain intervals, such as 1 to 1.5 µs, 2 to 3 µs, and 5 to 7 µs. This apparent grouping might be due to the increased error bars.

Fig. 4.17b) shows the temperature profiles with the simultaneous application of the two re-excitation techniques. These profiles combine some of the features of Fig. 4.16b) and Fig. 4.17b). The temperature increases significantly at 2 µs and has almost the same value at 3 µs. In fact, the profiles for the range between 1.5 and 4 µs are kept at almost the same temperatures. This range coincides with the main range of the energy deposition by the discharge. Thus, the high-voltage discharge is also capable of influence the rate of temperature decrease. This is also observable in Fig. 4.16b). It should be noted that error bars also have a significant increase. Then, using both techniques enhances the SNR, the temperature, and the electron density, but may depart the plasma from LTE. As with discharge, most of the changes observed when the sample was heated can also be attributed to an increase in the electron density. In fact, a more ionized plasma should emit more. Also, the more the ionization, the more energized are the species.

The fact that the temperature increases uniformly with the application of the discharge is interesting because the discharge is applied asymmetrically. The grounded electrode has an approximately horizontal orientation, while the charged electrode is usually in a diagonal orientation. Thus, it is necessary to analyze where the discharge is applied, and whether it is axially symmetric. This was performed by means of fast photography and was discussed in Sect. 4.4. It was found that the application position is not exactly the same in each discharge. Also, it

changes when the sample is heated and is not axially symmetric. Thus, the temperature and density axial profiles don't significantly change their shape with the discharge.

Therefore, except for longer delays, it was shown that the temperature is axially symmetrical. Along the positions measured, it is approximately constant. Then the high-voltage discharge does not affect the axial symmetry, although the electrodes do not follow this symmetry. To conclude this section, it is necessary to study whether the high-voltage discharge affects the radial symmetry of the temperature, as with the electron density.

Fig. 4.18 shows the radial profiles of the temperature, with and without the high-voltage discharge. Likewise, these profiles were obtained as the average of three measurements. The error bars correspond to the standard deviation of those measurements.

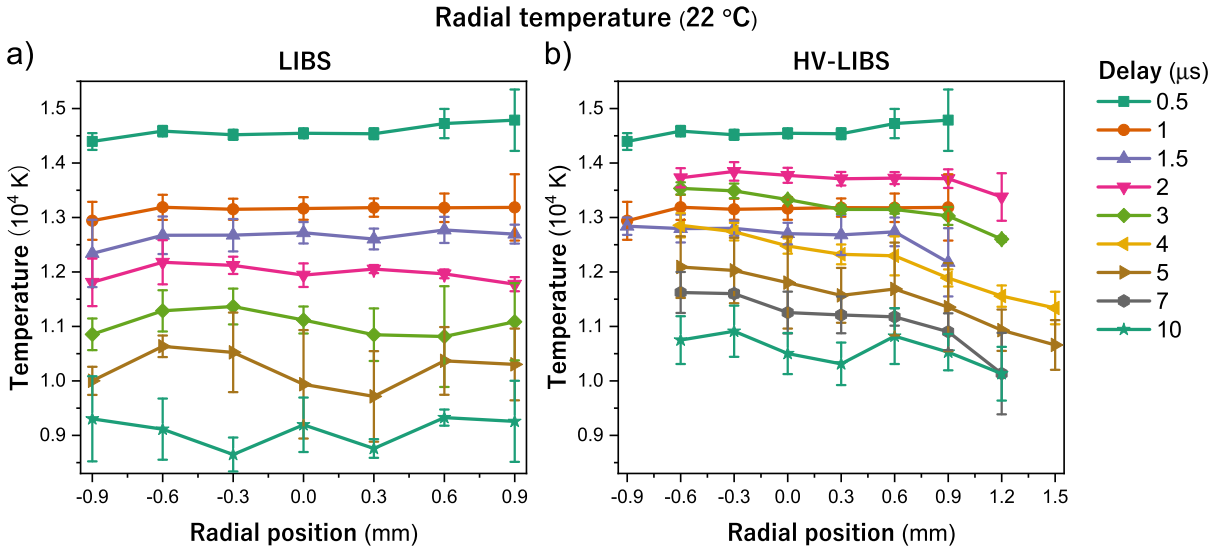

Fig. 4.18: Spatially resolved temperature in the radial direction. The zero in position corresponds approximately to the maximum of emission. For the sake of clarity, not all the data is presented in LIBS case. a) LIBS. b) LIBS with HV discharge applied at 1.5 µs.

Fig. 4.18a) shows the spatially resolved profile for the radial temperature. It is shown that, like the electron density, is symmetrical along the radial axis. However, after 3 µs after the laser onset, its behaviour becomes more unstable with time. This may again be an indication that the plasma tends to deviate from its LTE condition at longer delays.

In contrast, it is clear from Fig. 4.18b) that the HV discharge affects the radial symmetry. On the left side of the plasma, the measurement zone is not expanded, but the temperature increases significantly at -0.9 mm from the centre. Moreover, there is a further increase at -0.6 mm from the centre. This increase is significant only in the LIBS-HV profiles after 1.5 µs. However, the main difference with respect to the LIBS case is that in Fig. 4.18b) the temperature continuously decreases from this point to the right side of the plasma. However, even on the right side of the plasma, its temperature is higher than in the LIBS case. Furthermore, at the right side of the plasma the measurement zone is increased up to 1.5 mm far from the centre. This is in agreement with the results obtained in electron density.

Although Fig. 4.12b) suggested that the electron density decreases with respect to the radial position, it was not explicitly indicated whether this effect is apparent. In this case, it is clear that the plasma temperature is increasing asymmetrically. This effect is maximal at 4 µs and less clear after 7 µs. This temporal range agrees with the information obtained from the energy graph (Fig. 4.3).

From these results, it may be suggested that the rate of recombination is higher on the side of the charged electrode. This is because both the temperature and electron density are lower on this side. Thus, the electron flux from the grounded electrode heats the plasma left side, but this effect decreases with the radial position as the position increases. This may be a collisional effect caused by the interaction between the electron flux and the plasma species. Thus, these effects are mainly concentrated in the side of the grounded electrode.

However, as shown in Fig. 4.2, an oscillatory discharge was used. Thus, there should not be a preferential direction for the electron flux. In this case, it is possible that the discharge oscillations ionize and heat both plasma sides. From 4.2 it is clear that the integral of the current will have a similar shape to the energy graph. i.e., the total current is positive, thus most of the energy is deposited on the left side of the plasma.

The main result from this section is that the plasma temperature is mostly symmetric in both axes. However, the HV discharge induces a temperature asymmetry in the radial direction of the plasma. It was found that both re-excitation techniques increase the plasma temperature. In the heating case, this was attributed to an increase in electron density and thus to an ionisation enhancement. In contrast, it was suggested that the HV discharge heats the plasma by collisions. However, this increase in temperature was also found to be highly asymmetric, as shown in Fig. 4.19.

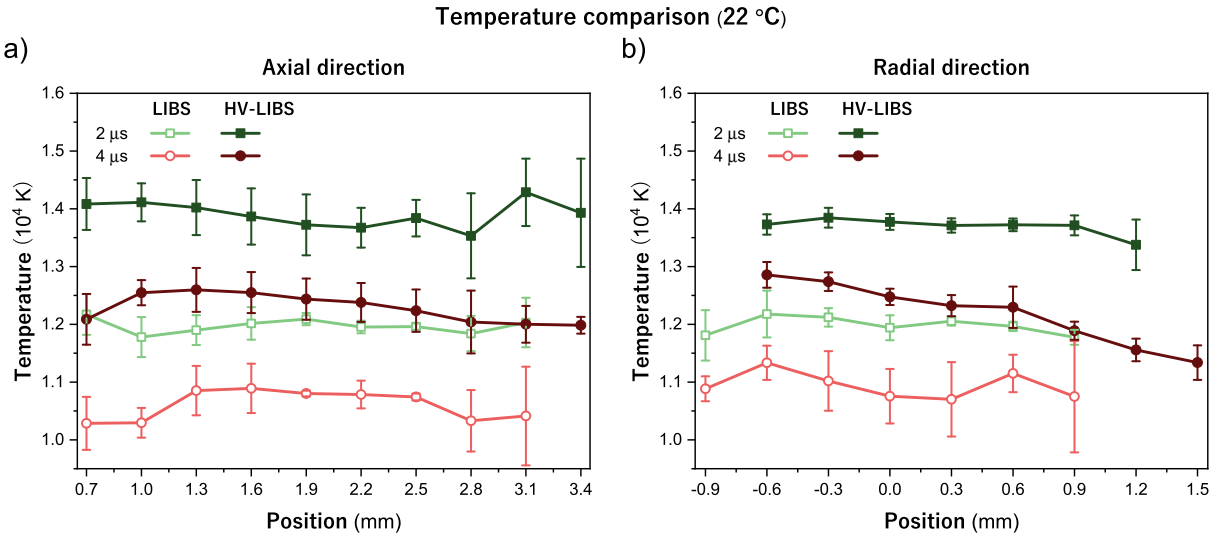

Fig. 4.19: Temperature comparison of LIBS with HV-LIBS at 2 and 4 µs. Each value corresponds to the average of three measurements, and the error bars to their standard deviation. a) Axial direction b) Radial direction

It can be observed that along the axial direction (Fig. 4.19a)) both LIBS and HV-LIBS exhibit a plane profile. However, in the radial direction (Fig. 4.19b)) it is clear that after the discharge is applied, the increase in temperature is asymmetric. This asymmetry is interesting

because the discharge should not have a preferential direction. Therefore, it was proposed to study how the discharge impacts the plasma and what its effect in the species is.

On the other hand, heating the sample affects the rate of decrease in temperature. This is also in agreement with the results obtained for the electron density. Also, this is a consequence of the extended lifetime of the plasma, which was observed in the fast photography results.

The results obtained in this section are mostly in agreement with those of the literature. For example, in studies such as the one by Aguilera et al. [68] it was found that the plasma formed on Fe-Ni alloys were axisymmetric. They studied the temperature along both the vertical and radial axes and found temperatures about 14,000 K near the plasma centre. However, in their work, the plasma temperature decreased at the boundaries. At these positions, they were not capable of using the Saha-Boltzmann equation, due to the weak emissivity. Their analysis was completed using the Boltzmann equation. For the axial temperature, they reported a hotter plasma near the sample than at the upper border.

The main differences with this work and the literature arise from the low SNR obtained near the boundaries. Also, to the low resolution used in both axes. However, the literature shows agreement with the temperature symmetry, which was not preserved when the discharge was applied. Therefore, the first observation that should be raised from these results is that although the discharge affects both directions, the plasma parameters only change along the radial axis. Also, as Fig. 4.7 shown, the discharge can be applied at different plasma heights, yet both electron density and temperature does not significantly change. Thus, it remains unclear what the discharge is actually doing to alter the symmetry of the parameters, only over the radial direction. Also, it is not clear why, although the discharge oscillates, there is a preferential direction for its effects.

To analyse some of these statements, it is necessary to study whether the HV discharge has a different net impact at both sides of the plasma. This study of the plasma morphology was carried out by means of fast photography, the results obtained were already presented. It was shown that the discharge is not symmetric. However, it was not observed a significant change along the radial direction, as observed in this section. Then, a better analysis is needed. A spectral analysis of the plasma species was performed to study the internal effect of the discharge. This is presented in Sect. 4.7.

4.7 Plasma species

To investigate how the internal distributions of species change when the discharge is applied, their emission maxima were analysed. Fig. 4.20 shows the analysis on the position of the species' maximum position when the discharge is applied to the plasma.

Fig. 4.20a) shows the temporal evolution of the maximum emission position long the radial direction for selected emission lines from different species. Each value represents the average of three positions, with error bars indicating the standard deviation. The radially symmetric spectral distribution of LIBS species is observed, centred around the plasma core. The maximum

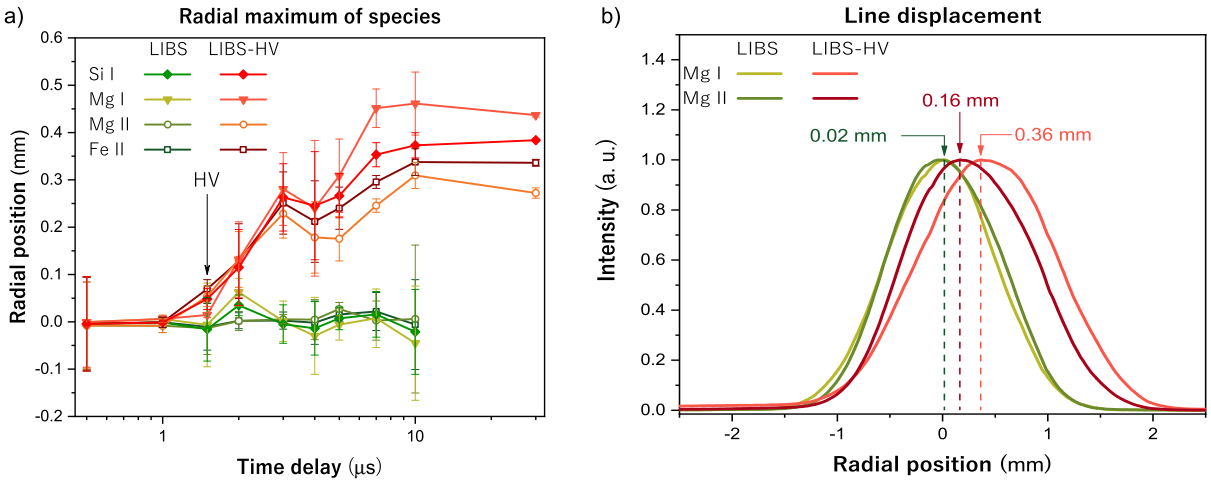

Fig. 4.20: Distribution of the species in the plasma after the HV discharge is triggered. Transitions used: Si I, 288.15 nm; Mg I, 285.21 nm; Mg II, 280.27 nm; Fe II, 275.57 nm. a) Radial distribution of the species' maximum position. Each value corresponds to the average of the maximum position of different species. Error bars correspond to the standard deviation of three measurements, except for 30 µs where only one measurement was performed. b) Line intensity for magnesium lines at 7 µs, for LIBS and LIBS with HV discharge. The intensity is normalised and the distribution is along the radial direction.

emission of both neutral and ionized species is located at around the centre of the plasma for all studied time delays

On the contrary, when the discharge is applied, two main effects are discernible. First, there is a systematic deviation of the spectral emissions from the plasma centre. In fact, the emissions shift towards the charged electrode. This displacement coincides with the first cycle of the discharge, which is apparently indicated by the direction of the initial oscillation. From Fig. 4.2, the first oscillation follows the direction from the grounded electrode to the charged one. Thus, this first period moves the plasma to the right and even if the second oscillation may move the plasma to the left side, subsequent oscillations lack the energy to return the plasma to the centre, establishing a preferential direction for the plasma's movement. This preferential direction influences both the temperature and the electron density symmetry. As depicted in Fig. 4.20a), ionic and neutral species exhibit different radial movements. In the case of ionic transitions, they remain closer to the centre than neutral transitions, which can be attributed to the fact that positive charges (ions) have the tendency to move towards the grounded electrode.

Thus, the electrical field induces a slightly polarization in the internal species of the plasma. This slight polarization, induced by the electrodes, is evident in Fig. 4.20b) showing a separation of about 0.2 mm between the ionic and neutral line profiles. The figure corresponds to magnesium transitions at 7 µs after the laser onset. The ionic and neutral lines are shown to move more than 0.3 and 0.15 mm from the centre, respectively. As a result, in HV-LIP, a low concentration of ions is observed on the right side and a low concentration of neutrals on the left side. This leads to a decrease in the calculated temperature along the radial direction (See Fig. 4.18b)). Therefore, it can be concluded that the changes in radial temperature are a consequence of the slight polarization induced by the electrodes.

The spectral analysis reveals that discharge affects symmetry in both temperature and electron density, with increased values along the radial axis. However, both electron density and

temperature experience a decrease along the radial direction, primarily due to the influence of the grounded electrode, which attracts ionic species and results in a cooler plasma on the side with the charged electrode.

4.8 Plasma parameters

In Sect. 2.1.1 the main plasma parameters were discussed. In this section, the characteristic parameters of the plasma are studied using the results obtained in temperature and electron density.

First, the parameters that allow for plasma classification were derived. The first condition arises from the Debye length. It quantifies the distance at which the plasma remains quasi-neutral and from Eq. 2.17 can by defined for electrons as

$$\lambda_D^2 = \frac{\varepsilon_0 k_B T}{N_e e^2}, \tag{4.15}$$

with N_e as the electron density, T is the plasma temperature, ε_0 is the electric permittivity of free space, e the elementary charge and k_B is Boltzmann's constant.

Then, in Eq. 2.19 the number of particles in a sphere of radius λ_D was defined as the Debye number or the plasma parameter,

$$N_D = N_e \frac{4}{3}\pi\lambda_D^3, \tag{4.16}$$

which can be used to validate that the potential energy is smaller than the thermal energy. The conditions that were obtained from these two parameters can be expressed as

$$\lambda_D \ll L \qquad \text{Debye length criterion} \tag{4.17}$$

$$N_D \gg 1 \qquad \text{Debye number criterion} \tag{4.18}$$

where L is the dimension of the plasma. From the results obtained, it is clear that the dimensions of the plasma are a few millimetres in height and width. These two criteria are taken as necessary conditions for an ideal plasma. Eq. 4.17 guarantees that the collective interactions are due to the bulk plasma and not to boundary effects. Also, Eq. 4.18 refers to a plasma in which thermal energy dominates over the potential, which is called an ideal plasma.

With the data obtained from electron density and temperature calculations, these criteria can be evaluated. To understand how each technique affects these parameters and how they evolve over time, Fig. 4.21 shows the temporally evolution of both the Debye length and the Debye number. This was calculated gathering all data obtained. Then, the average was obtained for each time delay. The figure shows also the error bars obtained from the standard deviation of the data.

As the figure shows, both parameters increase with time. From Fig. 4.21a) it is clear that the Debye length is lower than the dimensions of the plasma for several orders of magnitude. The Debye length ranges from about 12.6 to 52.4 nm. Then, it can be concluded that for the

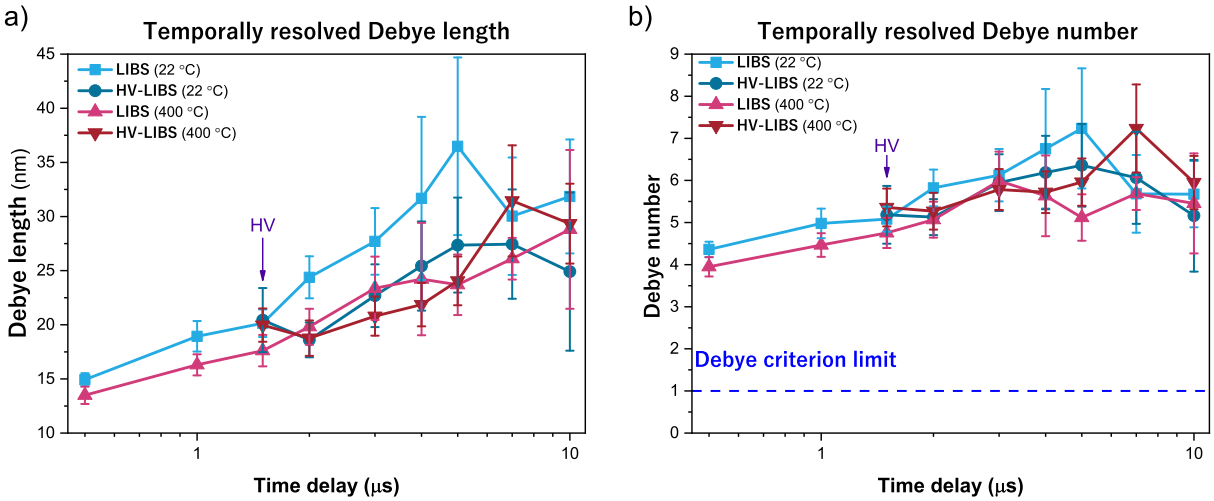

Fig. 4.21: Temporally resolved criteria of ideality based on Debye's parameters. a) Debye length b) Debye number. Each value corresponds to the average of all the data obtained at each time delay and experimental condition (LIBS and HV-LIBS at both 22 and 400 °C). The HV discharge is triggered at 1.5 µs after the onset of the laser. Error bars corresponds to the standard deviation of the data.

range of temperature and electron density obtained, the LIP can be described as quasi-neutral at distances greater than nanometres. Also, as the figure shows, the Debye length is greater in LIBS experiments performed at room temperature than those at 400 °C or with a HV discharge applied. This may suggest that both re-excitation techniques improve the quasi-neutrality of the plasma. Because if the Debye length decreases, it means that the scale at which the plasma can remain neutral is lower. However, since the plasma scale is around mm, the discussion should only conclude that the Debye criterion is fulfilled.

Similar results can be observed in Fig. 4.21b) for the plasma parameter. As the figure shows, the Debye number is of only few particles. In fact, it was obtained that it ranges from 3.6 to 10. Then, it may be suggested that the thermal interactions surpass the Coulomb ones. And hence the plasma is ideal. Also, as the plasma evolves this number slightly increases. This means that the plasma becomes more ideal as it evolves. Also, LIBS profile is slightly greater that re-excited profiles, which may indicate that the re-excitation techniques move the plasma apart of the ideality. This is because as the ionisation is greater, the Coulomb interactions increase in their importance. However, the difference given by the error bars is almost negligible. Then, this analysis can only conclude that the criterion is fulfilled by the LIP. Then, these results shown that it is indeed a plasma and satisfies the ideality criteria. Furthermore, this result can be generalised. In Sect. 2.1.1, the ideality criterion was also expressed by means of the mean distance between particles r_s, defining the parameter of ideality Γ (Eq. 2.24) as

$$\Gamma = \frac{e^2}{4\pi\varepsilon_0 r_s k_B T}. \tag{4.19}$$

This parameter can be extended to account for interactions between different species in the plasma. Supposing a mostly ionised plasma, when the main interactions are between ions and electrons, the parameter of ideality is $\Gamma_{Ze} = Z^{\frac{2}{3}}\Gamma$, with Z as the atomic number. Hence, the

ideality criterion is

$$\Gamma_{Ze} \ll 1, \qquad \text{Ideality criterion} \quad (4.20)$$

which expresses the dominance of the kinetic-thermal energy over the Coulomb interaction energy.

On the other hand, these criteria were described as valid in the case in which the subject is a classical plasma and not a quantum one. In order to suppose whether the plasma is classical it is necessary that electrons and ions are found at distances greater than the thermal electron de Broglie wavelength λ_e. If the mean energy of the interaction is $k_B T$, this condition can be written as (Eq. 2.26)

$$\lambda_e \ll \frac{Ze^2}{4\pi\varepsilon_0 k_B T}. \quad (4.21)$$

Hence, defining Q as the classicality parameter,

$$Q = \frac{Ze^2}{4\pi\varepsilon_0 \lambda_e k_B T}, \quad (4.22)$$

the condition becomes

$$Q \gg 1. \qquad \text{Classicality criterion} \quad (4.23)$$

Both the ideality and the classicality criteria were calculated with all the data obtained. Fig. 4.22 shows the temporally resolved evolution of these criteria for each technique studied. Likewise the electron density and the temperature, Γ_{Ze} and Q were calculated using magnesium transitions. The values reported correspond to the average of all the data obtained with each technique at each time delay. Error bars correspond to the standard deviation of the data.

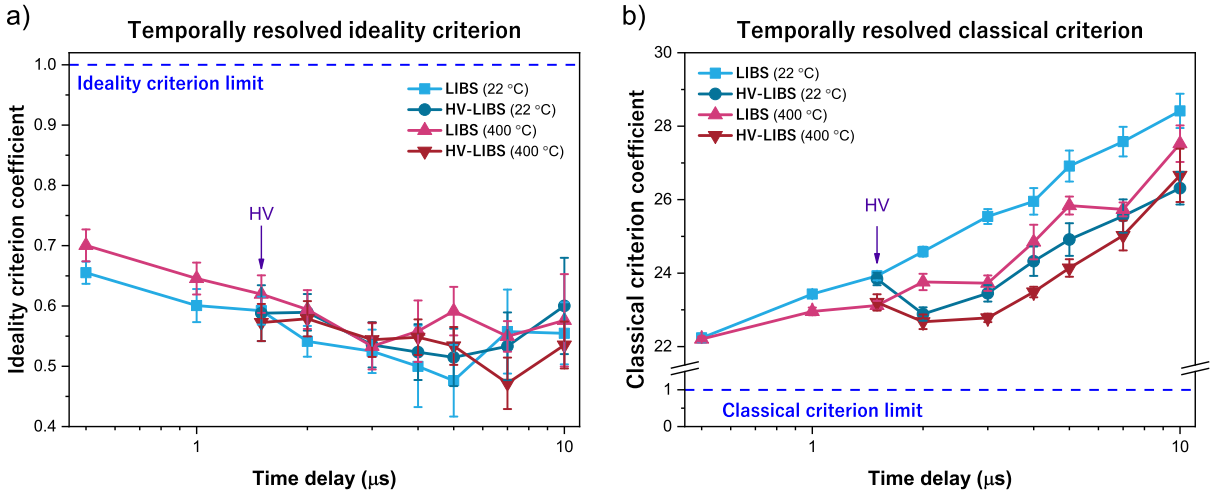

Fig. 4.22: Temporally resolved criteria for ideality and classicality. a) Ideality criterion b) Classicality criterion. Each value corresponds to the average of all the data obtained at each time delay and experimental condition (LIBS and HV-LIBS at both 22 and 400 °C). The HV discharge is triggered at 1.5 µs after the onset of the laser. Error bars corresponds to the standard deviation of the data. Magnesium was used for the calculations.

Fig. 4.22a) shows the temporally resolved evolution of Γ_{Ze}. It is clear that all the obtained values fall in the ideal region. In fact, the calculated values range from about 0.37 to 0.73, and decrease over time. This means that as the plasma evolves, it becomes "more ideal", as previously said. Likewise with the Debye criterion, LIBS is in average more ideal than the other techniques studied. Also, it should be expected that at the plasma formation, it may be approximately nonideal. This is because of the exponential growth in electron density at early times after the initial ionisation. As the plasma recombines and cools, it becomes more ideal, because the Coulomb interactions loss strength.

Fig. 4.22b) presents the temporally evolution of Q. The values obtained range from 22 to 29.4, which is above the criterion limit. Thus it can be concluded that the plasma behaves classically at all the measurements. Also, the LIBS profile increases almost exponentially. This means that as the plasma colds, it becomes more classical. This is because at early stages of the plasma formation, the density may be higher enough to have degenerated electrons. It should also be noted that as the classicality decreases with the increase in electron density, the application of the HV discharge leads to a decrease in classicality. Also, as heating the sample sustains the electron density, its plasma is slightly less classical than that at room temperature. However, it is clear that for all the data obtained the plasma behaves classically, as should be expected.

With these data, it can be concluded that, for the electron density and temperature ranges obtained, the plasma is classical and ideal. Even if these calculations suppose that the plasma has only two components, it should be expected that this result extends for the *real* plasma. Thus, the LIP behaves like a classical plasma with weak interaction of the electrons and ions [51]. Then, for this kind of plasma, it is possible to use the ideal gas theory to describe its thermodynamic state.

The thermodynamic state of the plasma was called Local Thermodynamic Equilibrium. This state was studied in Sect. 2.3.5, where it was said that if the plasma is in LTE, it is possible to use thermodynamic relations as the Boltzmann and Saha distributions. Furthermore, the calculations of the temperature were based in this supposition. Then, it is interesting to evaluate whether the obtained values satisfy the conditions for LTE. Thus, whether the components in the plasma may be in LTE.

Three conditions for LTE were described in Sect. 2.3.5. First, the McWhirter criterion which evaluates that for a stationary and homogeneous plasma, excitation and de-excitation rates are dominated by collisions rather than by radiative processes. Then, to study the non-stationary and non-homogeneous cases, it was proposed that the variation of the parameters must be small, in space and time.

The McWhirter criterion can be expressed as

$$N_e > 1.6 \times 10^{12} T^{\frac{1}{2}} \left(\Delta E_{nm}\right)^3 , \tag{4.24}$$

with N_e (cm^{-3}) the electron density, T (K) the temperature and ΔE_{nm} (eV) the energy difference between levels n and m. Then, it establishes an inferior limit for the electron density. Defining

the McWhirter criterion coefficient (MCC) as

$$MCC = \frac{N_e}{1.6 \times 10^{12} T^{\frac{1}{2}} \left(\Delta E_{nm}\right)^3}, \tag{4.25}$$

the first condition for LTE can be written as

$$MCC > 1. \qquad \text{McWhirter Criterion} \tag{4.26}$$

This criterion was evaluated for all the obtained data. As LTE is of main importance, its fulfilment was investigated across each of the three sections of the experimental work. Each measurement involves three parameters: the experimental technique, the time delay from the onset of the laser, and the spatial position of the measurement. Fig. 4.23 illustrates a statistical comparison of the McWhirter criterion in four different perspectives. Firstly, for each re-excitation technique; secondly, for each time delay; and finally, for each of the investigated spatial directions. Each graph consists of a series of boxplot graphs of all the MCC obtained with all the data[4]. The central line corresponds to the mean value, and the whiskers extend to the 5-95% percentile range of the data. The box encapsulates the percentiles 25 to 75. Also, the limit of the McWhirter criterion is signalled by a blue line. As is observed, all the data fall above this line and then agree with the McWhirter criterion. In summary, Fig. 4.23a) and Fig. 4.23b) have the same data, but classified by experiment or time delay; respectively. And then in Fig. 4.23c) and 4.23d) the same data is classified by spatial direction. The element evaluated is the transition 285.2127 nm ($3s3p \longrightarrow 2p^6 3s^2$) of Mg I, the same transition used to calculate the electron density, which has a ΔE_{nm} of 4.3458029 eV [79].

In Fig. 4.23a), the values for MCC are classified by experiment. The values range from 1.28 to 27.4, which implies that all measurements may be in LTE. As the figure shows, there is no significant difference between the different experimental configurations. Thus, the application of a HV discharge to the plasma or its formation in a heated sample has little effect in its equilibrium state. However, for measurements with HV discharge, the whiskers are shorter than in LIBS case. This is because, as Fig. 4.23b) shows, lower delays have a greater MCC and HV experiments start at 1.5 µs after the laser onset. Also, from Fig. 4.23b) it is clear that the extremal values of MCC correspond to extremal time delays, thus the upper outliers in Fig. 4.23a) correspond to short delays and the lower outliers to longer delays. On the other hand, from Fig. 4.23c) there are three main observations. First, along the radial direction there is not significant differences in the equilibrium state of the plasma. Second, the range of the data in each position almost covers the total range. This is an indication that, at each radial position, most of the values for MCC are reached at some delay or experiment. Third, that as LIBS experiments span up to 0.9 mm along the radial direction, only HV measurements are shown for 1.2 and 1.5 mm. Then, these values seem lower, because at these positions only delays of 1.5 µs are reported. This has an interesting implication that temporal changes in MCC are more important than spatial or experimental changes. Similar results are observed in Fig. 4.23d) for the vertical direction. In general, the state of equilibrium has no significant change along the spatial position in the plasma. The delay from the laser onset is the main cause of the changes in the state of equilibrium. This

[4]This refers to, effectively, all the data. THe objective is to show that there is no significant difference between techniques or spatial positions. However, there is a significant difference only when the data is classified by acquisition time.

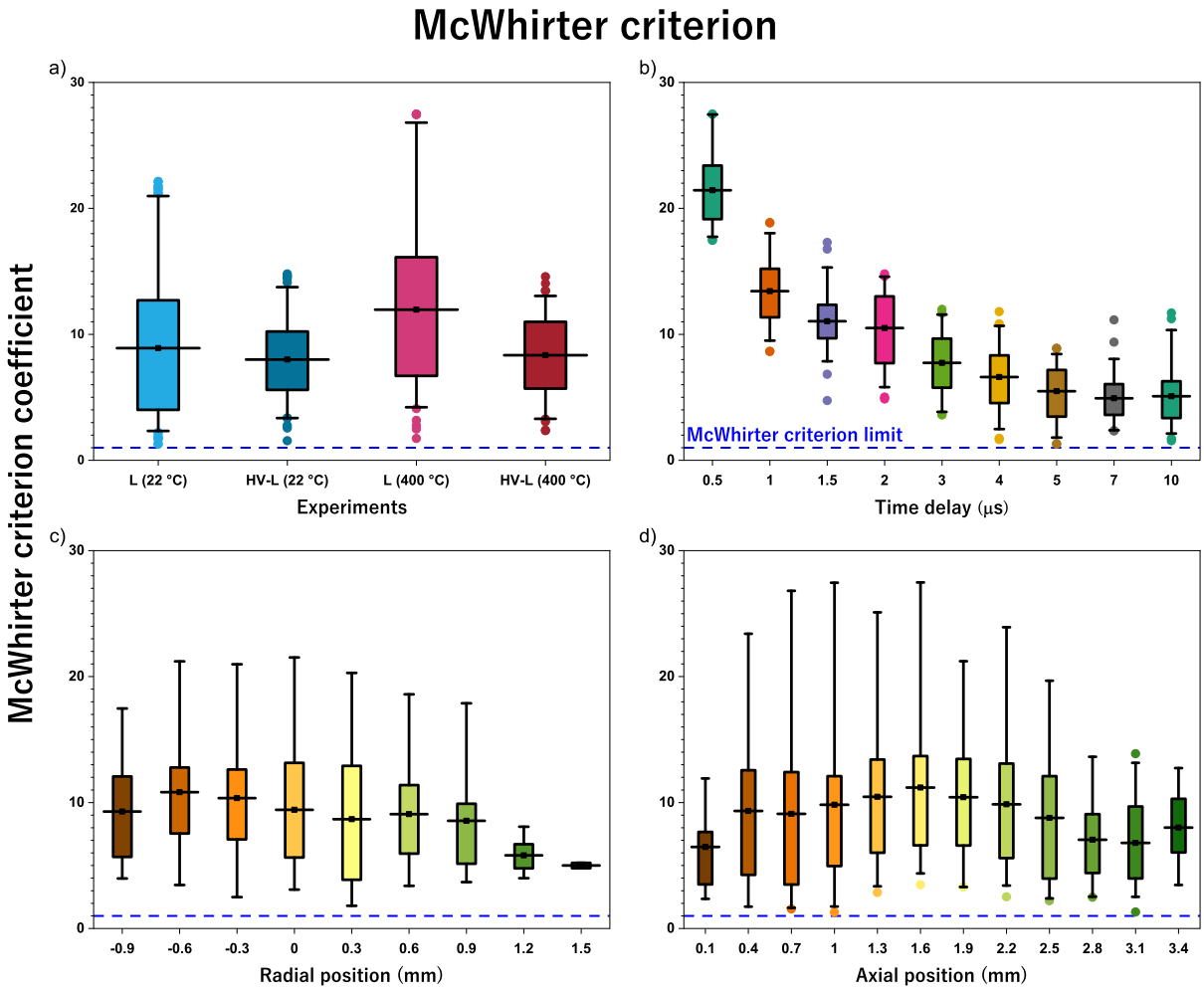

Fig. 4.23: Statistical representation of the McWhirter criterion. All the data are classified across the three parameters: Experiment, time delay, and spatial position. a) Data classified by experiment: L for LIBS and HV-L for LIBS assisted with HV discharge, and in parentheses is indicated the sample temperature. b) Data classified by time delay c) Data obtained along the radial direction, classified by position d) Data obtained along the axial direction, classified by position. Data above the blue line (MCC=1) satisfies the McWhirter criterion. Each box encapsulates the percentiles from 25 to 75, the central line corresponds to the mean, and the whiskers extend to the 5-95% percentile range of the data.

conclusion can also be obtained by a comparison of the whiskers. Temporal boxplots have shorter whiskers than the spatial or experimental ones. This implies that the best classification for the data is the temporal classification.

In order to clarify how each technique changes the sate of equilibrium, Fig. 4.24 shows the temporally resolved results for MCC. Each value corresponds to the average of all the data for the corresponding experiment and delay. Error bars were obtained from the standard deviation of the data.

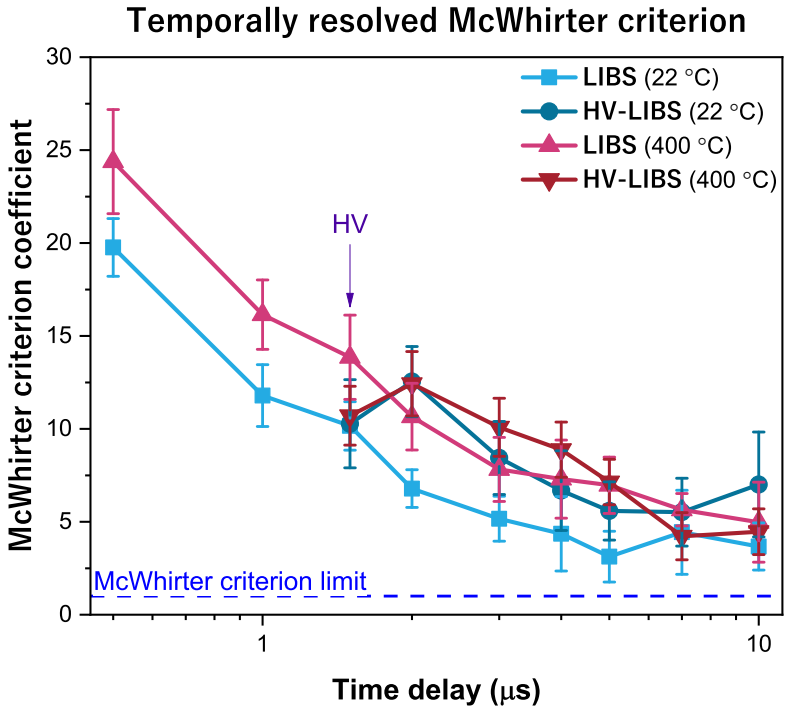

Fig. 4.24: Temporally resolved McWhirter criterion coefficient. Each value corresponds to the average of all the data obtained at each time delay and experimental condition (LIBS and HV-LIBS at 22 and 400 °C). The HV discharge is triggered at 1.5 µs after the onset of the laser. Error bars corresponds to the standard deviation of the data. Magnesium was used for the calculations.

Fig. 4.24 confirms that there is significant change in the equilibrium state of the plasma with the time delay. In general, as the plasma undergoes cooling, it departs from LTE. Moreover, the figure suggests that the re-excitation techniques contribute to sustaining the equilibrium state of the plasma for longer times. Although it was initially hypothesised that the application of the HV discharge might shift the plasma from LTE, its re-excitation effect appears to maintain equilibrium. However, in all cases, it is clear that the plasma deviates from LTE. Among the studied experimental configurations (only LIBS, HV-LIBS, varied sample temperatures, different spatial positions, and acquisition times), it can be concluded that what most affects the equilibrium state of the plasma is its temporal evolution.

Furthermore, the observed increase in error bars for temperature and electron density over time can be attributed to the plasma departing from LTE with time, causing deviations from Boltzmann statistics. This departure from equilibrium leads to a decrease in the repeatability of the calculations. However, this does not fully explain the observed increase in error bars when

re-excitation techniques are applied. To address this, consider Fig. 4.7, which illustrates the turbulence induced in the plasma during re-excitation. The plasma's inherent instability may result in variations between successive measurements. As each measurement comprises multiple shots and acquisitions, the differing nature of each re-excited plasma instance contributes to reduced precision in the collected radiation data.

The other two conditions studied correspond to the spatial and temporal gradients in the plasma. In the case of the temporal changes in the parameters of the plasma, it was requested that (Eqs. 2.109):

$$1 \gg \left| \frac{T(t+\tau_{rel}) - T(t)}{T(t)} \right| \qquad \text{Temporal criterion for T} \quad (4.27)$$

$$1 \gg \left| \frac{N_e(t+\tau_{rel}) - N_e(t)}{N_e(t)} \right|. \qquad \text{Temporal criterion for } N_e \quad (4.28)$$

These criteria correspond to ask for the plasma to transit a sequence of quasi-stationary near LTE states. And therefore, it should establish LTE in a time within the order of the relaxation time, defined as

$$\tau_{rel} = \frac{6.3 \times 10^4}{N_e f_{mn} \langle g \rangle} \Delta E_{nm} \, (k_B T)^{\frac{1}{2}} \exp\left(\frac{\Delta E_{nm}}{k_B T}\right), \quad (4.29)$$

where $\langle g \rangle$ is the gaunt factor, and f_{mn} is the transition strength. The gaunt factor for the Mg I transition was estimated of about 0.04 with Ref. [65] and the transition strength, of 1.8, was extracted from the NIST database [79]. With these data it was possible to calculate the relaxation time for all the values of temperature and electron density obtained.

On the other hand, in the case of inhomogeneous plasmas, the spatial gradients should be addressed. In Sect. 2.3.5 it was explained that if the spatial gradients are significant, the atoms cannot be described by the local values of temperature and electron density. This criteria was expressed as (Eq. 2.113)

$$1 \gg \left| \frac{T(x) - T(x+\lambda_d)}{T(x)} \right| \qquad \text{Spatial criterion for T} \quad (4.30)$$

$$1 \gg \left| \frac{N_e(x) - N_e(x+\lambda_d)}{N_e(x)} \right|. \qquad \text{Spatial criterion for } N_e \quad (4.31)$$

where the diffusion length was approximated as

$$\lambda_d \approx 1.4 \times 10^{12} \frac{(k_B T)^{\frac{3}{4}}}{N_e} \left(\frac{\Delta E_{nm}}{M_A f_{mn} \langle g \rangle} \right)^{\frac{1}{2}} \exp\left(\frac{\Delta E}{2 k_B T}\right), \quad (4.32)$$

and M_A is the atomic mass. Then, the diffusion length was calculated for all the data obtained.

Fig. 4.25 displays the temporally resolved results for the relaxation time and diffusion length. The transition used is Mg I, as in the previous results. Each value represents the average of all data obtained at that delay and experimental condition. The error bars indicate the standard deviation of the data.

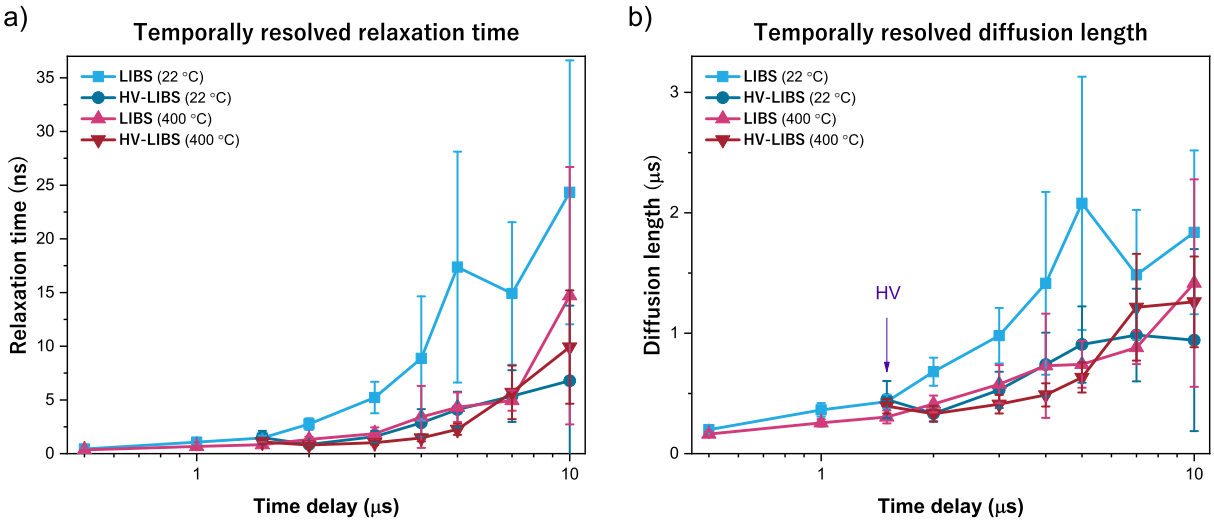

Fig. 4.25: Temporally resolved criteria for a) relaxation time b) diffusion length. Each value corresponds to the average of all the data obtained at each time delay and experimental condition (LIBS and HV-LIBS at both 22 and 400 °C). The HV discharge is triggered at 1.5 µs after the onset of the laser. Error bars correspond to the standard deviation of the data. Magnesium was used for the calculations.

As Fig. 4.25a) shows, the relaxation time is on the order of nanoseconds, ranging from 0.3 to 50 ns. This is lower than the acquisition width (with a minimum width of 100 ns) and the temporal difference between delays. Therefore, it is clear that the plasma can reach relaxation while the camera is acquiring the spectra. Additionally, from one time delay to another, the plasma will be relaxed. Thus, the temporal criteria for T and N_e (Eq. 4.27 and 4.28, respectively) are easily satisfied because $T(t+\tau_{rel}) - T(t) \geq T(t)$ implies that the temperature decreases by half along t_{rel}. However, between 0.5 and 10 µs the temperature generally changes by about 50%. On the other hand, the electron density has a higher rate of change but requires at least 0.5 µs to decrease by half. Furthermore, due to the decreasing rate in both electron density and temperature, it should be expected that in the first nanoseconds after the initial ionisation, the plasma may be far from LTE. Nevertheless, within the typical temporal width used in LIBS, the rate of change of the plasma parameters is significantly slow to be out of LTE.

Regarding the spatial gradients, Fig. 4.25b) shows the temporally resolved evolution of the diffusion length, which is in a range from 0.14 to 4.32 µm. In Ref. [65] there are two ways of analysing the diffusion length. First, the spatial criteria in Eq. 4.30 and 4.31. Second, by a comparison of λ_d to the characteristic variation in the plasma. In the first case, the change in temperature must satisfy $T(x) - T(x+\lambda_d) \ll T(x)$. However, both electron density and temperature are almost constant along both axes. The most significant changes occur in the radial axis when the HV discharge is applied. For example, between -0.6 and 1.5 mm there is a change in temperature of less than 20 %, at 4 and 5 µs after the laser onset. On the other hand, the electron density requires almost 1 mm to decrease by half in the radial direction when the discharge was applied. In the second case, the LTE criterion is expressed as $d_p > 10\lambda$, where d_p is the characteristic variation length in the plasma. It can be taken as the plasma diameter, which is in the order of mm. Also, can be approximated as [65]

$$d_p \approx T(x)\left(\frac{\mathrm{d}T(x)}{\mathrm{d}x}\right)^{-1}. \tag{4.33}$$

In this case, d_p ranges from 20 to 140 mm for the radial profile of HV-LIBS at 5 µs after the laser onset. Therefore, it can be concluded that the spatial gradients in the plasma are negligible and do not affect its LTE condition.

In this section the data obtained was applied for the estimation of some of the plasma parameters. In particular, these are related to its state of equilibrium and to analyse whether it is a classical and ideal plasma. The ideality criteria studied the capacity of the plasma to sustain its quasineutrality and whether the thermal energy dominates over the Coulomb interactions. It was found that the plasma maintains its ideality and classicality even when the re-excitation techniques are applied, at all spatial positions and time delays studied. Moreover, the re-excitation techniques enhance the ionisation and help the plasma to enhance these two characteristics. Also, the LTE state was studied. Plasma was found to satisfy the McWhirter criterion at all of the measurements performed. Also, the temporal and spatial gradients in electron density an temperature were found to be negligible to cause an alteration of the LTE state of the plasma. Moreover, the re-excitation techniques, due to increase in ionisation, help the plasma to sustain its equilibrium state. In conclusion, the plasma may be in LTE along all the positions and times studied. Also, this is independent of the sample temperature and the hv discharge. Nevertheless, it should be remembered that the use of the Saha-Boltzmann equation assumes that the plasma is in LTE. Then, the calculations presented in this section only are intended to show that the typical electron density and temperature in LIBS plasma are in agreement with the models used. Also, a presentation of the statistical classification of all the data analogous to Fig. 4.23 is presented in Apendix A. These results show the plasma properties and characteristics do not have a significantly changes by spatial position or experiment. Thus, the main variations of the plasma are due its temporal evolution.

In summary, in this thesis the laser-induced plasma from laser-induced breakdown spectroscopy was studied. In particular, the case in which a high-voltage discharge is applied to the plasma; proposed as an enhancement technique. In addition, the variations with two sample temperatures (room temperature and 400 °C) were addressed. This change in sample temperature was also proposed as an enhancement technique. The results of the morphology study, by fast photography, illustrated the plasma expansion. The plasma was shown to expand and divide. However, the heating system may enhance the internal energy to reduce this effect. On the other hand, the HV discharge induces severe turbulence that accelerates the splitting process. The plasma was characterised by its electron temperature and electron density. The electron density was calculated from the Stark broadening and the temperature by means of the Saha-Boltzmann plot. It was found that the main effect of the discharge is to induce a slight polarisation, which leads to a temperature gradient along the radial direction. In the axial direction, it was found that the plasma is approximately symmetric. Finally, with the calculated values for electron density and temperature, the state of ideality and classicality in the plasma was studied. It was concluded that at all the time delays and position the plasma is ideal and classic, which satisfies the hypothesis used to model it as an ideal gas. Also, its thermodynamic equilibrium was addressed by means of the McWhirter criterion and the study of the temporal and spatial gradients in temperature and electron density. It was concluded that the plasma may be in LTE at all the spatial positions and delays. Also, that the re-excitation techniques enhance the possibility of LTE. Finally, it was concluded that the main effect that departs the plasma from LTE is its temporal evolution.

Conclusions

In this work, the laser-induced plasma (LIP) obtained in laser-induced breakdown spectroscopy (LIBS) was studied. LIBS was presented as a spectroscopic technique for elemental identification. As a improvement, two enhancement techniques were applied. The main enhancement technique consisted of applying a high-voltage discharge to the LIP. This was also carried out when the sample was kept at high temperature, which was the second enhancement technique. The LIP was induced on the surface of loam soil samples. Loam soils are mainly useful in agriculture and typically have elements as silicon, magnesium, iron, manganese, oxygen, etc. This work was focused on its application in the the search for contaminants in soils.

To ablate the target, an infrared laser was used. The LIP spectral emission was collected with spatial and temporal resolution using two different optical arrangements: one to collect the emission along the vertical (axial) direction and the other to collect it along the horizontal (radial) direction. With this, it was possible to study the plasma with spatial resolution along both axes. Also, this was performed at several time delays from the laser onset.

The discharge, consisting of an oscillatory pulse applied via a spark-gap between two electrodes, delivered 250 mJ to the plasma over a duration of 10 µs. In heating experiments, a bulb lamp elevated the temperature of a steel plate to 400 °C, with the sample placed on top of this plate. The study of plasma morphology and evolution employed fast photography, where the camera directly collected the plasma emission. This approach was applied to each of the four possible combinations of the enhancement techniques. Spectroscopic analysis was conducted in both axial and radial directions for the LIP enhanced by HV discharge, and exclusively in the axial direction for the LIP induced on the heated sample. Parameters studied included electron density and plasma temperature, obtained through Stark broadening and the Saha-Boltzmann equation, respectively, under the Local Thermodynamic Equilibrium (LTE) model.

From the procedures and the analysis described above, the main results can be summarized as follows.

A LIP exhibits a characteristic expansion over time, with its emission area initially increasing and then decreasing at longer delays. This behaviour is more pronounced when the plasma tends to break apart at longer delays. However, when the sample is heated, a balance between external and internal pressure mechanisms contributes to preserving the plasma structure. On the other hand, the application of the HV discharge induces turbulence and significantly enhances plasma expansion and decomposition. When the discharge is applied at high sample temperatures, there is a noticeable acceleration in the axial expansion of the plasma.

It was shown that LIBS emission is strongly dependent on the electron density and the electron temperature. Generally, an increase in these parameters correlates with enhanced LIBS emission. This relationship shows the critical role that plasma conditions play the spectroscopic results in LIBS experiments.

LIBS plasma is symmetric in temperature and density. This is in both the axial and radial axes. The electron density decreases nearly exponentially in the first microseconds after the laser onset, and then it slows its decreasing rate. However, the temperature decreases exponentially along the measured temporal range.

Heating the sample increases both the plasma density and temperature. It was found that these changes are uniform along the axial direction. Also, an increased plasma lifetime was found in the heating experiments. This later result was attributed to changes in pressure and density in the surrounding air.

The application of the HV discharge to the LIP increases both its electron density and its temperature. These changes are uniform along the axial direction. However, in the radial direction it was observed a higher increase in both parameters at the side of the grounded electrode, compared to the side of the charged electrode. This lead to a decrease in electron density in temperature along the radial direction. Also, it was observed that the plasma species shift towards the charged electrode, effect attributed to a push by the discharge in its first oscillation. Also, there was found a slightly polarization in the plasma. The ionic species move less than the neutral species. This was attributed to the electric field from the electrodes. Thus, This polarization should be responsible for the asymmetry in the radial temperature.

The changes from both enhancement techniques are kept when both are simultaneously applied. However, the effects do not add linearly. Also, the error associated with the calculations increases significantly. It was observed that the heating system affects how the discharge propagates. The air becomes favourable for the discharge when its temperature increases.

The values obtained for both temperature and electron density correspond to a classical and ideal plasma with weak electron-ion interactions. Also, the LTE model was evaluated via the McWhirter criterion, a spatial criterion and a temporal criterion. All the criteria evaluated was fulfilled by the plasma parameters obtained. Also, it was found that there is no significant difference between a LIBS plasma, a HV-LIBS plasma and a LIBS plasma induced in a heated sample. The temporal evolution is the main process that departs the plasma from LTE.

Future work

The analysis of data obtained from heated samples was considerably limited, focusing mainly on spectral data for calculating electron density and plasma temperature. However, in order to discuss how the sample temperature affected the ablation efficiency, it was supposed that the target physical properties (e.g. reflectivity, thermal conductivity absorption) did not change with temperature. This is, generally, not true. Then, To comprehensively understand how sample temperature influences ablation efficiency, further investigations should consider the

temperature-dependent changes in target physical properties. Also, further studies should focus in studying the expansion of the plasma with different sample temperatures.

The application of the HV discharge was performed via two electrodes. However, their positions in relation to the plasma were arbitrary.Exploring the impact of electrode placement on the discharge trajectory and its effects on the results could be an interesting future research. However, as observed in Fig. 4.7, changes in trajectory occurred when the system was heated, so It is improbable that the position becomes significant to the results.

Furthermore, the Saha-Boltzmann method requires the use of ionic and neutral species of an element. In contrast, the multi-elemental version of this method can use transitions from different elements. In this work, the multi-elemental Saha-Boltzmann method was not implemented due to the lack of knowledge of the stoichiometry of the ablation. Although the concentrations of the major elements are known, it was not clear if they will be the same in the plasma, at all times and at all positions. Understanding the concentrations of major elements in the plasma at different times and positions would be crucial for accurate implementation for complex samples. This can be carried out by a study of the species distributions, likewise Fig. 4.20a) or by means of filters. A multi-elemental Saha-Boltzmann method should improve the temperature calculations and provide clearer temperature profiles.

Although the spatial description of the plasma found it to be approximately uniform regarding temperature and electron density, it was clear that at the edges the behaviour is different. Most of the figures -and the literature- suggest that the parameters decrease near the edges. This is due to collisional and radiative interactions with the atmosphere. Improving the collection of radiation from the edges, potentially through increased resolution and a complete spatial scan using a translation stage, would enhance the overall spatial understanding of the plasma. Also, a complete spatial scan should be possible by locating the plasma on a xyz translation stage.

The most relevant result in this work is the temperature gradient along the radial axis, which was attributed to a slightly polarization in the plasma. Also, the plasma was found to move towards the charged electrode. This key finding raises several questions that merit further investigation. First, it is not clear why the plasma moves towards that direction. Investigating how the movement changes if the polarity of the HV supply is reversed could provide information about the physics behind the HV intensification. Understanding why the plasma moves in a specific direction and exploring the relationship between current oscillations and species movement requires increased temporal and spatial resolution.

Lastly, the results concerning the LTE state could be extended by broadening the temporal range of measurements. Examining the period from the laser onset to the point at which LTE can be assumed, as well as determining the duration for which LTE remains valid, would provide valuable insights.

Appendix A

Plasma parameters

In this section, the statistical classification of all the parameters discussed in Sect. 4.8 is presented. For each parameter, the classification is organised by experiment, time delay, and spatial position.

Each figure comprises a series of boxplot graphs for all the data, with the central line representing the mean value and the whiskers extending to the 5-95% percentile range. The box encapsulates percentiles 25 to 75. A blue line indicates the limit of the corresponding criteria. All data conform to the respective criteria. Subfigures a) and b) classify the same data by experiment or time delay, respectively. Subfigures c) and d) categorize the data by spatial direction. The evaluated element is the transition at 285.2127 nm ($3s3p \longrightarrow 2p^6 3s^2$) of Mg I.

Fig. A.1 illustrates the Debye length, Fig. A.2 displays the Debye number, Fig. A.3 exhibits the ideality criterion, Fig. A.4 presents the classicality criterion, Fig. A.5 shows the relaxation time, and Fig. A.6 illustrates the diffusion length.

Similarly to Fig. 4.23, these figures show that the plasma undergoes minimal changes with spatial position or the experimental technique used. The main variations arise from its temporal evolution. Therefore, the most insightful classification for the data is by time delay.

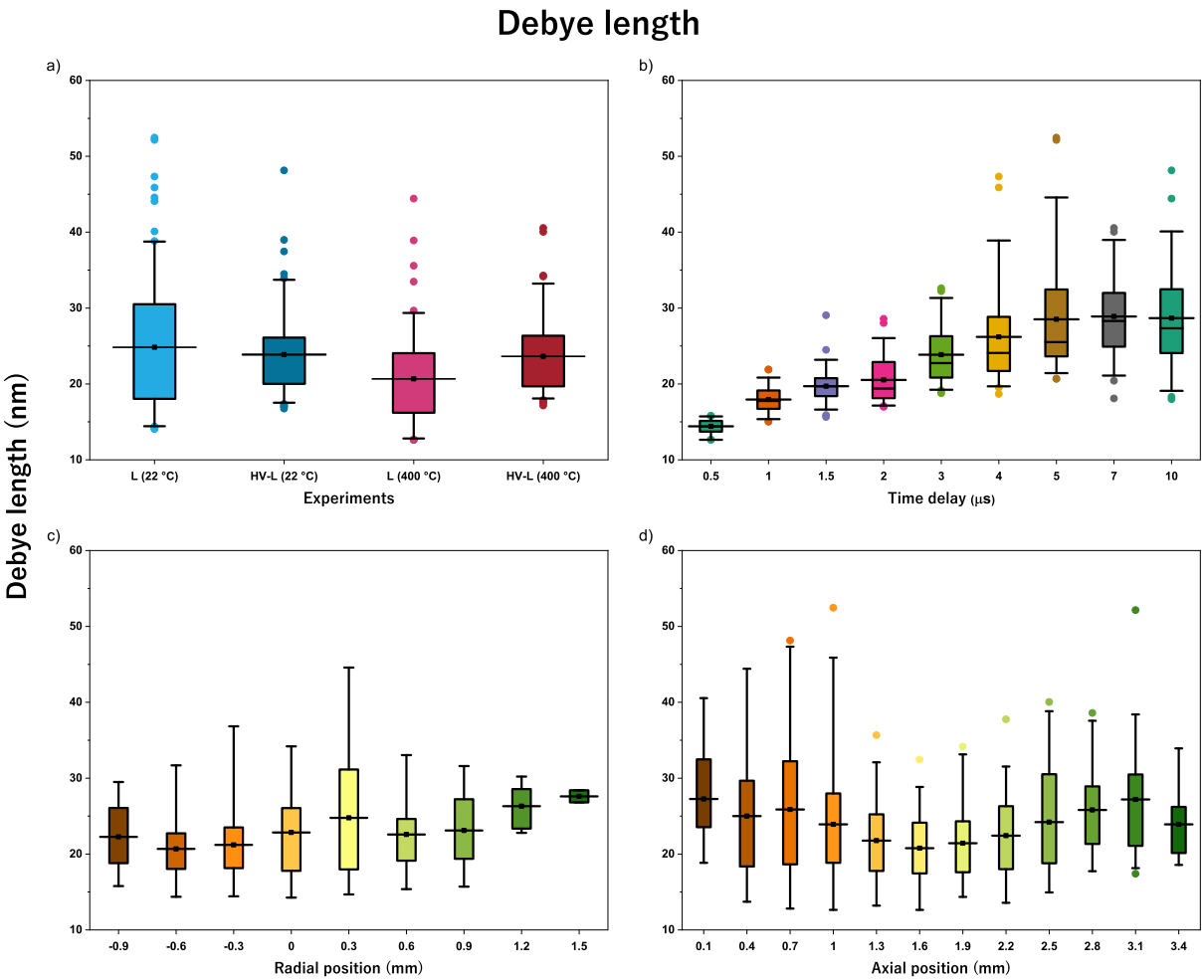

Fig. A.1: Statistical representation of the Debye length. All the data are classified across the three parameters: Experiment, time delay, and spatial position. a) Data classified by experiment: L for LIBS and HV-L for LIBS assisted with HV discharge, and in parentheses, the sample temperature is indicated. b) Data classified by time delay; c) Data obtained along the radial direction, classified by position; d) Data obtained along the axial direction, classified by position. Each box encapsulates the percentiles from 25 to 75, the central line corresponds to the mean, and the whiskers extend to the 5-95% percentile range of the data.

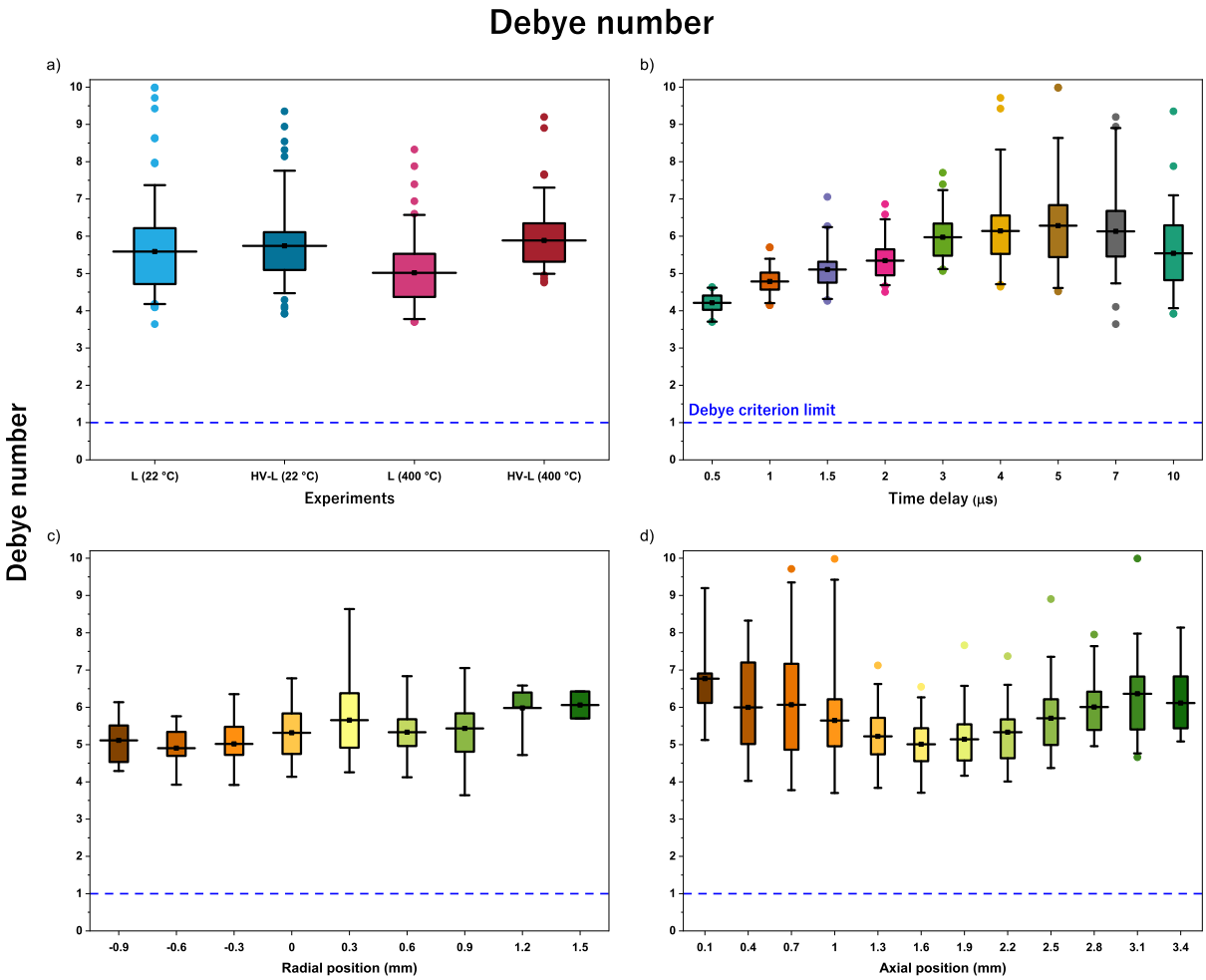

Fig. A.2: Statistical representation of the Debye number criterion. All the data are classified across the three parameters: Experiment, time delay, and spatial position. a) Data classified by experiment: L for LIBS and HV-L for LIBS assisted with HV discharge, and in parentheses, the sample temperature is indicated. b) Data classified by time delay; c) Data obtained along the radial direction, classified by position; d) Data obtained along the axial direction, classified by position. Data above the blue line (N_D=1) satisfies the Debye number ideality criterion. Each box encapsulates the percentiles from 25 to 75, the central line corresponds to the mean, and the whiskers extend to the 5-95% percentile range of the data.

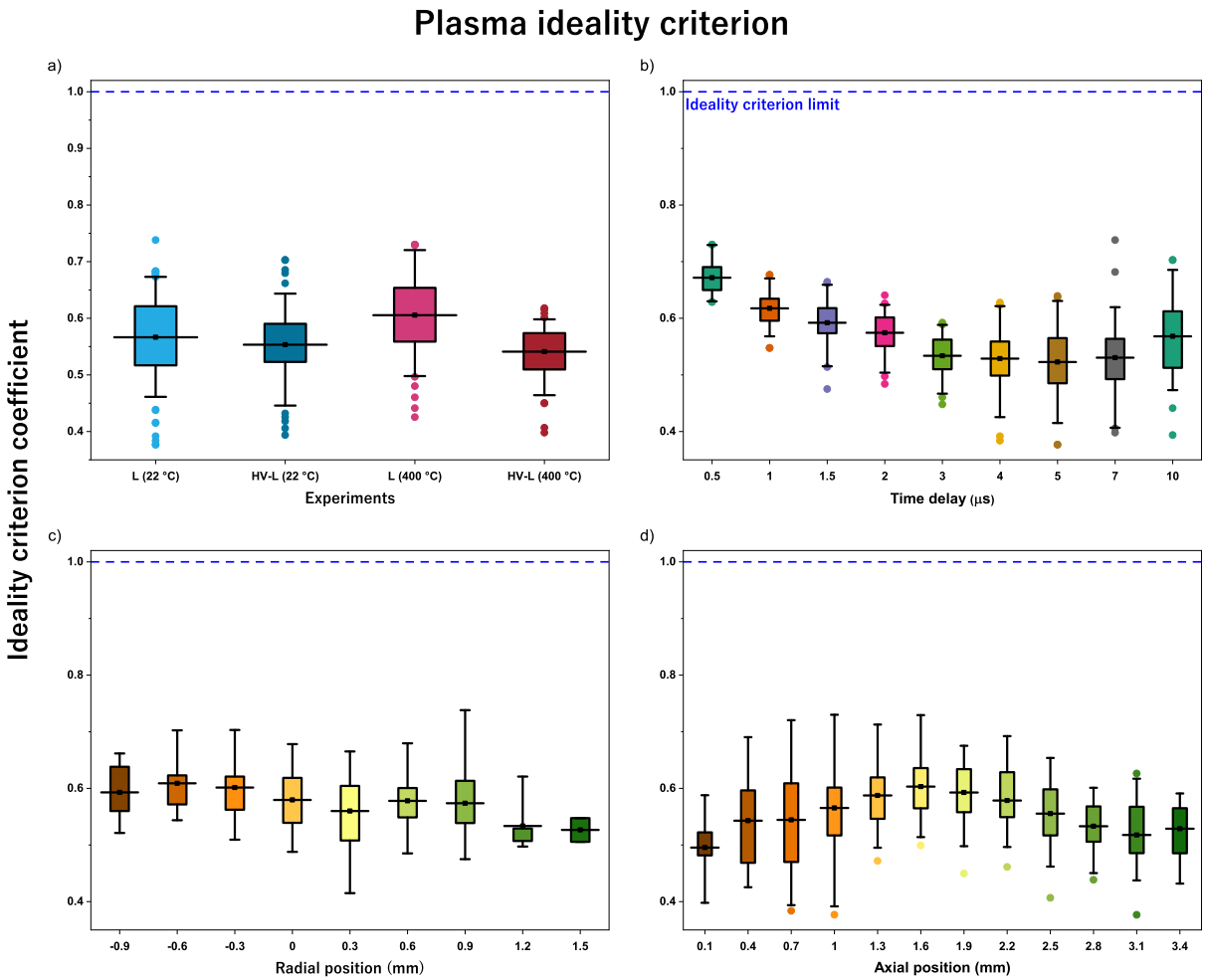

Fig. A.3: Statistical representation of the ideality criterion. All the data are classified across the three parameters: Experiment, time delay, and spatial position. a) Data classified by experiment: L for LIBS and HV-L for LIBS assisted with HV discharge, and in parentheses, the sample temperature is indicated. b) Data classified by time delay; c) Data obtained along the radial direction, classified by position; d) Data obtained along the axial direction, classified by position. Data under the blue line (Γ_{Ze}=1) satisfies the ideality criterion. Each box encapsulates the percentiles from 25 to 75, the central line corresponds to the mean, and the whiskers extend to the 5-95% percentile range of the data.

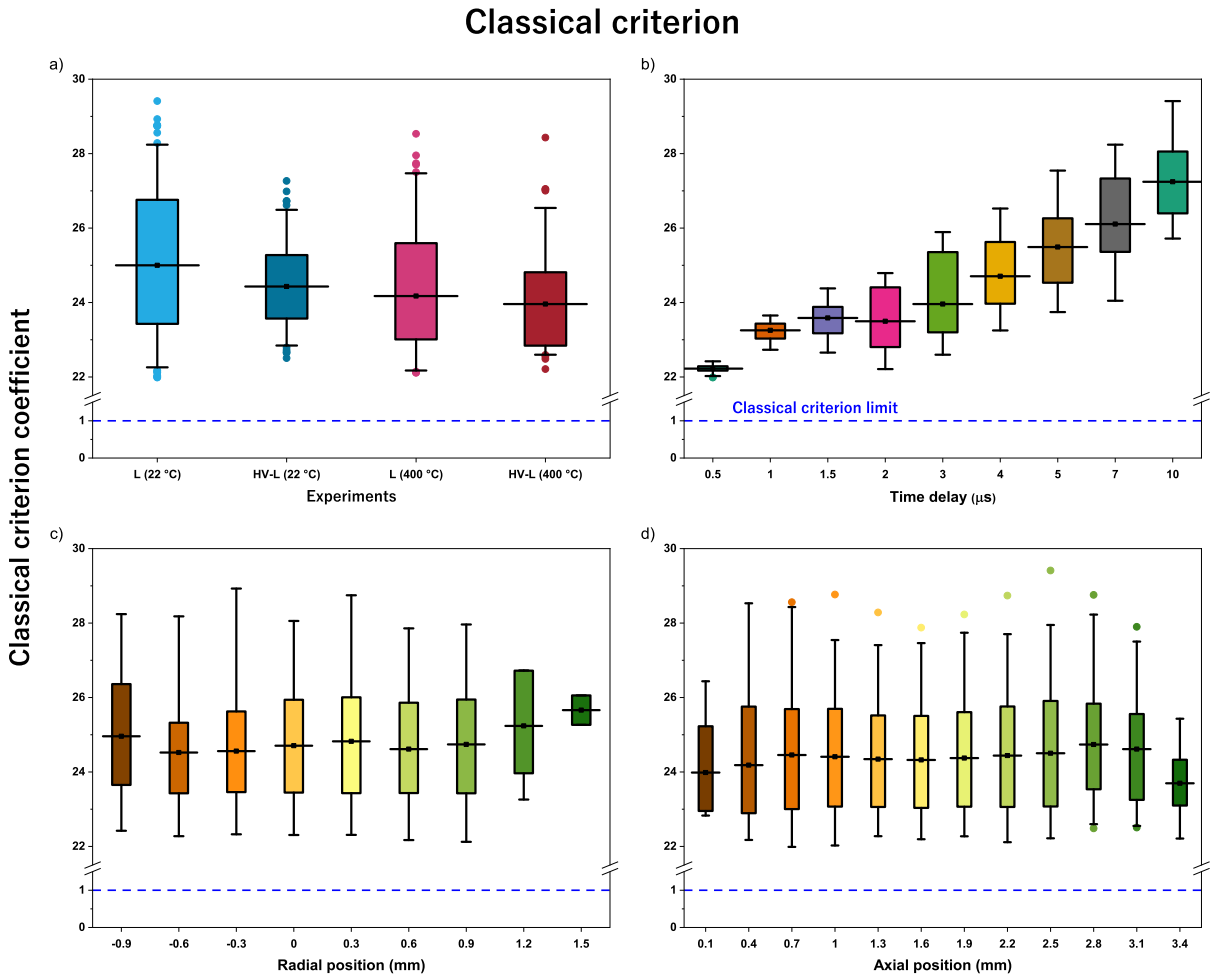

Fig. A.4: Statistical representation of the classicality criterion. All the data are classified across the three parameters: Experiment, time delay, and spatial position. a) Data classified by experiment: L for LIBS and HV-L for LIBS assisted with HV discharge, and in parentheses, the sample temperature is indicated. b) Data classified by time delay; c) Data obtained along the radial direction, classified by position; d) Data obtained along the axial direction, classified by position. Data above the blue line (Q=1) satisfies the Classical criterion. Each box encapsulates the percentiles from 25 to 75, the central line corresponds to the mean, and the whiskers extend to the 5-95% percentile range of the data.

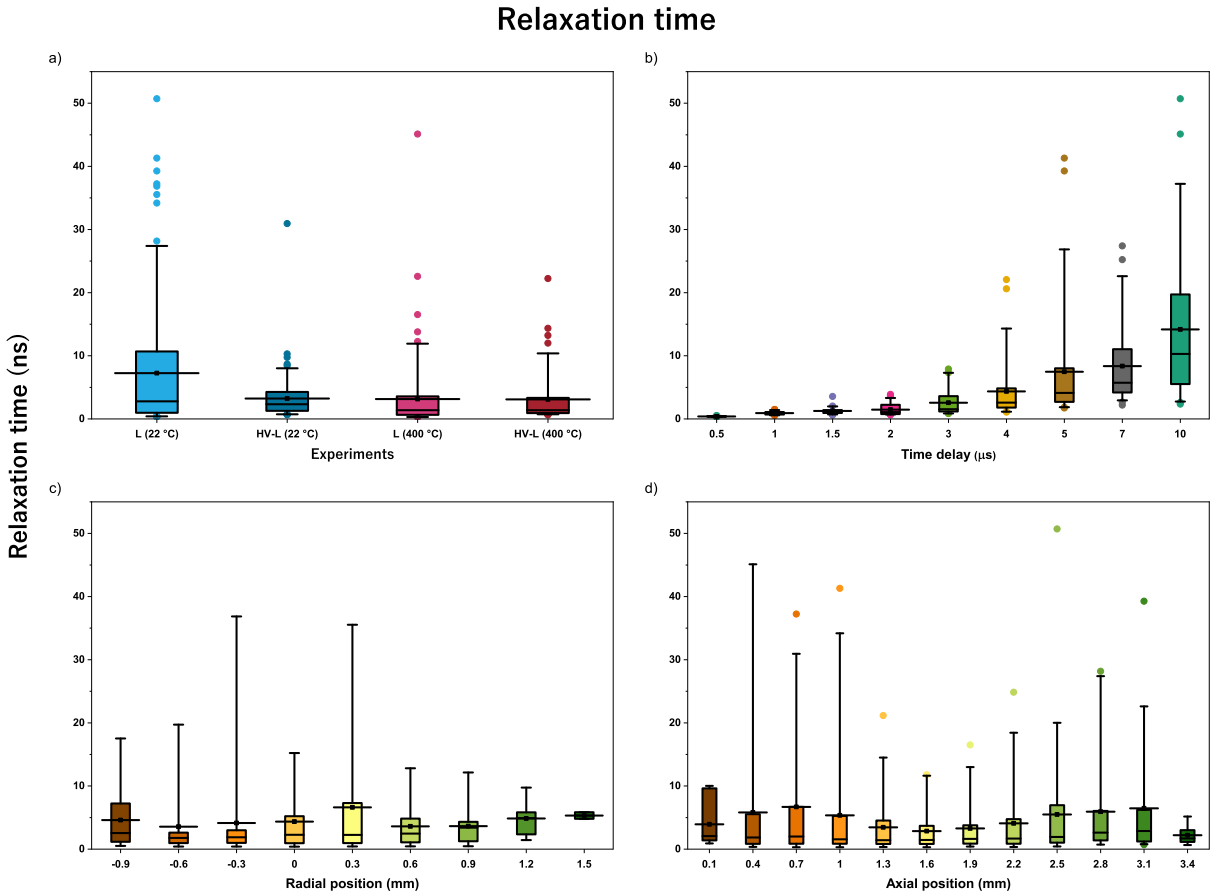

Fig. A.5: Statistical representation of the relaxation time. All the data are classified across the three parameters: Experiment, time delay, and spatial position. a) Data classified by experiment: L for LIBS and HV-L for LIBS assisted with HV discharge, and in parentheses, the sample temperature is indicated. b) Data classified by time delay; c) Data obtained along the radial direction, classified by position; d) Data obtained along the axial direction, classified by position. Each box encapsulates the percentiles from 25 to 75, the central line corresponds to the mean, and the whiskers extend to the 5-95% percentile range of the data.

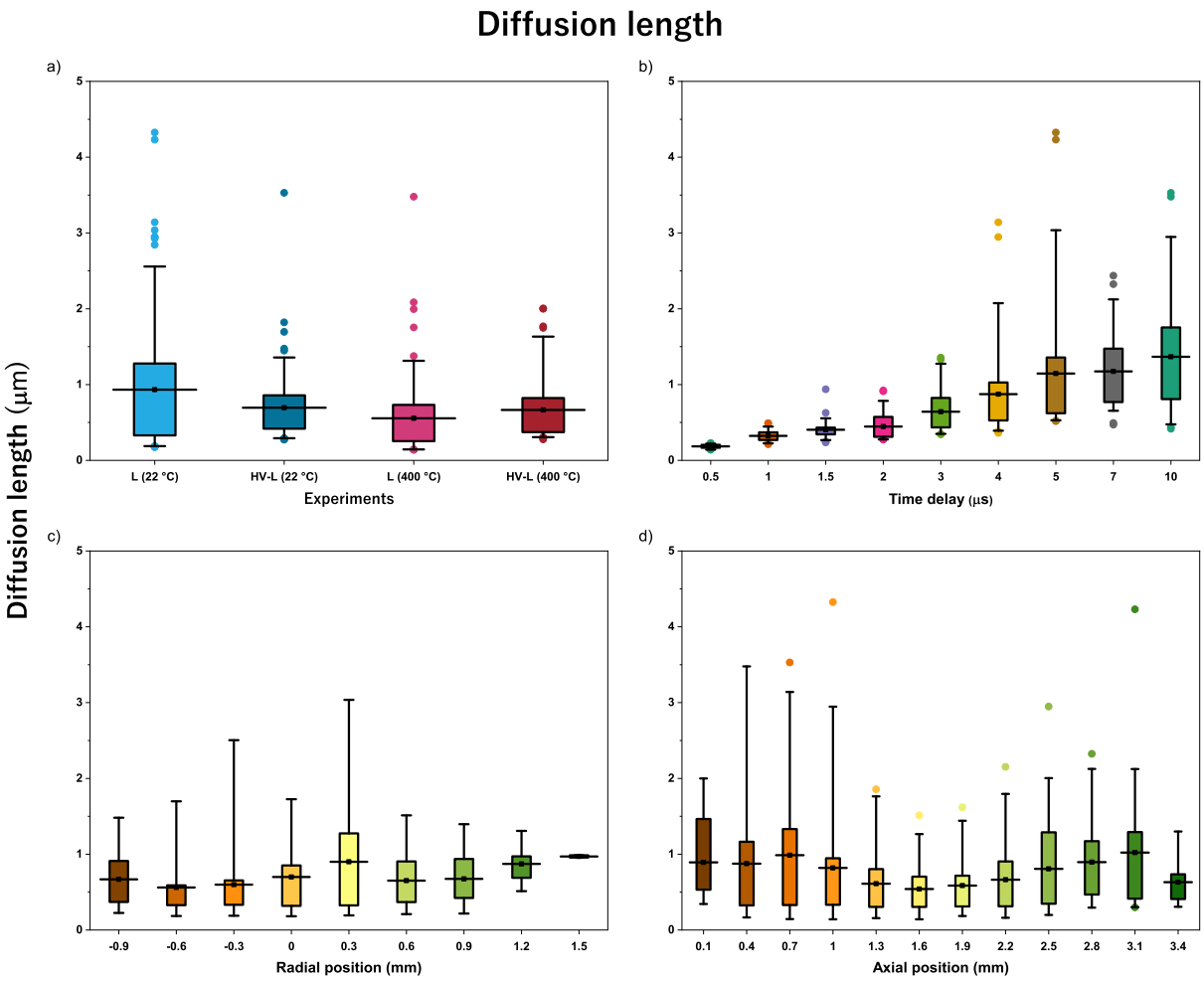

Fig. A.6: Statistical representation of the difussion length. All the data are classified across the three parameters: Experiment, time delay, and spatial position. a) Data classified by experiment: L for LIBS and HV-L for LIBS assisted with HV discharge, and in parentheses indicated the sample temperature. b) Data classified by time delay; c) Data obtained along the radial direction, classified by position; d) Data obtained along the axial direction, classified by position. Each box encapsulates the percentiles from 25 to 75, the central line corresponds to the mean, and the whiskers extend to the 5-95% percentile range of the data.

Bibliography

[1] T. Fujimoto. *Plasma Spectroscopy*. International Series of Monographs on Physics. Clarendon Press - Oxford, 1° edition, 2004 (cited on pages 1, 6, 46).

[2] J. D. Winefordner, I. B. Gornushkin, T. Correll, E. Gibb, B. W. Smith, and N. Omenetto. Comparing several atomic spectrometric methods to the super stars: special emphasis on laser induced breakdown spectrometry, LIBS, a future super star. *Journal of Analytical Atomic Spectrometry*, **19**:1061–1083, 9, 2004. DOI: 10.1039/B400355C (cited on page 1).

[3] A. Miziolek, V. Palleschi, and I. Schechter. *Laser-Induced Breakdown Spectroscopy: Fundamentals and Applications*. Cambridge University Press, 1° edition, 2006 (cited on pages 1, 6–8, 11, 14, 43).

[4] S. C. Jantzi, V. Motto-Ros, F. Trichard, Y. Markushin, N. Melikechi, and A. De Giacomo. Sample treatment and preparation for laser-induced breakdown spectroscopy. *Spectrochimica Acta Part B: Atomic Spectroscopy*, **115**:52–63, 2016. DOI: 10.1016/j.sab.2015.11.002 (cited on pages 1, 12, 15).

[5] W. Xu, X. Liu, Z. Yan, et al. The MarSCoDe Instrument Suite on the Mars Rover of China's Tianwen-1 Mission. *Space Science Reviews*, **217**(64), 2021. DOI: 10.1007/s11214-021-00836-5 (cited on pages 1, 16).

[6] S. Musazzi and U. Perini, editors. *Laser-Induced Breakdown Spectroscopy: Theory and Applications*. Springer-Verlag Berlin Heidelberg, 1° edition, 2014 (cited on pages 1, 8, 11–14, 16, 17, 32).

[7] V. K. Singh, D. K. Tripathi, Y. Deguchi, and Z. Wang, editors. *Laser Induced Breakdown Spectroscopy (LIBS): Concepts, Instrumentation, Data Analysis and Applications*. John Wiley & Sons, Ltd, 1st edition, 2023 (cited on pages 2, 11, 16, 17, 33, 35, 36).

[8] A. Ramírez Buenrostro. *Estudio Espectroscópico de la Interacción de una Descarga de Alta Tensión y un Plasma de Ablación Producido por Láser sobre Muestras Sometidas a Altas Temperaturas (In spanish)*. Bachelor's thesis, National Autonomous University of Mexico, Mexico City, Mexico, Apr. 2022 (cited on pages 2, 7).

[9] M. Amador-Mejía, H. Sobral, and A. Robledo-Martinez. Elemental analysis of heated soil samples using laser-induced breakdown spectroscopy assisted with high-voltage discharges. *Chemosensors*, **11**(3), 2023. DOI: 10.3390/chemosensors11030193 (cited on pages 2, 19–21, 51, 59, 67, 71, 72, 74).

[10] Mexico's Secretary of Environment and Natural Resources. Norma Oficial Mexicana NOM-147-SEMARNAT/SSA1-2004 (In Spanish). 2007. URL: https://www.dof.gob.mx/nota_detalle.php?codigo=4964569&fecha=02/03/2007#gsc.tab=0. Accesed: 19/2/2024 (cited on page 2).

[11] Washington State, Department of Ecology. Model Toxics Control Act Regulation and Statute, MTCA Cleanup Regulation. 2022. URL: https://apps.leg.wa.gov/wac/default.aspx?cite=173-340-900. Accesed: 19/2/2024 (cited on page 2).

[12] D. A. Cremers and L. J. Radziemski. *Handbook of Laser-Induced Breakdown Spectroscopy*. John Wiley & Sons Ltd, 2° edition, 2013 (cited on pages 6, 8, 10–14).

[13] R. Noll. *Laser-Induced Breakdown Spectroscopy: Fundamentals and Applications*. Springer-Verlag Berlin Heidelberg, 1° edition, 2012 (cited on pages 6–15, 32, 37).

[14] L. J. Radziemski and D. A. Cremers, editors. *Laser-Induced Plasmas and Applications*. Marcel Dekker, 1989 (cited on pages 8, 11, 33, 35).

[15] J. P. Singh and S. N. Thakur, editors. *Laser-Induced Breakdown Spectroscopy*. Elsevier Science, 2nd edition, 2020 (cited on pages 8, 11, 12, 14–17, 32, 35).

[16] R. Menzel. *Photonics: Linear and Nonlinear Interactions of Laser Light and Matter*. Advanced Texts in Physics. Springer, 2nd edition, 2007 (cited on pages 9, 10).

[17] H. Sobral, R. Sanginés, and A. Trujillo-Vázquez. Detection of trace elements in ice and water by laser-induced breakdown spectroscopy. *Spectrochimica Acta Part B: Atomic Spectroscopy*, **78**:62–66, 2012. DOI: 10.1016/j.sab.2012.09.005 (cited on page 11).

[18] H. Sobral, M. Amador-Mejía, and C. Márquez-Herrera. Characterization of pottery from teotihuacan using laser-induced breakdown spectroscopy and inductively coupled plasma optical emission spectroscopy. *Appl. Spectrosc.*, **75**(6):728–738, 2021. DOI: 10.1177/0003702821991931 (cited on page 16).

[19] D. L. Death, A. P. Cunningham, and L. Pollard. Multi-element analysis of iron ore pellets by laser-induced breakdown spectroscopy and principal components regression. *Spectrochimica Acta Part B: Atomic Spectroscopy*, **63**(7):763–769, 2008. DOI: 10.1016/j.sab.2008.04.014 (cited on page 16).

[20] P. R. Villas-Boas, M. A. Franco, L. Martin-Neto, H. T. Gollany, and D. M. B. P. Milori. Applications of laser-induced breakdown spectroscopy for soil characterization, part II: review of elemental analysis and soil classification. *European Journal of Soil Science*, **71**(5):805–818, 2020. DOI: 10.1111/ejss.12889 (cited on page 16).

[21] E. Teran-Hinojosa, H. Sobral, C. Sánchez-Pérez, A. Pérez-García, N. Alemán-García, and J. Hernández-Ruiz. Differentiation of fibrotic liver tissue using laser-induced breakdown spectroscopy. *Biomed. Opt. Express*, **8**(8):3816–3827, 2017. DOI: 10.1364/BOE.8.003816 (cited on page 16).

[22] S. Almaviva, L. Caneve, F. Colao, R. Fantoni, and G. Maddaluno. Remote-LIBS characterization of ITER-like plasma facing materials. *Journal of Nuclear Materials*, **421**(1):73–79, 2012. ISSN: 0022-3115. DOI: 10.1016/j.jnucmat.2011.11.050 (cited on page 17).

[23] P. R. Villas-Boas, M. A. Franco, L. Martin-Neto, H. T. Gollany, and D. M. B. P. Milori. Applications of laser-induced breakdown spectroscopy for soil analysis, part I: review of fundamentals and chemical and physical properties. *European Journal of Soil Science*, **71**(5):789–804, 2020. DOI: 10.1111/ejss.12888 (cited on page 17).

[24] V. N. Rai, A. K. Rai, F.-Y. Yueh, and J. P. Singh. Optical emission from laser-induced breakdown plasma of solid and liquid samples in the presence of a magnetic field. *Appl. Opt.*, **42**(12):2085–2093, 2003. DOI: 10.1364/AO.42.002085 (cited on page 17).

[25] H Lan, X. B. Wang, H Chen, D. L. Zuo, and P. X. Lu. Influence of a magnetic field on laser-produced sn plasma. *Plasma Sources Science and Technology*, **24**(5):055012, 2015. DOI: 10.1088/0963-0252/24/5/055012 (cited on page 17).

[26] A. A. Bol'shakov, X. Mao, and R. E. Russo. Spectral emission enhancement by an electric pulse for LIBS and LAMIS. *Journal of Analytical Atomic Spectrometry*, **32**:657–670, 3, 2017. DOI: 10.1039/C6JA00436A (cited on page 18).

[27] O. A. Nassef and H. E. Elsayed-Ali. Spark discharge assisted laser induced breakdown spectroscopy. *Spectrochimica Acta Part B: Atomic Spectroscopy*, **60**(12):1564–1572, 2005. DOI: 10.1016/j.sab.2005.10.010 (cited on page 18).

[28] M. M. Hassanimatin and S. H. Tavassoli. Experimental investigation of effective parameters on signal enhancement in spark assisted laser induced breakdown spectroscopy. *Physics of Plasmas*, **25**(5):053302, 2018. DOI: 10.1063/1.5029942 (cited on page 18).

[29] X. Wang, A. Li, X. Xu, Y. He, S. Qiu, X. Ma, and R. Liu. High enhancement factor in low-power unipolar discharge arc assisted laser induced plasma spectroscopy. *Spectrochimica Acta Part B: Atomic Spectroscopy*, **174**:105996, 2020. DOI: 10.1016/j.sab.2020.105996 (cited on page 19).

[30] Y. Wang, Y. Jiang, X. He, Y. Chen, and R. Li. Triggered parallel discharge in laser-ablation spark-induced breakdown spectroscopy and studies on its analytical performance for aluminum and brass samples. *Spectrochimica Acta Part B: Atomic Spectroscopy*, **150**:9–17, 2018. DOI: 10.1016/j.sab.2018.10.001 (cited on pages 18, 19).

[31] H. Sobral, G. Quintana-Silva, and A. Robledo-Martinez. Time-resolved optical characterization of the interaction between a laser produced plasma and a spark discharge. *Spectrochimica Acta Part B: Atomic Spectroscopy*, **167**:105844, 2020. DOI: 10.1016/j.sab.2020.105844 (cited on pages 18, 19).

[32] A. Robledo-Martinez, H. Sobral, and A. Garcia-Villarreal. Effect of applied voltage and inter-pulse delay in spark-assisted libs. *Spectrochimica Acta Part B: Atomic Spectroscopy*, **144**:7–14, 2018. DOI: 10.1016/j.sab.2018.03.002 (cited on page 18).

[33] K. Li, W. Zhou, Q. Shen, Z. Ren, and B. Peng. Laser ablation assisted spark induced breakdown spectroscopy on soil samples. *Journal of Analytical Atomic Spectrometry*, **25**:1475–1481, 9, 2010. DOI: 10.1039/B922187E (cited on page 19).

[34] X. Li, W. Zhou, K. Li, H. Qian, and Z. Ren. Laser ablation fast pulse discharge plasma spectroscopy analysis of Pb, Mg and Sn in soil. *Optics Communications*, **285**(1):54–58, 2012. DOI: 10.1016/j.optcom.2011.08.074 (cited on page 19).

[35] K. Li, W. Zhou, Q. Shen, J. Shao, and H. Qian. Signal enhancement of lead and arsenic in soil using laser ablation combined with fast electric discharge. *Spectrochimica Acta Part B: Atomic Spectroscopy*, **65**(5):420–424, 2010. DOI: 10.1016/j.sab.2010.04.006 (cited on page 19).

[36] X. F. Li, W. D. Zhou, and Z. F. Cui. Temperature and electron density of soil plasma generated by LA-FPDPS. *Frontiers of Physics*, **7**(6):721–727, 2012. DOI: 10.1007/s11467-012-0254-z (cited on page 19).

[37] S. H. Tavassoli and A. Gragossian. Effect of sample temperature on laser-induced breakdown spectroscopy. *Optics & Laser Technology*, **41**(4):481–485, 2009. DOI: 10.1016/j.optlastec.2008.07.010 (cited on page 20).

[38] S. Eschlböck-Fuchs, M. Haslinger, A. Hinterreiter, P. Kolmhofer, N. Huber, R. Rössler, J. Heitz, and J. Pedarnig. Influence of sample temperature on the expansion dynamics and the optical emission of laser-induced plasma. *Spectrochimica Acta Part B: Atomic Spectroscopy*, **87**:36–42, 2013. DOI: 10.1016/j.sab.2013.05.023 (cited on page 20).

[39] R. Sanginés, H. Sobral, and E. Alvarez-Zauco. The effect of sample temperature on the emission line intensification mechanisms in orthogonal double-pulse laser induced

breakdown spectroscopy. *Spectrochimica Acta Part B: Atomic Spectroscopy*, **68**:40–45, 2012. DOI: 10.1016/j.sab.2012.01.011 (cited on page 20).

[40] U. Liaqat, Z. A. Umar, R. Ahmed, and M. A. Baig. Comparative study of the emission enhancement due to target heating and laser energy on the laser-produced copper-zinc alloy plasma. *Analytical Letters*, **54**(8):1269–1283, 2021. DOI: 10.1080/00032719.2020.1799385 (cited on page 20).

[41] V. N. Lednev, M. Y. Grishin, P. A. Sdvizhenskii, R. D. Asyutin, R. S. Tretyakov, A. Y. Stavertiy, and S. M. Pershin. Sample temperature effect on laser ablation and analytical capabilities of laser induced breakdown spectroscopy. *Journal of Analytical Atomic Spectrometry*, **34**:607–615, 3, 2019. DOI: 10.1039/C8JA00348C (cited on page 20).

[42] A. Robledo-Martinez, A. Garcia-Villarreal, H. Sobral, and O. H. Magos. Emission enhancement in laser-induced breakdown spectroscopy from sample heating with a continuous-wave diode laser. *Spectrochimica Acta Part B: Atomic Spectroscopy*, **199**:106588, 2023. DOI: 10.1016/j.sab.2022.106588 (cited on page 20).

[43] Z. A. Umar, U. Liaqat, R. Ahmed, and M. A. Baig. Detection of lead in soil implying sample heating and laser-induced breakdown spectroscopy. *Appl. Opt.*, **60**(2):452–458, 2021. DOI: 10.1364/AO.404672 (cited on page 21).

[44] F. Chang, J. Yang, H. Lu, and H. Li. A LIBS quantitative analysis method for samples with changing temperature via functional data analysis. *J. Anal. At. Spectrom.*, **36**:1007–1017, 5, 2021. DOI: 10.1039/D0JA00514B (cited on page 21).

[45] P. M. Bellan. *Fundamentals of plasma physics*. Cambridge University Press, 1st edition, 2006 (cited on pages 23–25).

[46] R. J. Goldston and P. H. Rutherford. *Introduction to plasma physics*. Institute of Physics Publishing, 1st edition, 1995 (cited on page 23).

[47] A. Dinklage, T. Klinger, G. Marx, and L. Schweikhard, editors. *Plasma Physics: Confinement, Transport and Collective Effects*. Lecture Notes in Physics. Springer, 1st edition, 2005 (cited on pages 23, 26, 36).

[48] A. F. Alexandrov, L. S. Bogdankevich, and A. A. Rukhadze. *Principles of plasma electrodynamics*. Springer series in Electrophysics. Springer-Verlag Berlin Heidelberg, 1st edition, 1984 (cited on page 23).

[49] W. Lochte-Holtgreven. *Plasma Diagnostics*. AVS Classics Series. American Institute of Physics, 1995 (cited on pages 24, 30, 31, 36, 37).

[50] J. D. Callen. Fundamentals of Plasma Physics [Unpublished manuscript]. University of Wisconsin, Madison (cited on pages 25–27).

[51] V. Fortov, I. Iakubov, and A. Khrapak. *Physics of Strongly Coupled Plasma*. International series of monographs on physics. Oxford University Press, 1st edition, 2006 (cited on pages 27, 33, 36, 99).

[52] F. Reif. *Fundamentals of statistical and thermal physics*. Series in fundamentals of physics. McGraw-Hill, 1965 (cited on page 28).

[53] H. R. Griem. *Plasma Spectroscopy*. McGraw-Hill, Inc., 1964 (cited on pages 28–31, 37, 40, 41).

[54] H. R. Griem. *Principles of Plasma Spectroscopy*. Cambridge Monographs on Plasma Physics. Cambridge University Press, 1° edition, 2005 (cited on pages 29, 33, 37, 39, 40, 45).

[55] J. D. Jackson. *Classical Electrodynamics*. John Wiley, 3rd edition, 1999 (cited on pages 31, 38).

[56] J. F. Ready. *Effects of High-Power Laser Radiation*. Academic Press, 1971 (cited on pages 32, 33, 35).

[57] A. De Giacomo, M. Dell'Aglio, R. Gaudiuso, S. Amoruso, and O. De Pascale. Effects of the background environment on formation, evolution and emission spectra of laser-induced plasmas. *Spectrochimica Acta Part B: Atomic Spectroscopy*, **78**:1–19, 2012. DOI: 10.1016/j.sab.2012.10.003 (cited on pages 33, 35).

[58] H.-J. Kunze. *Introduction to Plasma Spectroscopy*. Springer Series on Atomic, Optical, and Plasma Physics. Springer, 1st edition, 2009 (cited on pages 33, 42–44).

[59] A. De Giacomo, M. Dell'Aglio, O. De Pascale, R. Gaudiuso, V. Palleschi, C. Parigger, and A. Woods. Plasma processes and emission spectra in laser induced plasmas: a point of view. *Spectrochimica Acta Part B: Atomic Spectroscopy*, **100**:180–188, 2014. DOI: 10.1016/j.sab.2014.08.013 (cited on pages 33, 34).

[60] A. A. Ovsyannikov and M. F. Zhukov, editors. *Plasma diagnostics*. Cambridge International Science Publishing, 2000 (cited on page 36).

[61] R. Shankar. *Principles of Quantum Mechanics*. Springer, 2nd edition, 1994 (cited on page 37).

[62] G. Peach. The width of spectral lines. *Contemporary Physics*, **16**(1):17–34, 1975. DOI: 10.1080/05107517508228028 (cited on pages 42, 43).

[63] G. Bekefi. *Principles of Laser Plasmas*. John Wiley & Sons, 1° edition, 1976 (cited on pages 43, 78).

[64] S. Zhang, X. Wang, M. He, Y. Jiang, B. Zhang, W. Hang, and B. Huang. Laser-induced plasma temperature. *Spectrochimica Acta - Part B Atomic Spectroscopy*, **97**:13–33, 2014. DOI: 10.1016/j.sab.2014.04.009 (cited on page 45).

[65] G. Cristoforetti, A. De Giacomo, M. Dell'Aglio, S. Legnaioli, E. Tognoni, V. Palleschi, and N. Omenetto. Local Thermodynamic Equilibrium in Laser-Induced Breakdown Spectroscopy: Beyond the McWhirter criterion. *Spectrochimica Acta Part B: Atomic Spectroscopy*, **65**(1):86–95, 2010. DOI: 10.1016/j.sab.2009.11.005 (cited on pages 45–47, 103, 104).

[66] A. P. Thorne. *Spectrophysics*. Chapman and Hall, 2° edition, 1988 (cited on page 45).

[67] H. R. Griem. Validity of local thermal equilibrium in plasma spectroscopy. *Phys. Rev.*, **131**:1170–1176, 3, 1963. DOI: 10.1103/PhysRev.131.1170 (cited on pages 45–47).

[68] J. A. Aguilera and C. Aragón. Characterization of a laser-induced plasma by spatially resolved spectroscopy of neutral atom and ion emissions.: comparison of local and spatially integrated measurements. *Spectrochimica Acta Part B: Atomic Spectroscopy*, **59**(12):1861–1876, 2004. DOI: 10.1016/j.sab.2004.08.003 (cited on pages 50, 94).

[69] J. A. Aguilera and C. Aragón. Multi-element saha–boltzmann and boltzmann plots in laser-induced plasmas. *Spectrochimica Acta Part B: Atomic Spectroscopy*, **62**(4):378 –385, 2007. ISSN: 0584-8547. DOI: 10.1016/j.sab.2007.03.024 (cited on page 50).

[70] R. Lal and M. K. Shukla. *Principles of Soil Physics*. Books in Soils, Plants, and the Environment. CRC Press, 1st edition, 2004 (cited on page 52).

[71] P. J. Vittum. *Chapter 238 - Soil Habitats*. In *Encyclopedia of Insects*. V. H. Resh and R. T. Cardé, editors. 2° edition. Academic Press, 2° edition, 2009, pages 935–939. DOI: 10.1016/B978-0-12-374144-8.00247-2 (cited on page 53).

[72] Amplitude laser. Surelite I, II, III. 2018. URL: https://amplitude-laser.com/products/nanosecond-lasers/standard-nanosecond-lasers/surelite-i-ii-iii/. Accesed: 27/10/2023 (cited on pages 53, 54).

[73] Berkeley Nucleonics Corporation. Model 575 | 0.001 hz to 10 mhz digital delay / pulse generator. 2021. URL: https://www.berkeleynucleonics.com/Model-575. Accesed: 27/10/2023 (cited on page 54).

[74] Tektronix. Dpo4000b. URL: https://www.tek.com/datasheet/mso4000b-dpo4000b-series-mixed-signal-oscilloscope-datasheet. Accesed: 27/10/2023 (cited on page 55).

[75] Spellman HV. Bertan 205b. URL: https://testequipment.center/Product_Documents/Bertan-205B-30R-Specifications-7E5A5.pdf. Accesed: 27/10/2023 (cited on page 55).

[76] Spellman HV. Slm series. URL: https://www.spellmanhv.com/es/high-voltage-power-supplies/SLM. Accesed: 27/10/2023 (cited on page 55).

[77] Princeton Instruments. Acton series sp-2500i. URL: http://ridl.cfd.rit.edu/products/manuals/Princeton%20Acton/SP-2500i.pdf. Accesed: 27/10/2023 (cited on page 57).

[78] Princeton Instruments. Pi-max. URL: http://pi-j.jp/pdf/manual/PI-MAX_SystemManual.pdf. Accesed: 27/10/2023 (cited on page 57).

[79] A. Kramida, Y. Ralchenko, J. Reader, and NIST ASD Team. NIST Atomic Spectra Database (ver. 5.10). 2022. URL: https://physics.nist.gov/asd. Accesed: 2/11/2023 (cited on pages 61, 87, 100, 103).

[80] Newport Corporation. Kpx094 plano-convex lens. URL: https://www.newport.com/p/KPX094. Accesed: 4/11/2023 (cited on page 66).

[81] M. N. Polyanskiy. Refractiveindex.info database of optical constants. 2023. URL: https://refractiveindex.info/. Accesed: 2/11/2023 (cited on page 66).

[82] D. J. Schroeder. *Astronomical Optics*. Academic Press, 2nd edition, 2000 (cited on page 72).

[83] M. S. Dimitrijević and S. Sahal-Bréchot. Stark broadening of Mg I spectral lines. *Physica Scripta*, **52**(1):41–51, 1995. DOI: 10.1088/0031-8949/52/1/008 (cited on page 79).

[84] M. Corsi, G. Cristoforetti, M. Hidalgo, D. Iriarte, S. Legnaioli, V. Palleschi, A. Salvetti, and E. Tognoni. Effect of laser-induced crater depth in laser-induced breakdown spectroscopy emission features. *Applied Spectroscopy*, **59**(7):853–860, 2005. DOI: 10.1366/0003702054411607 (cited on page 85).

[85] A. De Giacomo, M. Dell'Aglio, R. Gaudiuso, G. Cristoforetti, S. Legnaioli, V. Palleschi, and E. Tognoni. Spatial distribution of hydrogen and other emitters in aluminum laser-induced plasma in air and consequences on spatially integrated laser-induced breakdown spectroscopy measurements. *Spectrochimica Acta Part B: Atomic Spectroscopy*, **63**(9):980–987, 2008. DOI: 10.1016/j.sab.2008.06.010 (cited on page 85).